
Influence of carrier density on the ultrafast optical response of graphene and few-layer graphene

Thomas Limmer

Dissertation
an der Fakultät für Physik
der Ludwig-Maximilians-Universität
München

vorgelegt von
Thomas Limmer
aus Inning a. H.

München
Mai 2012

Erstgutachter: Prof. Dr. Jochen Feldmann
Zweitgutachter: Prof. Dr. Jan von Delft
Tag der Verteidigung: 09.08.2012

Cover: Graphene

Publications

Publications based on the result of this thesis:

- *Influence of carrier density on the electronic cooling channels of bilayer graphene*
T. Limmer, A.J. Houtepen, A. Niggebaum, R. Tautz and E. Da Como
Appl. Phys. Lett., **99**, 103104 (2011)
- *Carrier recombination lifetime in few-layer graphene*
T. Limmer, A. Grüneis, E. Da Como and J. Feldmann
submitted to Phys. Rev. Lett.
- *Femtosecond photoinduced absorption in graphite: Evidence for optically induced compression of the graphite lattice*
T. Limmer, E. Da Como and J. Feldmann
Manuscript in preparation

Further publications:

- *Structural correlations in the generation of polaron pairs in low-bandgap polymers for photovoltaics*
R. Tautz, E. Da Como, T. Limmer, J. Feldmann, H.J. Egelhaaf, E. von Hauff, V. Lemaire, D. Beljonne, S. Yilmaz, I. Dumsch, S. Allard and U. Scherf
submitted to Nature Comm.
- *Reduced Charge Transfer Exciton Recombination in Organic Semiconductor Heterojunctions by Molecular Doping*
F. Deschler, E. Da Como, T. Limmer, R. Tautz, T. Godde, M. Bayer, E. von Hauff, S. Yilmaz, S. Allard, U. Scherf and J. Feldmann
Phys. Rev. Lett., **107**, 127402 (2011)
- *Anisotropic optical emission of single CdSe/CdS tetrapod heterostructures: Evidence for a wavefunction symmetry breaking*
C. Mauser, T. Limmer, E. Da Como, K. Becker, A.L. Rogach, J. Feldmann and D.V. Talapin
Phys. Rev. B, **77**, 153303 (2008)

Kurzfassung

Die vorliegende Arbeit untersucht die dynamische Antwort von Graphen und Multilagen-Graphen auf ultrakurze, optische Anregung in unterschiedlichen Bereichen der photoinduzierten Ladungsträgerdichte. Ein detailliertes Verständnis der Ladungsträgerdynamiken bei höheren Temperaturen ist wichtig für diverse Anwendungen, z.B. in Photodetektoren und Transistoren.

Im ersten Teil wird die Energieverlustrate von photoinduzierten Ladungsträgern in 2-lagigen Graphen bestimmt und relevante Mechanismen der Ladungsträgerabkühlung und deren Abhängigkeit von der anfänglichen Ladungsträgertemperatur werden diskutiert. Mit Hilfe der ultrakurzen, transienten Absorptionsspektroskopie im Energiebereich von 0.25 eV-1.3 eV werden die Ladungsträgerkühlkurven in Abhängigkeit der anfänglichen Ladungsträgertemperatur und -dichte gemessen. Zwei unterschiedliche Bereiche konnten hierbei identifiziert werden, einer wird von der Emission optischer, der andere von akustischen Phononen dominiert. Bei höheren, induzierten Ladungsträgerdichten findet der Übergang zwischen den beiden Bereichen bei höheren Temperaturen statt, da die Effizienz des Kühlprozesses durch optischen Phononen abnimmt. Kühlen durch akustische Phononen, welches keine Sättigung aufweist, übernimmt einen größeren Anteil bei größeren Ladungsträgerdichten.

Die Reduktion der photoinduzierten Ladungsträgerdichte eröffnet eine neue Methode, die Ladungsträger-Rekombinationszeit in Multilagen-Graphen zu bestimmen. Der nah- bis mittel-Infrarot Spektralbereich entspricht energetisch dem Bereich der Inter-subbänder von Multilagen-Graphen, deren Komplexität mit zunehmender Lagenanzahl steigt. Die aus der Absorptionsspektroskopie gewonnenen Transienten zeigen einzelne Bereiche erhöhter photoinduzierter Absorption, überlagert vom photoinduzierten Ausbleichen optisch gekoppelter Interbandlevels. Unterstützt durch tight-binding Modelle der elektronischen Struktur werden den Absorptionsbanden Interbandübergänge zugeordnet. Diese Übergänge weisen interessanterweise langsamere Dynamiken auf als das Ausbleichen der Interbandübergänge. Der Grund hierfür liegt in der speziellen Leitungs- und Valenzbandstruktur, die eine Absorption von Photonen unabhängig vom Wellenvektor der Ladungsträger zulässt. Die Lebenszeit der Interbandübergänge hängt daher einzig von der intrinsischen Lebenszeit der photoinduzierten Ladungsträger ab und stellt eine neuartige und elegante Methode dar, die Ladungsträger-Rekombinationszeit in Multilagen-Graphen zu bestimmen.

Bei sehr hoher Strahlungsintensität zeigen die Transienten von Graphit eine sehr starke, photoinduzierte Erhöhung der Absorption innerhalb der ersten hundert Femtosekunden nach Anregung, abhängig von Abfrage Energie, Abfrage-Leistung und zeitlicher Dauer des Abfrage-Pulses. Der ultrakurze Anstieg der Absorption wird mit einer initialen Kompression entlang der c-Achse des Graphitgitters erklärt, induziert durch photoangeregte Phononen, welche eine strukturelle und elektronische Modifikation in der Ebene und senkrecht dazu zur Folge haben. Die nachfolgende, erhöhte Transmission wird begleitet von Oszillationen des gemessenen Signals, welche mit 43 cm^{-1} exakt der Frequenz der Zwischenlagen-Schermode von Multilagen-Graphen entsprechen. Dies demonstriert eindrucksvoll, wie Femtosekundenpulse transiente, elektronische Zustände induzieren können, die stark mit kohärenten Gittervibrationen koppeln.

Die Ergebnisse dieser Arbeit ermöglichen ein tieferes Verständnis der einzigartigen, elektronischen Struktur von Graphen und Multilagen-Graphen, was eine Grundvoraussetzung für die Entwicklung von Graphen-basierten, elektronischen Bauteilen ist.

Abstract

In this thesis, the response of graphene and few-layer graphene to femtosecond optical photoexcitation at different magnitudes of photoinduced carrier densities has been investigated. A detailed understanding of carrier dynamics in graphene at elevated temperatures is important for applications in high-speed photonic and optoelectronic devices.

In the first part, we determine the energy loss rate of photoexcited carriers in 2-layer graphene and discuss the relevant mechanism of carrier cooling and their dependence on the initial carrier temperature. Measurements were performed by means of femtosecond transient absorption spectroscopy on a broad photon energy range. From the transients, the carrier cooling curves for different initial temperatures and densities of the photoexcited carriers are extracted. Two regimes of carrier cooling are identified, dominated by optical and acoustic phonon emission, respectively. Interestingly, for increasing carrier density the crossover between the two regimes occurs at larger carrier temperatures since cooling via optical phonons experiences a bottleneck. Cooling via acoustic phonons, which are less sensitive to saturation, show an increasing contribution at high carrier density explaining the shift in the crossover. The results address important questions regarding ultrafast optoelectronic devices where transport is dominated by hot carriers and their scattering by phonons.

In another series of experiments performed by decreasing the photoexcited carrier density, we are able to determine the carrier recombination lifetime in graphene flakes differing in the number of layers. At low carrier densities, the differential absorption spectra show an evolving structure, with the number of graphene layers, composed of photoinduced absorption bands superimposed on the bleaching of the interband optically coupled states. Supported by tight binding model calculations of the electronic structure, we assign the photoinduced absorption features to intersubband transitions. Interestingly, these transitions show a slower dynamics than the interband bleaching because of their independence from the absolute energy value of the carriers with respect to the Dirac point. The lifetime of these intersubband transitions depends exclusively on the intrinsic lifetime of the photoinduced carriers. The experiments provide a new and elegant method to measure the carrier recombination lifetime in a class of zero gap semiconductors such as few-layer graphene. The findings are of particular interest for applications, since the response time of photodiodes is determined by the carrier lifetime.

By analyzing the response of graphite at a high level of photoexcitation we identified a strong temporal limited photoinduced absorption appearing in the first hundreds of femtoseconds after photoexcitation. The ultrashort increase in absorption is attributed to an initial compression along the *c*-axis of the graphite lattice induced by photoexcited coherent phonons leading to a structural modification of the carbon atoms and electronic sp^2/sp^3 like hybridization. In the following *c*-axis expansion the transients are accompanied by coherent oscillations with the frequency of the interlayer (E_{2g}) shearing mode. Remarkably, these results demonstrate how femtosecond pulses can induce transient electronic states strongly coupled with coherent vibrational oscillations in a 2D semimetal.

These results contribute to a deeper understanding of the unique electronic structure of graphene and few-layer graphene, which is essential for the development of graphene-based devices.

Contents

Kurzfassung	ix
Abstract	x
1. Introduction	3
2. Theoretical background	7
2.1. Electronic structure	7
2.1.1. Carbon electronic hybridization	7
2.1.2. Unit cell and Brillouin zone of graphene	7
2.1.3. Tight-Binding model	9
2.2. Light absorption in graphene	14
2.2.1. Optical conductance of a graphene monolayer	14
2.2.2. Optical absorption of a n-layer system	16
2.3. Vibrational properties	21
2.3.1. Phonon dispersion relation	21
2.3.2. Electron-phonon interaction	25
2.4. Raman scattering	27
2.4.1. Basic principles	27
2.4.2. First- and second-order Raman process	31
3. Methods	35
3.1. Sample preparation	35
3.1.1. Mechanical exfoliation	35
3.1.2. Transfer process	38
3.1.3. CVD graphene	39

3.1.4. Samples for optical spectroscopy	40
3.1.5. Characterization of single flakes	41
3.2. Time-resolved spectroscopy	43
3.2.1. Differential transmission pump-probe spectroscopy: method	44
3.2.2. Laser system for pump-probe spectroscopy	45
3.3. Raman setup	48
4. Influence of carrier density on the electronic cooling channels of 2-layer graphene	51
4.1. Physical background of carrier cooling in graphene	52
4.2. Ultrafast carrier dynamics in graphene	53
4.3. Spectrally resolved carrier dynamics	56
4.4. Analysis of the carrier dynamics	58
4.5. Influence of carrier density on energy loss	62
4.6. Summary	64
5. Carrier recombination lifetime in few-layer graphene	65
5.1. Few-layer graphene and the problem of carrier recombination . . .	66
5.2. Samples and experimental settings	68
5.3. Differential absorption transients of few-layer graphene flakes . . .	70
5.4. Carrier recombination lifetime	74
5.5. Summary	78
6. Ultrafast optically induced compression of graphite lattice	79
6.1. Graphite subjected to high fluence laser pulses	80
6.2. Fluence dependent photoinduced absorption in graphite	81
6.3. Influence of probe photon energy, carrier density and pulse dura- tion on the transient absorption	83
6.4. Lattice oscillations in graphite	89
6.5. Summary	93
7. Conclusions and outlook	95

A. From graphene to graphite: Evolution of the 2D Raman peak	99
A.1. Physical background Raman scattering in graphene	99
A.2. Raman spectrum of graphite and graphene	100
A.3. 2D Raman peak vs. number of layers	101
A.4. Calculation of the phonon density of states	105
Bibliography	113
Acknowledgments	123

1. Introduction

For more than sixty years, the material graphite has been studied theoretically [1–3]. Models like the Slonczewski-Weiss-McClure and tight-binding model have been widely used to describe the electronic structure and the properties of numerous carbon based materials. Graphene, which is defined as a single two dimensional layer of carbon atoms arranged in a honeycomb like lattice, can be considered as the main building block of diverse carbon based materials, like fullerenes [4], carbon nanotubes [5] or the three dimensional graphite. Since the 1980s, graphene was mainly investigated by theoretical groups because more than 70 years ago Landau and Peierls [6, 7] as well as Mermin and Wagner in the late 60s [8, 9] argued that a strictly two dimensional material is thermodynamically not stable in three dimensional space. The argument was that a divergent contribution to thermal fluctuations in low-dimensional crystal lattices should lead to a displacement of atoms where they become comparable to interatomic distances at any finite temperature [10]. It took several years before Andre Geim and co-workers at the University of Manchester reported on the existence of the free-standing, two dimensional atomic crystal graphene [11]. The existence of this single, one atom thick structure was explained in a way that the extracted 2D crystals become intrinsically stable when entering the third dimension by the formation of ripples [12]. This 3D warping can lead to a gain in elastic energy suppressing thermal vibrations, which, above a certain temperature, can minimize the total free energy and deform the material [13]. As already mentioned graphene is defined as a single atom thick layer of carbon atoms in a hexagonal lattice. Therefore, only this material can be considered as a real 2D material. Already two or more layers of graphene stacked on top of one another have a different electronic band structure, and above 10 layers show the characteristics are those of 3D bulk graphite [14].

Besides the huge interest from the theoretical point of view, graphene also shows remarkable electronic and optical properties. As a direct consequence of the linear energy dispersion, the charge carriers in graphene behave as massless Dirac fermions [15]. Consequently, the charge carriers are described by the relativistic Dirac equation, rather than the non-relativistic Schrödinger equation, with an effective Fermi velocity of about 10^6 m/s.

Besides the electronic properties, graphene shows also interesting optical properties. One being the universal optical conductance [16] $G_0 = e^2/(4\hbar)$, which gives the transmittance of a 1-layer graphene of $T \approx 1 - \pi\alpha \approx 97.7\%$. Here α is the fine-structure constant. Hence, each layer absorbs $\approx 2.3\%$, independent of photon energy, over the visible spectrum [17].

In this work, we explore the response of graphene and few-layer graphene structures to excitation by ultrafast optical pulses producing a non-equilibrium carrier population in the valence and conduction bands. The dynamics of carrier cooling by emission of phonons is of particular interest in carbon based low dimensional structures, such as carbon nanotubes and graphene because of their extraordinary mobilities and current densities in devices [18] in the presence of strong electron-phonon interactions [19]. We look at the dynamics of carriers as a function of the energy and the photoexcited carrier density and discuss the main mechanism which returns the excited system back to the room temperature equilibrium. It is crucial to understand how hot carriers lose energy in different regimes of photo-carrier densities, as this process is one of the limiting factors in the performance of high-speed devices, like photodetectors [20] and ultrafast switches [21]. We note that, although the mechanism by which carriers gain energy is different for applied electric fields and photoexcitation, the process by which they lose energy with the lattice (i.e. by the emission of phonons) is the same [22]. Therefore, information gained by optical studies is useful in understanding high-field hot-carrier-dominated transport. Besides the huge interest in 1-layer graphene during the last years also few-layer graphene has been a matter of particular interest. One of the remarkable properties is a band gap that can be opened in 2-layer and 3-layer graphene by applying external electric fields [23–25]. Since the electronic properties of graphene are changing with every additional stacked layer, we have

also investigated changes in the optical properties as a function of the number of stacked layers.

This thesis is organized in 6 chapters. In chapter 2 we introduce the main theoretical background of the electronic and vibrational structure of graphene and few-layer graphene. Furthermore, the light absorption process and all theoretical methods used in the work to model experimental data are discussed.

The micromechanical exfoliation method to obtain graphene from graphite flakes is discussed in detail in chapter 3 together with a technique to subsequently transfer the flakes to any desired substrate. The experimental methods necessary to perform femtosecond pump-probe spectroscopy in the near- to middle-infrared spectral region and the laser system are also described. As Raman scattering spectroscopy allows a fast and non-destructive method to determine several characteristic parameters in graphite, the operation principles are discussed.

In chapter 4 we consider the carrier cooling in 2-layer graphene since this material is gaining an increasing interest in photonics and optoelectronics [26]. We look at the dynamics of carriers as a function of the photoexcited carrier density and discuss the main mechanisms which bring the excited system back to the room temperature equilibrium. Hot carriers are expected to emit optical phonons as long as their energy with respect to the bottom of the band is above the optical phonon energy $\hbar\Omega_{op}$. In proximity to this energy, acoustic phonons are the dominant cooling channel for equilibrating the electronic system with the lattice. By performing pump-probe spectroscopy in a photon energy range below $2\hbar\Omega_{op}$, we could identify two regimes of carrier cooling, dominated by optical and acoustic phonon emission. Interestingly, for increasing carrier density the crossover between the two regimes occurs at larger carrier temperatures, since cooling via optical phonons experiences a bottleneck.

The dynamics of carriers at very low densities of photoexcited carriers, $\approx 4 \times 10^{10} \text{ cm}^{-2}$, is discussed in chapter 5. In these experimental conditions which corresponds to very low pump fluences, we could identify distinctive absorption bands in the differential absorption transients of few-layer graphene samples with two or more stacked layers according to the electronic band structure. Supported by tight binding model calculations of the electronic structure, we have assigned the photoinduced absorption feature to intersubband transitions as the number of

layers is increased. These transitions exhibit dynamics on a longer timescale with respect to the interband bleaching. As discussed in chapter 5 their dynamics is independent from the energy value of the carriers with respect to the Dirac point. Thus, the lifetime of these intersubband transitions depends on the lifetime of the photoinduced carriers and not on relaxation phenomena. Thus, it provides an elegant method to measure the carrier recombination lifetime in a class of semimetals such as few-layer graphene.

In chapter 6 a study of the response of multi-layer graphene to intense femtosecond pulse irradiation is presented. We have studied changes in the optical absorption at photon energies close to the Dirac point, 0.3 eV to 0.6 eV, induced by ultrashort optical pulses. Thus far, no optical studies in this energy range for fluences in the preablation regime of graphite have been reported. We will show an ultrafast photoinduced increase in absorption followed by an increase in transmission and a subsequent decay of the transmission change signal. The findings will be explained by an initial compression of the graphite lattice followed by an expansion and oscillation of the lattice. The frequency of this oscillation is extracted from the experimental data and corresponds to the vibrational shearing mode of graphite. The observed optical response of the material is a direct consequence of the high intensity femtosecond optical pulses.

The thesis ends with a conclusion, summarizing the reported findings and an outlook.

2. Theoretical background

2.1. Electronic structure

2.1.1. Carbon electronic hybridization

The electronic configuration of a free isolated carbon atom is $1s^2 2s^2 2p^2$. If carbon atoms combine to build a molecular solid state body, the electrons from the 2s and 2p orbital form a hybrid orbital in the direction of the axis of the chemical bond. Depending on the kind of crystalline structure of the solid body, a different number of hybrid orbitals is needed to bind to two up to four next neighbors. Carbon forms sp^n hybrid orbitals with $n = 1$ (acetylene), $n = 2$ (graphite or single wall nanotubes) and $n = 3$ (diamond). This work focuses on the analysis of sp^2 systems which comprise a planar, hexagonal lattice structure. In this system, two 2s electrons and one 2p electron ($2p_x$ and $2p_y$ in the graphene plane) form three sp^2 hybrid orbitals, which form three σ (binding) and three σ^* (anti-binding) orbitals and are responsible for the strong covalent bond between carbon atoms. The remaining $2p_z$ electrons constitute binding and anti-binding π and π^* orbitals, perpendicular to the graphene plane, which account for the accessibility of the electronic spectra with visible light (0 eV-3 eV) in optical experiments. In this work, only the physical properties mainly ascribed to the π electron system are considered and analyzed.

2.1.2. Unit cell and Brillouin zone of graphene

Graphene consists of a single atomic layer of graphite, in which the carbon atoms adopt a honeycomb configuration. The unit cell can be described as a rhombus with two atoms as shown in Fig.2.1.

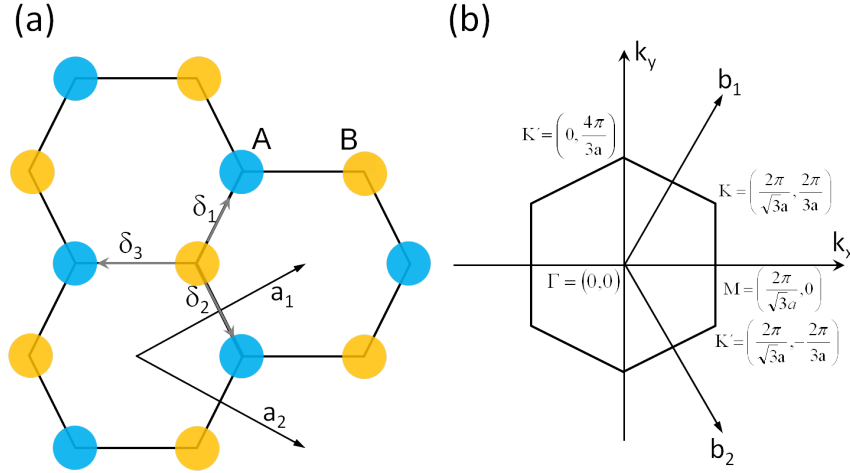


Figure 2.1.: (a) The unit cell and (b) the first Brillouin zone (BZ) of graphene. The two vectors \mathbf{a}_1 and \mathbf{a}_2 define the unit cell. Every atom (A and B) in the unit cell is surrounded by three next neighbors shown by the vectors δ_1 , δ_2 and δ_3 . The Brillouin zone is defined by the reciprocal lattice vectors \mathbf{b}_1 and \mathbf{b}_2 with $|\mathbf{b}_1| = |\mathbf{b}_2| = \frac{4\pi}{\sqrt{3}a}$. In the center of the BZ lies the Γ point, in the corners of the BZ the \mathbf{K} and \mathbf{K}' points. The \mathbf{M} point can be found between two neighboring \mathbf{K} and \mathbf{K}' points.

The two atoms A and B of the unit cell constitute two non-equivalent atoms because these two atoms cannot be connected with one or a combination of the unit vectors \mathbf{a}_1 and \mathbf{a}_2 . The unit vectors have a length of $a = \sqrt{3}a_0 = |\mathbf{a}_1| = |\mathbf{a}_2| = 2.46 \text{ \AA}$ with $a_0 = 1.42 \text{ \AA}$ the length of the C-C bond and are defined by

$$\mathbf{a}_1 = a \left(\frac{1}{2}, \frac{\sqrt{3}}{2} \right), \mathbf{a}_2 = a \left(\frac{1}{2}, -\frac{\sqrt{3}}{2} \right)$$

Figure 2.1(b) depicts the first Brillouin zone (BZ) of graphene with some of the high-symmetry points. The BZ of graphene can also be described as a hexagon with the symmetry points $\Gamma = (0,0)$, hexagon corner $\mathbf{K} = 1/a(2\pi/\sqrt{3}, 2\pi/3)$ and the center of one side $\mathbf{M} = 1/a(2\pi/\sqrt{3}, 0)$. One important property shall be noted here. There are two non-equivalent K points with the coordinates \mathbf{K} and \mathbf{K}' which belong to the Fermi-surface of graphene. The latter will be explained in the next paragraph. The reciprocal lattice vectors of the first Brillouin zone of graphene are defined by the following requirement: $\mathbf{a}_i \cdot \mathbf{b}_j = 2\pi\delta_{ij}$ with δ_{ij} being

the Kronecker delta. They are defined by

$$\mathbf{b}_1 = \frac{1}{a} \left(\frac{2\pi}{\sqrt{3}}, 2\pi \right), \mathbf{b}_2 = \frac{1}{a} \left(\frac{2\pi}{\sqrt{3}}, -2\pi \right).$$

In graphite the distance between two neighboring sheets of graphene is given by $c_0 = 3.35 \text{ \AA}$ [27]. Reference [28] showed that in a system consisting of only two sheets of graphene, bilayer graphene, the intraplanar distance corresponds to the intraplanar lattice distance of graphite. According to this, the values of graphite are used in this work whenever the electronic properties or structure of multilayer graphene is calculated or analyzed.

2.1.3. Tight-Binding model

Analyzing the electronic properties of graphene, we calculated the electronic dispersion relation by means of a tight-binding model. Starting with a graphene monolayer the hamiltonian of a N-layer system is successively build up and the electronic band structure computed. The simple tight binding method uses a linear combination of atomic orbitals (LCAO) in order to calculate the energy E of the electronic system as a function of the wave vector \mathbf{k} . The tight binding approximation of a crystal describes the eigenfunctions of the electrons starting from the respective atomic orbitals. In a graphene unit cell five atomic orbitals for every atom can be identified: 1s, 2s and three 2p, which sums up for a total of ten orbitals per unit cell. For the calculation of σ and π , only four valence electrons are considered (2s and 2p), though, while the electrons of 1s are neglected. Actually, the 1s orbital of a carbon atom has an energy of 258 eV below vacuum level so that the 1s energy bands can be equalized with the atomic levels [29]. Therefore, only the π atomic orbitals are considered for the calculation.

The tight-binding model used in this work restricts to the interatomic interactions to the ones depicted in figure 2.2 between two single carbon atoms of a layer system in AB-configuration: γ_0 the interactions between two neighboring A-B-atoms in one plane, γ_1 between A-A, γ_3 between B-B and γ_4 between A-B

atoms in the neighboring planes above and below and γ_2 between A-A and γ_5 between B-B atoms in the plane one further away.

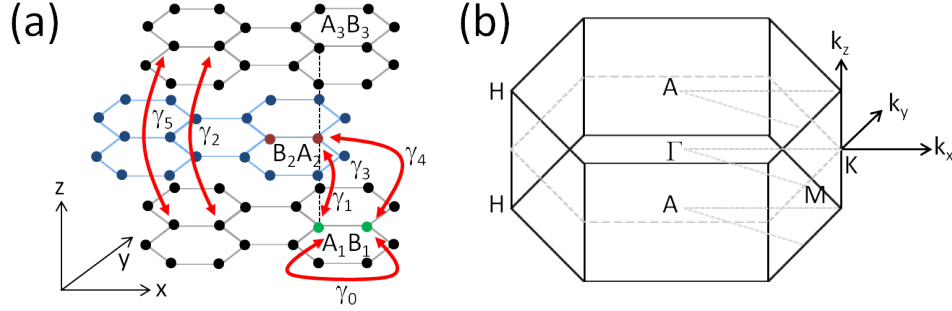


Figure 2.2.: The crystal structure (a) of three sheets of graphene in AB-stacking with their respective tight-binding parameters γ_i and the interactions between the carbon atoms taken into consideration for the calculations. (b) shows the three-dimensional Brillouin zone of graphite with the high-symmetry points and the coordinate system used in this work.

Reference [29] demonstrated that the energetic gap in *AB-stacked* graphite between σ and π bands with respect to the Fermi-energy is very large (at the K point about 10 eV). As a consequence, the π bands dominate the most important electronic characteristics of the system in the low-energy regime and we can limit ourselves to the calculation of the π bands in the following.

Starting with the two atoms A and B of the unit cell of a graphene sheet, two tight-binding Bloch-functions are build up for every graphene sheet:

$$\psi^{A_i}(\mathbf{k}, \mathbf{r}) = \frac{1}{\sqrt{N}} \sum_{A_i} \Phi_A(\mathbf{r} - \mathbf{r}_{A_i}) \exp(i\mathbf{k} \cdot \mathbf{r}_{A_i}) \quad (2.1)$$

$$\psi^{B_i}(\mathbf{k}, \mathbf{r}) = \frac{1}{\sqrt{N}} \sum_{B_i} \Phi_B(\mathbf{r} - \mathbf{r}_{B_i}) \exp(i\mathbf{k} \cdot \mathbf{r}_{B_i}) \quad (2.2)$$

with \mathbf{r}_{A_i} and \mathbf{r}_{B_i} the positions of the A and B nuclei within the sheet i , Φ_A and Φ_B the atomic wave function of an A or B carbon atom, respectively, multiplied with a phase factor and N the number of unit cells. The complete electronic wave

function for a system of N_l graphene layers is given by

$$\Psi_l(\mathbf{k}, \mathbf{r}) = \sum_{i=1}^{N_l} c_{A_i}(\mathbf{k}) \psi^{A_i}(\mathbf{k}, \mathbf{r}) + \sum_{i=1}^{N_l} c_{B_i}(\mathbf{k}) \psi^{B_i}(\mathbf{k}, \mathbf{r}) \quad (2.3)$$

with N_l the number of layers. The $2N_l$ coefficients $c_{A_i}(\mathbf{k})$ and $c_{B_i}(\mathbf{k})$ are coefficients of the Bloch-wave function and are determined by diagonalization of the Hamiltonian. As we are only interested in the energy dispersion around the \mathbf{K} points and due to the relatively large distance between the carbon atoms, we can neglect the overlap-matrices $S(\mathbf{k})$ [14]. The tight-binding parameters, as shown in figure 2.2, are exactly defined in [14] and can be found in table 1.1.

TB parameter	SWMcC parameter	Value for $N_l = 1$	Value for $N_l = 2$	Value for $N_l > 2$
E_0	γ_2	0	-0.0206	-0.0206
Δ'	$\Delta - \gamma_2 + \gamma_5$	0	0.0366	0.0366
γ'_0	γ_0	3.12	3.12	3.12
γ'_1	γ_1	0	0.377	0.377
γ'_2	$\gamma_2/2$	0		-0.0103
γ'_3	γ_3	0	0.29	0.29
γ'_4	$-\gamma_4$	0	-0.120	-0.120
γ'_5	$\gamma_5/2$	0		0.0125

Table 2.1.: Relation between the parameters of the tight-binding (TB) model and the Slonczewski-Weiss-McClure model (SWMcC-model) [3] [2] together with the parameters for a number of layers of $N_l = 1$, $N_l = 2$ and $N_l > 2$. All values are in eV [14].

Table 1.1 gives the relation between the parameters of the tight-binding (TB) model and the Slonczewski-Weiss-McClure model (SWMcC-model) [3] [2] together with the parameters for a number of layers of $N_l = 1$, $N_l = 2$ and $N_l > 2$. All values in eV [14]. For the case of a single layer of graphene, only the γ_0 interaction is considered. Starting from $N_l > 2$ all atomic interactions are considered.

The individual matrix elements needed in order to calculate the tight binding Hamiltonian are the following:

$$\langle \psi^{A_i} | H | \psi^{A_i} \rangle \approx E_0 + \Delta' \quad (2.4)$$

$$\langle \psi^{A_i} | H | \psi^{B_i} \rangle \approx \gamma'_0 f(k_x, k_y) \quad (\text{i,uneven}) \quad (2.5)$$

$$\text{and } \gamma'_0 f^*(k_x, k_y) \quad (\text{i,even}) \quad (2.6)$$

$$\langle \psi^{A_i} | H | \psi^{A_{i+1}} \rangle \approx \gamma'_0 \quad (2.7)$$

$$\langle \psi^{A_i} | H | \psi^{B_{i+1}} \rangle \approx \gamma'_4 f^*(k_x, k_y) \quad (\text{i,uneven}) \quad (2.8)$$

$$\text{and } \gamma'_4 f(k_x, k_y) \quad (\text{i,even}) \quad (2.9)$$

$$\langle \psi^{A_i} | H | \psi^{A_{i+2}} \rangle \approx \gamma'_5 \quad (2.10)$$

$$\langle \psi^{B_i} | H | \psi^{B_{i+1}} \rangle \approx E_0 \quad (2.11)$$

$$\langle \psi^{B_i} | H | \psi^{A_{i+1}} \rangle = \langle \psi^{A_i} | H | \psi^{B_{i+1}} \rangle \quad (2.12)$$

$$\langle \psi^{B_i} | H | \psi^{B_{i+1}} \rangle \approx \gamma'_3 f(k_x, k_y) \quad (\text{i,uneven}) \quad (2.13)$$

$$\text{and } \gamma'_3 f^*(k_x, k_y) \quad (\text{i,even}) \quad (2.14)$$

$$\langle \psi^{B_i} | H | \psi^{B_{i+2}} \rangle \approx \gamma'_2 \quad (2.15)$$

The function $f(k_x, k_y)$ is given by:

$$f(k_x, k_y) = \exp\left(ik_x a / \sqrt{3}\right) + 2 \exp\left(-ik_x a / 2\sqrt{3}\right) \cos(k_y a / 2) \quad (2.16)$$

Starting from the individual, included matrix elements, we can build up the Hamiltonian for any number of graphene sheets N_l . First, the matrix elements for the two first and the two last sheets are defined. For the latter, we have to discriminate between an even or uneven number of layers. Subsequently, the elements of the in-between layers are successively added while differentiating

between even and uneven sheets.

Figure 2.3 shows the calculated band structure for $N_l = 1$ layers of graphene in the first Brillouin zone.

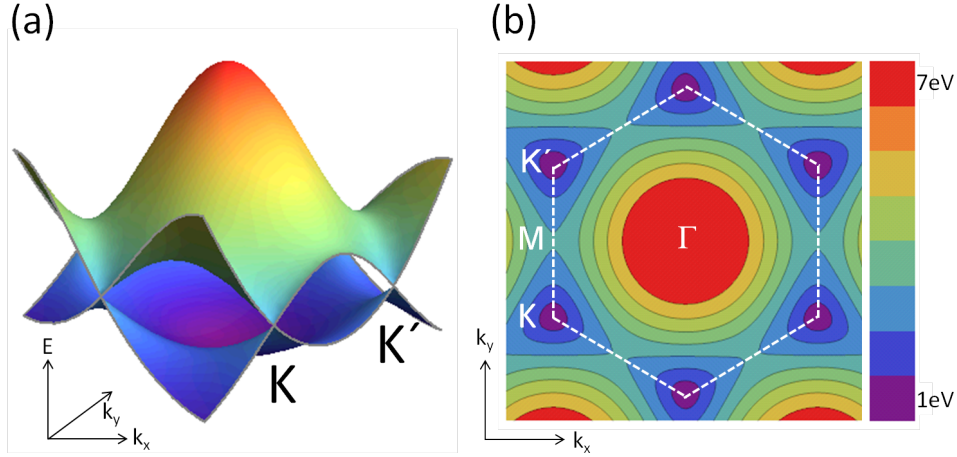


Figure 2.3.: Electronic dispersion relation for $N_l = 1$ layers of graphene for the first Brillouin zone. (a) π and π^* bands together with the two symmetry points \mathbf{K} and \mathbf{K}' . In the area around these symmetry points the dispersion relation is approximately linear in \mathbf{k} . (b) dispersion relation of the π^* band with selected equi-energy surfaces in and beyond the first Brillouin zone. The honeycomb structure of the BZ is clearly visible. All values are in eV, the energetic distance between two equi-energy lines is 1 eV.

Fig. 2.3(a) shows the π and π^* bands together with the two symmetry points \mathbf{K} and \mathbf{K}' in the first BZ for monolayer graphene. In the area around these two symmetry points the dispersion relation for a monolayer graphene is approximately linear in \mathbf{k} . Optical transitions between binding and anti-binding bands [14] are allowed. Fig. 2.3(b) illustrates that the area relevant for optical spectroscopy in the visible and infrared is the one around the \mathbf{K} points. For small electron energies up to 1eV, the equi-energy surfaces are circles close to the \mathbf{K} points. For larger energies the equi-energy surfaces are deformed towards triangular, an effect known as *trigonal warping* [1]. In chapter 4 this model will be used to calculate the band dispersion for few- and multilayer graphene structures.

2.2. Light absorption in graphene

In 2008, Nair et al. [17] could show that the absorption of one graphene layer is determined by the fundamental constant $\pi\alpha = 2.293\%$ with $\alpha = e^2/\hbar c \approx 1/137$ being the fine structure constant. This parameter describes the coupling between light and relativistic electrons and is traditionally associated with aspects from quantum electrodynamics [17]. The origin of this frequency-independent value is associated with special properties of two dimensional massless Dirac fermions and the gapless electronic spectrum of graphene. Ref. [30, 31] describe it with a chiral resonance, which is a process where a particle-antiparticle pair is created upon the absorption of a photon, and the result for graphene follows directly upon consideration of its four-fold spinodal degeneracy. This universal absorbance is equivalent to an optical sheet conductivity for graphene exhibiting a frequency-independent value of $\sigma = \pi G_0/4$, with $G_0 = 2e^2/h$ being the quantum of conductance [32]. Nevertheless this simple picture breaks down at lower photon energies due to several effects like spectral and sample-to-sample variations [32]. In the following chapter the optical conductivity is derived for a monolayer graphene starting from the Kubo-formula followed by a detailed description of the absorption spectrum calculated for a system consisting of N-layers.

2.2.1. Optical conductance of a graphene monolayer

This section explains how the optical conductance of a graphene monolayer can be calculated. Starting from the Kubo-formula in the *Dirac cone approximation* [33], which means that the energy dispersion in vicinity to the high symmetry \mathbf{K} points is assumed to be strictly linear, the optical conductance of graphene can be presented as follows according to [34],

$$\sigma(\omega, T, \mu) = \frac{e^2\omega}{i\pi\hbar} \left[\int dE \frac{|E|}{\omega^2} \frac{df_0(E)}{dE} - \int dE \frac{f_0(-E) - f_0(E)}{(\omega + i\delta)^2 - 4E^2} \right] \quad (2.17)$$

with frequency ω , energy E , $\delta \rightarrow 0$ an infinitesimal integration quantity ,

$$f_0(E) = \{ \exp[(E - \mu)/k_B T] + 1 \}^{-1} \quad (2.18)$$

the Fermi-Dirac distribution function, k_B the Boltzmann-constant, μ the chemical potential and T the temperature of the charge carriers. The validity of equation 2.17 is limited to the high-frequency regime or $\omega \gg (kv_F, \tau^{-1})$ with the Fermi-velocity $v_F = 1.1 \cdot 10^6$ m/s and the collision rate of carriers τ^{-1} . Several authors [35–37] show that the main mechanism of carrier relaxation is provided by charged impurities, where the collision rate is then given by $\tau^{-1} \approx 2\pi^2 e^4 n_{imp} / \hbar \epsilon_g^2 E$ with ϵ_g the dielectric constant of graphene, E the characteristic electron energy and n_{imp} the density of charged impurities per unit surface [33]. The first term of equation 2.17 is allocated to intraband electron-photon interactions [38]. Including a phenomenological scattering rate Γ , it can be proven that the intraband part of the surface conductance of graphene has a drude form:

$$\sigma^{intra}(\omega, T) = 4 \ln 2 \frac{e^2}{h} \frac{(\hbar\Gamma)k_B T}{(\hbar\omega)^2 + (\hbar\Gamma)^2} \quad (2.19)$$

The second term of equation 2.17 is assigned to interband electron-photon interactions. The real part describes the absorption of photons following interband transitions between valence and conduction band. With the assumption $\mu \ll k_B T$ it can be displayed as follows:

$$\sigma^{inter}(\omega, T, \mu) = \frac{\pi e^2}{4h} \left[\tanh\left(\frac{\hbar\omega + 2\mu}{4k_B T}\right) + \tanh\left(\frac{\hbar\omega - 2\mu}{4k_B T}\right) \right] \quad (2.20)$$

As graphene does not have an energy bandgap, the individual contributions of both inter- and intraband transitions can have different contributions. For large frequencies, which means $\omega > k_B T$, $\omega > \mu$ interband transitions dominate, for small frequencies intraband transitions play the more important role. For very small frequencies, the intraband contribution to the total conductance outbalances the other terms since in this regime phonons, defects and other scatter processes significantly contribute to scattering. The special form of the optical conductance in the low frequency regime is explained in [39] in greater detail, but is not of relevance for the spectral range analyzed in this work.

2.2.2. Optical absorption of a n-layer system

In the last section, the optical conductance and, hence, the absorbance of a mono-layer graphene was derived. Kuzmenko and co-workers [16] measured the optical conductivity of graphite in the infrared spectral region. It was found that the conductivity is of the order of the universal value $\sigma = \pi G_0/4$ per layer, but due to the interlayer coupling it exhibited a significant variation with the photon energy in the infrared region. In order to investigate the optical properties of n-layer systems, the band structure of each system has to be incorporated in the calculation of the absorption of a n-layer system. Computing the absorption of a system of n-layers of graphene, we used a quantum mechanical description of the response of a medium to an external electric field. For this purpose we first derive an expression for the atomic optical susceptibility.

Optical susceptibility The stationary Schrödinger equation of a single electron in an atom is [40]

$$H_0 \Psi_n(\mathbf{r}) = \epsilon_n \Psi_n(\mathbf{r}), \quad (2.21)$$

where ϵ_n and $\Psi_n(\mathbf{r})$ are the energy eigenvalues and the eigenfunctions respectively. An optical field $E(t)$ couples to the dipole moment of the atom and causes time-dependent changes of the wavefunction

$$i\hbar \frac{\partial \Psi(\mathbf{r}, t)}{\partial t} = (H_0 + H_I(t)) \Psi_n(\mathbf{r}, t) \quad (2.22)$$

with a perturbation $H_I(t) = -exE(t) = -dE(t)$, where d is the operator for the electric dipole moment for an assumed polarization of the homogeneous electromagnetic field in x direction. Expanding the time-dependent wavefunctions in the stationary wavefunctions

$$\Psi(\mathbf{r}, t) = \sum_m a_m(t) e^{-i\epsilon_m t} \psi_m(\mathbf{r}) \quad (2.23)$$

and inserting the resulting expression into the Schrödinger equation we find for the coefficients a_n the equation

$$i\hbar \frac{da_n}{dt} = -E(t) \sum_m e^{-i\epsilon_{nm}t} \langle n | d | m \rangle a_m \quad (2.24)$$

with the electric dipole matrix element $d_{nm} = \langle n | d | m \rangle = \int d^3r \Psi_n^*(\mathbf{r}) d \Psi_m^*(\mathbf{r})$ and the energy difference $\epsilon_{nm} = \epsilon_n - \epsilon_m$. Equation 2.24 is now solved iteratively with taking the field as perturbation. We limit ourselves to linear order perturbation theory and consider only terms linear in the field, so we employ *linear response theory*.

The field-induced polarization is now given as the expectation value of the dipole operator

$$P(t) = -n_0 \int d^3r \Psi_n^*(\mathbf{r}, t) d \Psi_m^*(\mathbf{r}, t) \quad (2.25)$$

with n_0 the density of the independent or non-interacting atoms in the system. Inserting the total wavefunction from time-dependent perturbation theory (not displayed) into equation 2.25 and considering only terms linear in the field we obtain the polarization

$$P(t) = -\frac{n_0}{\hbar} \sum_n |d_{nm}|^2 \int \frac{d\omega}{2\pi} E(\omega) e^{-i\omega t} \left(\frac{1}{\omega - \epsilon_{nm} + i\gamma} - \frac{1}{\omega + \epsilon_{nm} + i\gamma} \right) \quad (2.26)$$

$$= \int \frac{d\omega}{2\pi} P(\omega) e^{-i\omega t} \quad (2.27)$$

This equation yields $P(\omega) = \chi(\omega)E(\omega)$ with the optical susceptibility

$$\chi(\omega) = -\frac{n_0}{\hbar} \sum_m |d_{nm}|^2 \left(\frac{1}{\omega - \epsilon_{nm} + i\gamma} - \frac{1}{\omega + \epsilon_{nm} + i\gamma} \right) \quad (2.28)$$

The parameter γ is introduced in the calculation to assure that $E(t) \rightarrow 0$ when $t \rightarrow \infty$. This adiabatic switch-on factor plays the same role as the damping parameter in the classical oscillator model. For notational simplicity the $\lim_{\gamma \rightarrow 0}$ in front of the expression is dropped, but it is understood that this limit is always implicit.

Oscillator strength A comparison of the previous result for the optical susceptibility with the result from the classical oscillator model described for example in [40] reveals a similar structure with the difference that the atom is represented not only by one but many oscillators with different transitions energies ϵ_{nm} . By rewriting expression 2.27 for the optical susceptibility

$$\chi(\omega) = -\frac{n_0 e^2}{2m_0} \sum_n \frac{f_{nl}}{\epsilon_{nl}} \left(\frac{1}{\omega - \epsilon_{lm} + i\gamma} - \frac{1}{\omega + \epsilon_{lm} + i\gamma} \right) \quad (2.29)$$

each partial oscillator has the strength of

$$f_{nl} = \frac{2m_0}{\hbar} |x_{nl}|^2 \epsilon_{nl} \quad (2.30)$$

By summing over all the final states it can be shown [40] that adding the strengths of all oscillators fulfills the *oscillator strength* sum rule

$$\sum_n f_{nl} = 1 \quad (2.31)$$

which means that the total transition strength in an atom can be viewed as that of one oscillator which is distributed over many partial oscillators, each having the strength f_{nl} .

Absorption The displacement field $D(\omega)$ can be expressed in terms of the polarization $P(\omega)$ and the electric field $E(\omega)$

$$D(\omega) = E(\omega) + 4\pi P(\omega) = \epsilon(\omega)E(\omega) \quad (2.32)$$

where the optical dielectric function $\epsilon(\omega)$ is related with the optical susceptibility as

$$\epsilon(\omega) = 1 + 4\pi\chi(\omega) \quad (2.33)$$

For a plane wave propagating with wavenumber $k(\omega)$ and extinction coefficient $\kappa(\omega)$ in a dielectric medium we can obtain by solving Maxwells equations the relations [40]

$$n(\omega) = \left[\frac{1}{2} \left(\epsilon'(\omega) + \sqrt{\epsilon'^2(\omega) + \epsilon''^2(\omega)} \right) \right]^{1/2} \quad (2.34)$$

for the complex index of refraction and

$$\alpha(\omega) = \frac{\omega}{n(\omega)c} \epsilon''(\omega) \quad (2.35)$$

the absorption coefficient.

If furthermore $\epsilon''(\omega) \ll \epsilon'(\omega)$ and the index of refraction is only weakly frequency dependent, we can approximate

$$\alpha(\omega) \cong \frac{\omega}{n_b c} \epsilon''(\omega) = \frac{4\pi\omega}{n_b c} \chi''(\omega) \quad (2.36)$$

where n_b is the background refractive index.

Absorption spectrum The optical absorption function of a system consisting of n -layers of graphene is calculated according to the last section by combining Eq.2.27 and Eq.2.35. In comparison to the full set of optical Bloch equations, the quasi-equilibrium approximation used here is a considerable simplification in the analysis of the optical response [40]. Here, a quasi-thermal distribution of the electrons in the conduction band and of the holes in the valence band is used to replace the diagonal elements of the density matrix. In our calculations we use the following expression for the optical absorption [41]:

$$\begin{aligned} \alpha(\omega) \propto \frac{1}{m_e} \sum_{i,f} \int_{1stBZ} \frac{dk_x}{2\pi} \frac{dk_y}{2\pi} \cdot \left| \langle \Psi^f(\mathbf{k}) | \hat{\mathbf{E}} \cdot \vec{P} | \Psi^i(\mathbf{k}) \rangle \right|^2 \\ \times \text{Im} \left[\frac{f(E^f(\mathbf{k}, T, \mu)) - f(E^i(\mathbf{k}, T, \mu))}{E^f(\mathbf{k}) - E^i(\mathbf{k}) - \omega - i\Gamma} \right] \end{aligned} \quad (2.37)$$

with the Fermi-Dirac distribution function

$$f(E^{i,f}(\mathbf{k}), T, \mu) = (1 + \exp((E^{i,f}(\mathbf{k}) - \mu)/k_B T))^{-1} \quad (2.38)$$

and the energy of the corresponding band $E^{i,f}(\mathbf{k})$ with the band index for initial and final state $i, f = \pm 1, \pm 2, \dots, \pm N_l$ where $+(-)$ corresponds to unoccupied π^* states (occupied π states), the electronic temperature T and chemical potential μ and a broadening parameter $\Gamma = 0.001\gamma_0$ due to various deexcitation mechanism

[41]. Electrons in the presence of an electromagnetic field with $\hat{\mathbf{E}}_x \parallel \hat{x}$ ($\hat{\mathbf{E}}_y \parallel \hat{y}$) are excited from the valence to the conduction band or within a subband. \vec{P} is the electron momentum operator. At $T = 0$ only interband excitations occur. The selection rules for an optical transition are assumed to be $\Delta\mathbf{k} = 0$ because the momentum change due to a transition induced by a photon is in the order of $k_{photon} = \frac{2\pi}{\lambda_{photon}} \approx \frac{k_{BZ}}{3000}$. The dipole matrix elements of Eq. 2.35 are evaluated within the gradient approximation [29, 41–44]

$$\left| \langle \Psi^f(\mathbf{k}) | \hat{\mathbf{E}} \cdot \vec{P} | \Psi^i(\mathbf{k}) \rangle \right| \approx \left| \langle \Psi^f(\mathbf{k}) | \nabla_k H | \Psi^i(\mathbf{k}) \rangle \right| \quad (2.39)$$

where the dipole elements are approximated by taking the gradient of the corresponding hamiltonian matrix elements with the wavefunctions taken from the tight-binding model described in section 2.1.3. Only when a Hamiltonian matrix element H_{lm} contains the function $f(k_x, k_y)$ from equation 2.16, $\frac{\partial H}{\partial k}$ is nonzero. Due to the considered interactions between different neighboring carbon atoms in the tight-binding model, there are three different possible channels with substantial contributions to the dipole elements [41]. The electron jumping from the site A (B) to the next nearest neighboring atom B (A) in the same graphite sheet makes the major contribution to the first channel. The electron hopping from the site A (B) to site B (A) located on the next nearest neighbor graphite sheet is the second channel. The electron hopping from site B on one sheet to the site B located on the next nearest neighbor graphite sheet gives the third contribution.

The oscillator strength of an optical transition is calculated by the absolute square of the corresponding dipole matrix element. Fig.2.4(a) displays the dispersion relation close to the \mathbf{K} -point in the first Brillouin Zone of 1-layer graphene with one possible optical transition ϵ_{12} between valence and conduction band indicated by the red vertical arrow. Fig.2.4(b) shows the calculated oscillator strength as a function of k_x and k_y in an extended Brillouin Zone for the assigned optical transition between conduction and valence band as a colour contour plot with values of different contours given in the plot. The hexagonal structure of the Brillouin Zone is clearly visible. The oscillator strength has a maximum on the connection line between adjacent carbon atoms.

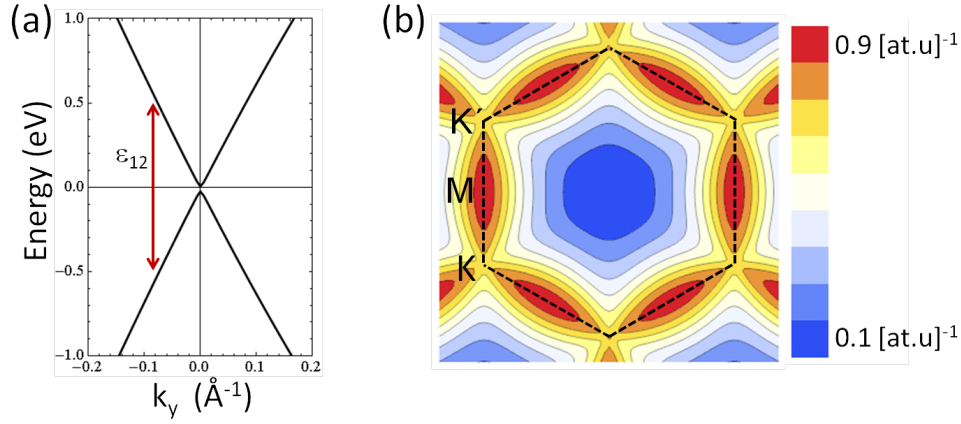


Figure 2.4.: (a) Dispersion relation close to the \mathbf{K} -point in the first Brillouin Zone of 1-layer graphene with one possible optical transition ϵ_{12} between valence and conduction band indicated by the vertical arrow. (b) Calculated oscillator strength as a function of k_x and k_y in the first Brillouin Zone for the assigned optical transition between conduction and valence band as a colour contour plot with values of different contours given in the plot. The hexagonal structure of the Brillouin Zone is clearly visible. The oscillator strength has a maximum on the connection line between adjacent carbon atoms.

Therefore, optical transitions between symmetric bands show a high oscillator strength on the connection line between two \mathbf{K} -points and are negligible close to the Γ -point.

2.3. Vibrational properties

The next section briefly presents the widely used force-constant method to describe the phonon dispersion relations in graphene. By evaluation of the dynamical matrix of the lattice, the electron-phonon interaction can be quantified within the tight-binding framework. The description follows the detailed argumentation by Alexander Grüneis [29] and Georgii Samsonidze [45].

2.3.1. Phonon dispersion relation

Phonon dispersion relations are a fundamental physical property of solid materials. They can be used to determine mechanical, thermal and other condensed

matter phenomena. Experimentally, the phonon dispersion relation of three dimensional graphite and two dimensional graphene has been measured by inelastic neutron scattering [46] and electron energy loss spectroscopy [47, 48]. These methods are accurate for probing zone center phonons, but are not able to determine the region between the K - and M -point in the Brillouin zone. Inelastic X-ray scattering has provided the means to determine this region experimentally in graphite [49]. In the following a tight binding force constant model with a set of 8 force constants of four nearest neighbour atoms will be presented. The force constants have been fitted to reproduce the experimental data from the above mentioned measurements [29]. In the force constant model, the i -th atom is con-

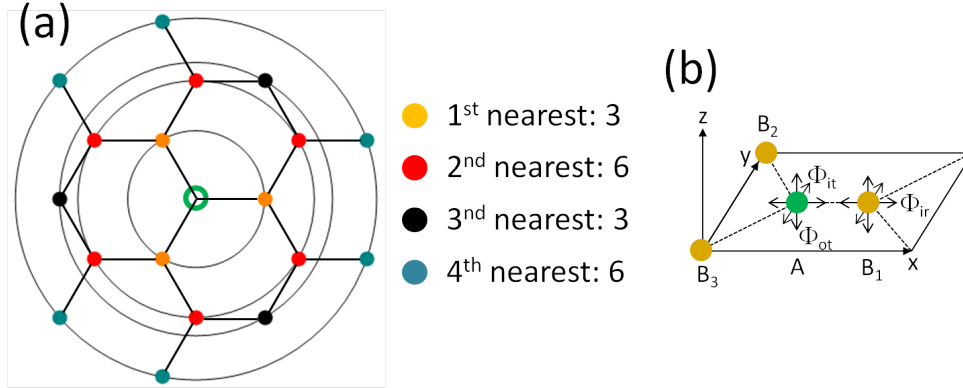


Figure 2.5.: (a) Neighbor atoms of graphene up to fourth nearest neighbor for an A atom (green circle). Black thin circles connect the same class of neighbor atoms. (b) Force sheet constants between A and B_1 atom on a graphene sheet. ϕ_{ir} , ϕ_{it} and ϕ_{ot} are the forces for the nearest neighbor atoms in the in-plane radial, in-plane tangential and out-of-plane tangential directions, respectively. The force tensors for the atoms B_2 and B_3 are obtained by appropriately rotating the K^{ij} tensor for A and B_1 atom.

nected to its j -th neighbour atom through a force constant tensor K^{ij} , whose components are given by the force constants. In general, the equations of motion for the displacement of the i -th atom measured from the equilibrium position, $\mathbf{u}_i = (x_i, y_i, z_i)$ for N atoms in the unit cells is given by:

$$M_i \ddot{\mathbf{u}}_i = \sum_j K^{ij} (\mathbf{u}_j - \mathbf{u}_i), \quad (i=1, \dots, N) \quad (2.40)$$

with M_i the mass and the sum over j is normally taken over only a few neighbor distances relative to the i -th site. Since the force between two atoms is decreasing with increasing interatomic distance, the cut-off radius determines the distance at which interactions between atoms can be neglected. Here, the cut-off radius is set to the fourth nearest neighbour distance, a valid assumption, since the result of the calculation is able to reproduce experimental neutron scattering data [46]. Every A and B atom has 18 neighbouring atoms up to the fourth shell (see Fig.2.5(a)), so we need 12 force constant tensors for the A (B) atom, considering the force constant parameters and four shells. For each shell we have to consider three force constants for the degrees of freedom: (i) in-plane radial, along bond direction, (ii) in-plane transversal, perpendicular to the bond direction and (iii) out-of-plane, depicted in Fig.2.5(b). We use a coordinate system in which one atom is on the x-axis with the coordinate given by the radius of the shell. The force constant tensor is then rotated to every position of an atom in all shells by a rotation matrix U_m around the z-axis perpendicular to the graphene plane. As an example for the first shell, the rotation matrix of an atom A with the three atoms B_n ($n=1,2,3$) is given by [27]:

$$U_m = \begin{pmatrix} \cos(\theta_m) & \sin(\theta_m) & 0 \\ -\sin(\theta_m) & \cos(\theta_m) & 0 \\ 0 & 0 & 1 \end{pmatrix} \quad (2.41)$$

For the first shell the force constant tensors can be evaluated by:

$$K^{A,B_m} = U_m^{-1} K^{A,B_1} U_m, (m=2,3) \quad (2.42)$$

For $m=1$, U_m is given by the unity matrix and has only diagonal matrix elements

$$K^{A,B_1} = \begin{pmatrix} \phi_{ir}^{(1)} & 0 & 0 \\ 0 & \phi_{it}^{(2)} & 0 \\ 0 & 0 & \phi_{ot}^{(3)} \end{pmatrix} \quad (2.43)$$

with the force constants between an atom in the center and on the positive x-axis in the n -th shell given by in-plane radial $\phi_{ir}^{(n)}$, in-plane transversal $\phi_{it}^{(n)}$ and

out-of-plane transversal $\phi_{ot}^{(n)}$ vibrations. The vibrational properties are obtained by solving the following equation:

$$D(\mathbf{q})\mathbf{S}^\nu(\mathbf{q}) = 0 \quad (2.44)$$

with the phonon wavevector \mathbf{q} , the phonon eigenfunction of the ν -th branch $\mathbf{S}^\nu(\mathbf{q})$ and the dynamical matrix $D(\mathbf{q})$. The latter is defined by

$$D(\mathbf{q}) = \begin{pmatrix} D^{AA} & D^{AB} \\ D^{BA} & D^{BB} \end{pmatrix} \quad (2.45)$$

with the matrix elements given by:

$$D^{ij}(\mathbf{q}) = \left(\sum_{j''} K^{ij''} - M_i \omega^2 \mathbf{q} I \right) \delta_{ij} - \sum_{j'} K^{ij'} e^{i\mathbf{q} \cdot \Delta \mathbf{R}_{ij'}} \quad , (i, j = A, B) \quad (2.46)$$

Here, the sum over j'' is taken for all neighbor sites from the i -th atom with $K^{ij''} \neq 0$, and the sum over j' is taken for the equivalent sites to the j -th atom, I is a 3x3 unit matrix. Similar to the tight binding calculations of the electronic dispersions in section 2.1.3, the dynamical matrix is given by the product of the force constant tensor K^{ij} and a phase factor $e^{i\mathbf{q} \cdot \Delta \mathbf{R}_{ij'}}$ with the distance vector $\Delta \mathbf{R}_{ij'}$ between atoms i and j . For the force constants of graphite, we use the results according to Ref. [29] obtained by fitting experimental data from elastic neutron scattering from Ref. [50]: $\phi_{ir}^{(1)} = 36.50$, $\phi_{it}^{(1)} = 24.50$, $\phi_{ir}^{(2)} = 8.80$, $\phi_{it}^{(2)} = -3.23$, $\phi_{ir}^{(3)} = 3.00$, $\phi_{it}^{(3)} = -5.25$, $\phi_{ir}^{(4)} = -1.91$, $\phi_{it}^{(4)} = 2.29$, $\phi_{ot}^{(1)} = 9.82$, $\phi_{ot}^{(2)} = -0.40$, $\phi_{ot}^{(3)} = 0.15$, $\phi_{ot}^{(4)} = -0.58$. Units are 10^4 dyn/cm. By solving Eq.2.43 the 6x6 dynamical matrix is obtained and the eigenvalues give the 6 branches of the graphite phonon dispersion. Fig.2.6(a) shows the calculated phonon dispersion relation along the Γ - M - K - Γ direction in the first Brillouin zone. There are six phonon branches that are in order of increasing energy, out-of-plane transverse acoustic (oTA), in-plane transverse acoustic (iTA), in-plane longitudinal acoustic (LA), out-of-plane transverse optical (oTO), in-plane transverse optical (iTO) and in-plane longitudinal optical (LO). Additionally, the corresponding density of states vs.

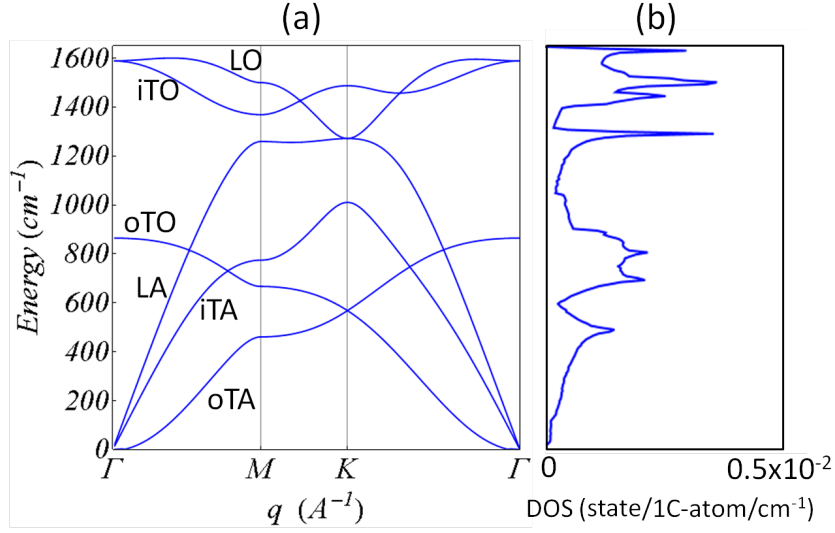


Figure 2.6.: (a) Phonon dispersion relation of graphite calculated with the force constant model described in the text. There are six phonon branches that are in increasing energy out-of-plane transverse acoustic (oTA), in-plane transverse acoustic (iTA), in-plane longitudinal acoustic (LA), out-of-plane transverse optical (oTO), in-plane transverse optical (iTO) and in-plane longitudinal optical (LO). (b) The corresponding density of states vs phonon energy for phonon modes in units of states/1C-atom/cm⁻¹ × 10⁻².

phonon energy for phonon modes is shown in Fig.2.6(b), showing a high density of states for the optical modes.

2.3.2. Electron-phonon interaction

The following paragraph briefly summarizes, how to calculate electron phonon coupling constants with a tight binding approximation for graphite as a function of electron wavevector \mathbf{k} and phonon branch ν . Details of the method can be found in Ref. [29].

The crystal potential at a position \mathbf{r} in the crystal is a time-dependent function due to atomic vibrations. The latter are given by the phonon mode ν with frequency $\omega_{\nu}^{\mathbf{q}}$ and phonon wavevector \mathbf{q} . In the model, a so called "rigid-ion" or "adiabatic"-approximation is used, which regards the potential of the atom as perfectly following the movement of the atom. The total potential is given by the sum over atomic screened ion potentials $v(\mathbf{r} - \mathbf{R}_{\sigma}^{\nu})$, with $\mathbf{R}_{\sigma}^{\nu}$ being the coordinate

of the atom $\sigma = A, B$ in the ν -th unit cell of graphene which is displaced from the equilibrium position due to a phonon. The displacement is described by the phonon eigenfunction $\mathbf{S}_\sigma^\nu(\mathbf{q})$. In first-order, time-dependent perturbation theory, the matrix element between an initial $\mathbf{k}-i$ and final electron state $\mathbf{k}-f$ with energies E_i and E_f is given by:

$$M_{vib\rho}^{f,i,\nu}(\mathbf{k}_f, \mathbf{k}_i) = - \sum_{v=1}^{N_\nu} \sum_{\sigma=A,B} \langle \Psi^f(\mathbf{r}, \mathbf{k}_f) | A_\rho^\nu(\mathbf{q}) \nabla v(\mathbf{r} - \mathbf{R}_\sigma^v) \cdot \mathbf{S}_\sigma^\nu(\mathbf{R}_\sigma^v, \mathbf{q}) | \Psi^i(\mathbf{r}, \mathbf{k}_i) \rangle \quad (2.47)$$

Here, $\Psi^{f,i}(\mathbf{r}, \mathbf{k}_{f,i})$ denotes the electron wavefunction at final and initial band index with final and initial electron wavevector $\mathbf{k}_{f,i}$ as given by Eq.2.3. The phonon eigenfunction is given by multiplying a phase factor to the solution of the 6x6 dynamical matrix described in the last section:

$$\mathbf{S}_\sigma^\nu(\mathbf{R}_\sigma^v, \mathbf{q}) = \mathbf{S}_\sigma^\nu(\mathbf{q}) e^{i\mathbf{q} \cdot \mathbf{R}_\sigma^v} \quad (2.48)$$

The amplitude of the vibration $A_\rho^\nu(\mathbf{q})$ depends on the temperature T through the number of phonons in the mode with index ν given by the Bose-Einstein distribution $N_{vib\rho}^\nu(\mathbf{q}) = (\exp(\hbar\omega_{vib}^\nu(\mathbf{q})/k_B T) - 1)^{-1}$ and the number of atoms N_a that contribute to the phonon. The index ρ refers to the process of phonon emission $\rho = E$ or phonon absorption $\rho = A$. Obviously $N_{vibE}^\nu(\mathbf{q}) = N_{vibA}^\nu(\mathbf{q}) + 1$. The amplitude is given by:

$$A_\rho^\nu(\mathbf{q}) = \sqrt{\frac{2\hbar N_{vib\rho}^\nu(\mathbf{q})}{m_C \omega_{vib}^\nu(\mathbf{q}) N_a}} \quad (2.49)$$

with $m_C = 1.9927 \times 10^{-26}$ kg the mass of a carbon atom.

Using the substitution $\mathbf{R}_s^u = \mathbf{R}_\sigma^v + \mathbf{r}_\sigma^{ls}$, where l is for the l -th atom of type $s=A,B$, and the momentum conservation for an electron phonon scattering event $\mathbf{k}_i = \mathbf{k}_f \pm \mathbf{q}$, Eq.2.46 becomes:

$$M_{vib\rho}^{f,i,\nu}(\mathbf{k}_f, \mathbf{k}_i) = - \sum_{l,l',s,s',\sigma} A_\rho^\nu(\mathbf{q}) c_{s'}^{f*}(\mathbf{k}_f) c_{s'}^i(\mathbf{k}_i) e^{-i\mathbf{r}_\sigma^{l's'} \cdot \mathbf{k}_f} e^{-i\mathbf{r}_\sigma^{ls} \cdot \mathbf{k}_i} \mathbf{S}_\sigma^\nu(\mathbf{q}) \cdot \mathbf{m}_D(\mathbf{r}_\sigma^{l's'}, \mathbf{r}_\sigma^{ls}) \quad (2.50)$$

The relative vector \mathbf{r}_σ^{ls} starts from a σ atom at \mathbf{R}_σ^v and goes to a s atom at \mathbf{R}_s^u . The atomic deformation potential vector \mathbf{m}_D is calculated analytically by using a Gaussian basis set for the $2p_z$ atomic orbital wavefunctions $\varphi(\mathbf{r})$ and the free ion potential $v(\mathbf{r})$ as described in Ref.[29]. The model presented here will be used in chapter A to compute the electron-phonon interactions for a Raman scattering analysis of few-layer graphene.

2.4. Raman scattering

2.4.1. Basic principles

Raman scattering effect Light scattering techniques provide a useful tool to study fundamental processes in solid state materials and molecules. In inelastic scattering processes, the incoming and scattered photon have different frequencies and this frequency shift is related to the characteristics of the material investigated. The process of inelastic scattering of light is called Raman effect. In the Raman process an incident photon with Energy E_i and momentum k_i is scattered in the medium resulting in a photon with different energy E_f and momentum k_f . Energy and momentum conservation give:

$$E_f = E_i \pm E_q \text{ and } k_f = k_i \pm k_q \quad (2.51)$$

with E_q and k_q the energy and momentum change of the photon before and after the scattering event. In principle, different excitations can result from Raman scattering. The most common scattering phenomenon involves phonons, so E_q and k_q can be considered as energy and momentum of the phonons being created and/or annihilated during the inelastic Raman scattering event [51].

Simplified, in Raman scattering the incoming photon creates a movement of the electrons. At different atomic positions within the vibrational mode displacement of the atom, the ability of the photon to move the electrons will be different. The latter is measured by the polarizability of the material. These vibrational modes are often called normal modes and are connected to the chemical and structural properties of the material. Since the normal modes are a property of the material,

Raman spectroscopy can be used to investigate the material properties in detail.

Light-matter interaction and polarizability In this section, we briefly describe the concept of polarizability of materials and give a classical description of the Raman effect. The macroscopic approach to explain the Raman effect is based on the action of an incident light on an extended medium creating a macroscopic polarization vector. The induced Polarization \mathbf{P} of an infinite medium with dielectric susceptibility χ can be written in terms of the electric field \mathbf{E} of the incident light as [52]:

$$\mathbf{P} = \chi \cdot \epsilon_0 \mathbf{E} \quad (2.52)$$

Here the dielectric susceptibility χ is a tensor. The electric field can be written as a plan wave:

$$\mathbf{E} = \mathbf{E}_0 \cos(\mathbf{k} \cdot \mathbf{r} - \omega t) \quad (2.53)$$

with the wavevector \mathbf{k} and frequency ω of the incident light. Since the atomic positions are changing with time, the polarizability tensor χ will depend on the atomic vibrations of the medium. If we assume that the amplitudes of the atomic vibrations at room temperature are much smaller than the lattice constant of the medium, we can expand the matrix elements of χ as a function of the generalized coordinate of a given vibrational mode Q_l in a Taylor series [52]:

$$\chi_{ij} = (\chi_{ij})_0 + \sum_l \left(\frac{\partial \chi_{ij}}{\partial Q_l} \right)_0 Q_l + \mathcal{O}^2 \quad (2.54)$$

$(\chi_{ij})_0$ stands here for the value of χ_{ij} in the equilibrium configuration. Inserting Eq.2.53 in Eq.2.51 and considering only terms to first order, we can rewrite Eq.2.51 as the sum of two contributions:

$$\mathbf{P} = \mathbf{P}_{Rayleigh} + \mathbf{P}_{Raman} \quad (2.55)$$

Here $\mathbf{P}_{Rayleigh}$ is the polarization vector oscillating with the same frequency as that of the incident light and \mathbf{P}_{Raman} is the modified polarization due to the

vibration of the atoms. By combining Eqs. 2.51-2.53 we can write the Raman contribution to the induced polarization as:

$$P_{Raman,i} = \sum_l \left(\frac{\partial \chi_{ij}}{\partial Q_l} \right)_0 Q_l E_{0,j} \cos(\mathbf{k} \cdot \mathbf{r} - \omega t) \quad (2.56)$$

In order to determine the frequency and wavevector of \mathbf{P}_{Raman} , we can describe the vibrational modes Q_l as a plane wave with wavevector \mathbf{q} as:

$$Q_l = Q_l^0 \cos(\mathbf{q} \cdot \mathbf{r} - \Omega t) \quad (2.57)$$

Here Ω is the normal mode frequency of the material that couples to the optical field so that the polarizability which is induced by the applied electric field becomes

$$P_{Raman,i} = \frac{1}{2} \sum_l \left(\frac{\partial \chi_{ij}}{\partial Q_l} \right)_0 Q_l^0 E_{0,j} \times \{ \cos[(\mathbf{k} + \mathbf{q}) \cdot \mathbf{r} - (\omega + \Omega)t] + \cos[(\mathbf{k} - \mathbf{q}) \cdot \mathbf{r} - (\omega - \Omega)t] \} \quad (2.58)$$

From Eq.2.57 we can identify two different contributions of inelastically scattered light in the Raman process. First term: The photon will be upshifted by the same frequency, resulting in absorption of a phonon, ($\omega_{AS} = \omega + \Omega$). Second term: The photon will be downshifted by the frequency Ω of the atom, resulting in an emission of a phonon, ($\omega_S = \omega - \Omega$). The first process is called Anti-Stokes, the second Stokes scattering.

Stokes and anti-Stokes Raman processes In a typical light scattering process, both the elastically and inelastically contributions are observed. Fig. 2.7 illustrates a Rayleigh and Raman spectrum where an incident light with frequency ω creates Stokes and anti-Stokes components. The Rayleigh intensity is always stronger and has to be filtered out for Raman measurements. The Stokes processes are typically stronger than the anti-Stokes processes due to phonon creation/annihilation statistics [51]. In experiments with visible light, the wavevector of the incident photon is on the order of 10^7 m^{-1} , which will create a maximum phonon wavevector in this order of magnitude. If we compare this value with the

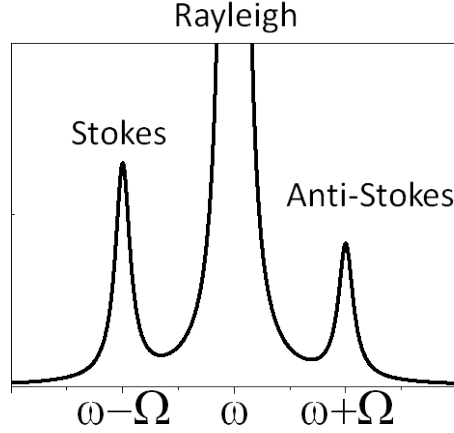


Figure 2.7.: Schematics showing the Rayleigh and the Raman spectrum. The Rayleigh intensity is always much stronger and has to be filtered out for Raman measurements. The Stokes processes are typically stronger than the anti-Stokes processes due to phonon creation/annihilation statistics.

dimensions of the first Brillouin Zone which typically is on the order of 10^{10} m^{-1} , we see that Raman scattering with visible light only probes phonons with small wavevectors and thus is limited to analyze zone-center phonons [52].

The probability to create or annihilate a phonon depends on phonon statistics, which in the case of phonons, is given by the Bose-Einstein distribution function. At a given temperature, the average number of phonons n_q with Energy E_q is given by:

$$n_q = \frac{1}{e^{E_q/k_B T} - 1} \quad (2.59)$$

with k_B the Boltzmann constant and T the temperature of the phonon system. The probability for the Stokes and anti-Stokes process differs because in the Stokes process the phonon system changes from n phonons to $n+1$ and in the anti-Stokes process from $n+1$ to n phonons. The matrix elements for both transitions are the same [51], so the intensity ratio between the Stokes and anti-Stokes signals from one given phonon can be approximated by:

$$\frac{I_{Stokes}}{I_{aStokes}} \propto \frac{n_q + 1}{n_q} = e^{E_q/k_B T} \quad (2.60)$$

where I_{Stokes} and $I_{aStokes}$ stand for the intensity measured for the Stokes and anti-Stokes peaks. Since the anti-Stokes signals are typically weaker than the Stokes signals, it is common to refer to the Stokes spectra when showing Raman spectra. If we do not refer explicitly to the type of scattering process, it is the Stokes process that is being addressed throughout this work.

2.4.2. First- and second-order Raman process

Resonance Raman scattering In typical experiments, the laser excitation energy is much higher than the phonon energy. Although the exchange in energy between light and the medium is transferred to the atomic vibrations, it is the electron system that mediates the light-matter interaction. If the energy of the photon does not match a real transition in the electronic band structure, the electron that absorbs the energy is said to be in a virtual state. From there, it can couple to the lattice. If, however, the laser photon energy matches a real electronic transition from an occupied initial state to an unoccupied final state E_{if} , the probability of this process can exceed the former by orders of magnitude ($\approx 10^3$, [51]). This process is called resonance Raman effect. The same is valid if the scattered light ($E_{Laser} \pm E_q$) is equal to an electronic transition E_{if} . Therefore, the Raman intensity should increase when $E_{Laser} \rightarrow E_{if}$, being resonant with incident light and $E_{Laser} \rightarrow E_{if} \pm E_q$, being resonant with scattered light. The Raman intensity profile is given by [51]:

$$I(E_{Laser}) = \left| \frac{A}{(E_{Laser} - E_{if} - i\gamma_r)(E_{Laser} - (E_{if} \pm E_q) - i\gamma_r)} \right|^2 \quad (2.61)$$

The full width half maximum (FWHM) of each peak in the Raman intensity profile is the resonance window width γ_r , which is related to the lifetime of the excited states in the Raman scattering process. It gives the time delay between absorption of a photon and emission of a phonon. The resonance effect is important in nano-scale structures, as the Raman signal is in general very weak due to the small size of the samples.

Higher-order Raman processes A detailed description of the Raman spectrum of graphite and graphene will be given in chapter A. For the discussion, higher-order Raman processes will be important. The order of the Raman process is given by the number of scattering events that contribute to the Raman process. In the first-order Stokes Raman scattering event, the photon exchange energy creates one phonon in the crystal with a very small momentum ($q \approx 0$ [51]). If the scattering involves two, three or more phonons the Raman process is called second-order, third-order, .. respectively. First-order processes give the basic quantum of vibration, higher-order processes can give very important information about overtones ($n \cdot E_q$) and combination of several phonon modes ($E_{q1} + E_{q2}$). One interesting point is that for higher-order processes the restriction $q \approx 0$ in the first-order process is relaxed. A photoexcited electron at k_i can be scattered to $k_i + q$ and with a second phonon with wavevector $-q$ backscattered to its original position, which allows the recombination with their corresponding holes. The propability of such processes is usually very small and not important for solids, but as will be shown in chapter 6, in the case of sp^2 systems there are Raman signals from $q \neq 0$ scattering events.

The Raman spectrum of 1-layer graphene The Raman spectrum of 1-layer graphene exhibits different features. The two most prominent peaks are the G-peak appearing at 1582 cm^{-1} and the 2D-peak appearing at about 2700 cm^{-1} , when using 2.41 eV as excitation laser energy. Besides these two modes, different peaks appear in the spectra, as shown in Fig. 2.8(a) [52]. There is an additional peak with low intensity near 2400 cm^{-1} , called G*-band. Fig. 2.8(a)(ii) shows the Raman spectrum for 1-layer graphene with some disorder or defects in the sample, where an additional peak, labeled D, at about 1350 cm^{-1} appears. Close to 1620 cm^{-1} another disorder-induced mode appears, called D'. Fig.2.8(b) depicts the relevant physical processes responsible for the peaks in the Raman spectrum of graphene [52]. This is the common picture used in the literature to explain the Raman scattering in graphene. We start with (i): The G peak is associated with the doubly degenerated iTO and LO (see Fig.2.6 from the last section) phonon mode with E_{2g} symmetry at the Γ -point in the Brillouin zone (BZ). A photo-excited electron state scatters within the K-point with a $q \approx 0$ phonon.

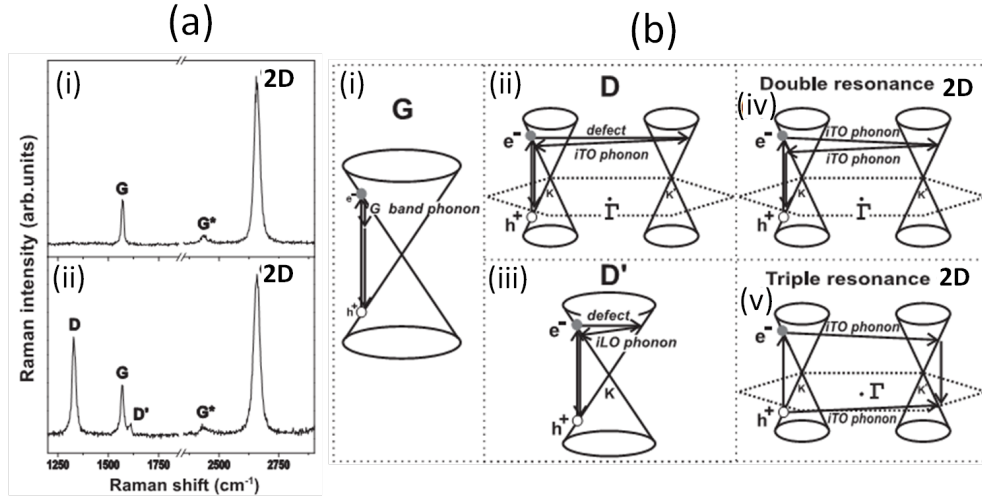


Figure 2.8.: (a) The (i) Raman spectrum of a defect free monolayer graphene showing the main Raman features, G, G* and the 2D-mode with a laser excitation energy of 2.41 eV. And (ii) the Raman spectrum of a defective monolayer, in which two disorder-induced D and D' Raman modes appear additionally. (b) The (i) first-order Raman process which gives rise to the G-mode. Second-order Raman process showing the (ii) inter-valley D-mode and (iii) intra-valley D'-mode. (iv) Second-order Raman process involving two phonons and (v) a possible triple resonance Raman process. All figures are taken from Ref.[52].

The latter is a first-order process. Scattering within the K (K')-point is called intra-valley scattering. (ii): The photo-excited electron scatters elastically by a defect and a iTO phonon from K to K' and back. Scattering from K to K' points in the hexagonal BZ is called inter-valley scattering, involving $q \neq 0$ phonons. The latter is a second-order process. It can generally be distinguished between first- and second-order process by the frequency shift of the second-order Raman peaks with the laser wavelength used. For example, the disorder-induced D-mode shifts with laser excitation energy about $53 \text{ cm}^{-1}/\text{eV}$ [53]. (iii): Disorder-induced intra-valley process involving a $q \neq 0$ iLO-phonon. (iv): In the double-resonance process the photo-excited electron is inelastically scattered by a iTO phonon with wavevector \mathbf{q} from K to K' point and then back scattered by a iTO phonon with opposite momentum. In a double-resonance Raman process with three scattering events, two resonance conditions have to be fulfilled. The intermediate state is always a real electronic state and either the initial or the final state is a real electronic state. Because of the special band structure of graphene, with an

almost symmetric conduction- and valence-band, this can lead to case (v), the triple resonance. The electron and hole are scattered from K to K' point, where electron-hole generation is a resonant process, both electron and hole scattering are resonant and electron-hole recombination at the opposite side will be resonant. This triple resonant condition might explain why the 2D-band in 1-layer graphene is more intense than the G-band [52].

3. Methods

The following chapter describes the methods and techniques used in order to fabricate and characterize the samples.

3.1. Sample preparation

Writing with a pencil on a piece of paper transfers single flakes of graphite on the paper. Among these flakes single layers of graphene can presumably be found. But, the theoretical theorem of Mermin and Wagner says that due to the periodical structure of carbon atoms in a hexagonal lattice an infinite two-dimensional system cannot be thermodynamically stable in 3-dimensional space. Long-wave fluctuations would lead to the destruction of the long-range order of the 2-dimensional lattice [8, 9]. In 2005, Novoselov et al. described the existence of single graphene layers fabricated from graphite [54]. Further experimental and theoretical publications on this topic proved that the fluctuations can be suppressed by anharmonic coupling of bending and elongation modes [55–57]. Hence, a 2-D structure can exist, but would feature huge differences in the third dimension perpendicular to the plane [12]. Furthermore, graphene owes its discovery a subtle optical phenomenon: Graphene deposited on a silicon-dioxide covered silicon wafer substrate is visible to the naked eye with an conventional optical microscope [58].

3.1.1. Mechanical exfoliation

So far the method to fabricate graphene by mechanically pulling off one-atom thick layers of graphite as described by Novoselov et al. is still the method of choice for most research groups worldwide. This simple and inexpensive process

allows to produce Graphene with high quality and up to sizes of several tens of μm . An additional advantage of the exfoliation technique is that the graphene samples transferred on a silicon substrate can be identified with a conventional microscope. Blake et al. demonstrated that a silicon oxide layer of 300 nm or 100 nm thickness optimizes the contrast between the single-atom carbon layer and the substrate [58]. A change of the SiO_2 -layer thickness of only five percent leads to the complete disappearance of the contrast between graphene and the substrate [54].

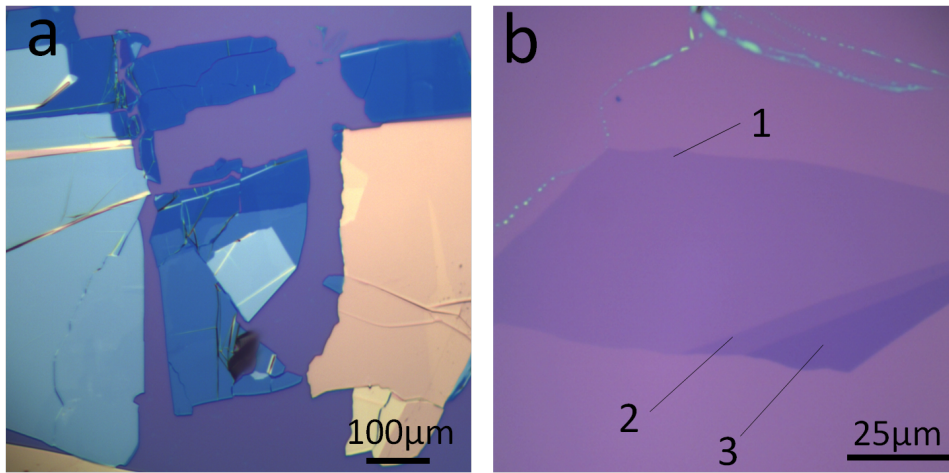


Figure 3.1.: (a) Illustration of the correlation between the thickness of the graphene/graphite layer and the color of the material under an optical microscope with a halogen lamp as light source. The silicon substrate appears purple and defines the background, the graphite layers appear from yellow over light blue till dark blue in descending number of layers. (b) Area with one, two and three layers of graphene on a silicon substrate. A very weak contrast between the 1-layer graphene and the background can be distinguished.

Fig.3.1(a) illustrates the correlation between the thickness of the graphene/graphite layer and the color of the material under an optical microscope with a halogen lamp as light source. The silicon substrate appears purple and defines the background, the graphite layers appear from yellow over light blue till dark blue in descending number of layers. Fig.3.1(b) shows an additional area with one, two and three layers of graphene on a silicon substrate. A very weak contrast between the 1-layer graphene and the background can be distinguished.

We describe here the method we used to fabricate graphene, which is based on the technique developed by Novoselov et al. [54]. The starting point is the raw material: Natural graphite pieces of the company NGS Naturgraphit GmbH, Germany (www.graphit.de). The single flakes are about 10-20 mm big and consist of 80-99.5 % of carbon. All fabrication steps described in the following are carried out in a clean room in order to minimize contamination of the materials.

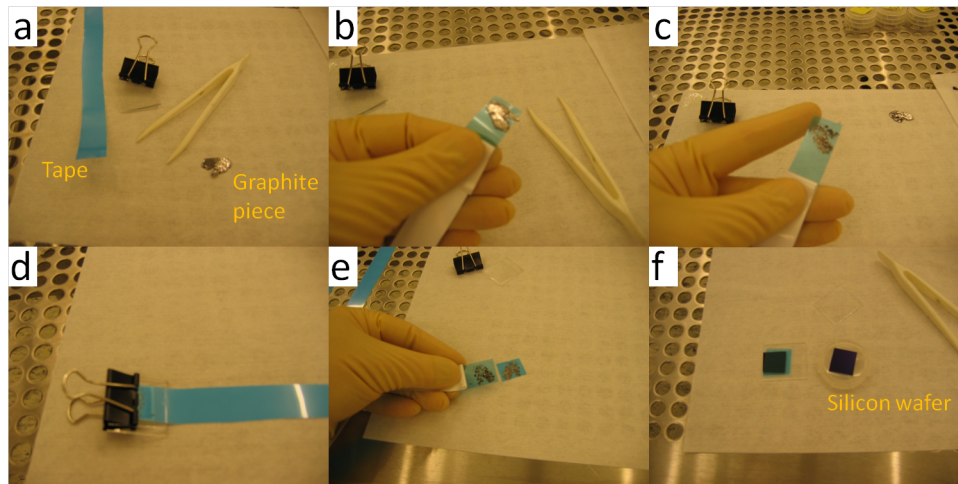


Figure 3.2.: Visualization of the mechanical exfoliation process. (a) starting materials: piece of the tape, paper clamps, a plastic tweezer and the natural graphite flake. (b) the graphite flake is stuck to the tape to get a first copy of the flake. (c) the flake is subsequently split into thinner and thinner layers by sticking together and pulling-off of the tape. (d) and (e) show how to use the paper clamp to assure a constant homogenous pressure. (f) transfer to a silicon wafer.

First the thick piece of graphite is stuck to a special tape and pulled-off carefully to get a copy of the graphite flake as homogeneous as possible. The tape (Nitto Denko, Type Lensguard 7568, www.nitto.com) allows an especially residual free transfer of the single layers. The flake on the tape is subsequently split into thinner and thinner layers by sticking together and pulling-off of the tape. Ensuring a constant and homogeneous pressure of the tape on the graphite flake, the samples are clamped between two glass cover-slides with a paperclip for ≈ 5 minutes. As soon as the graphite appears less reflective, the flake is glued on a silicon substrate with the tape and clamped with paperclips for 12 hours. The silicon substrate should be as contamination-free as possible and is cleaned

directly before usage by means of an oxygen-plasma (Diener, Femto Low Pressure Plasma facility, 100 W for 5 minutes). Important for the exfoliation procedure of the tape from the silicon wafer is the pull-off velocity. The process should take about 60 seconds for a tape area of 2x2 cm. Fig.3.2 visualizes the single steps. By means of an optical microscope the single flakes can be roughly identified. An exact determination of the number of graphene layers of one or two is described in section 3.1.5.

3.1.2. Transfer process

For further spectroscopic analyses, it is necessary to transfer single graphene flakes on silicon wafers obtained from the mechanical exfoliation process to substrates with different optical properties. To this end, a wet-chemical procedure developed by Reina et al. was slightly modified. [59]. Fig.3.3 shows the procedure in detail.

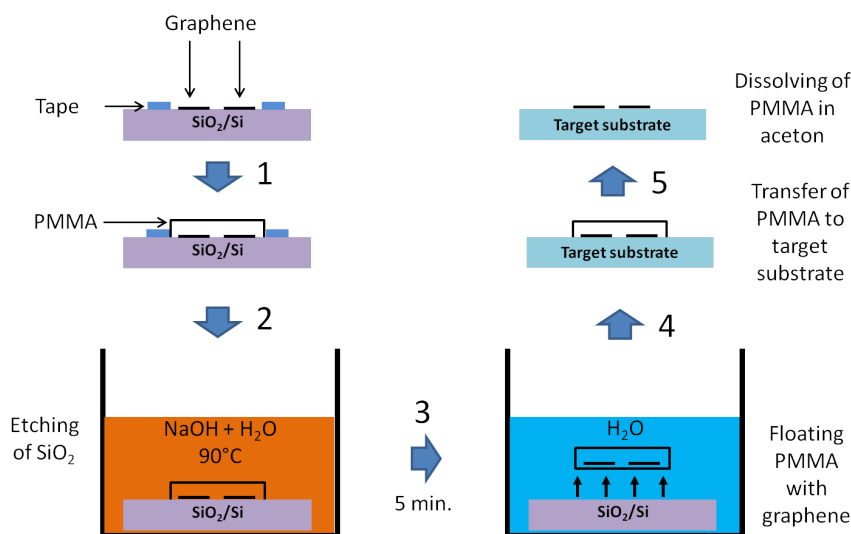


Figure 3.3.: Illustration of the graphene flake transfer method. The graphene on the silicon wafer is covered with a thin layer of PMMA. In an aqueous solution of NaOH the underlying SiO_2 is partially etched to release the PMMA/graphene film. The PMMA/graphene film is rinsed several times in deionized water and transferred to the target substrate. In the last step the PMMA is dissolved in Aceton.

A hole of 3x3 mm is cut into the Nitto Denko Lensguard 7568 tape and the tape is glued on the silicon substrate in a such a way that the graphene flake to

be transferred is in the center of the hole. This process assures to transfer only the area and graphene flake of interest. All parameters in the following steps are optimized for a 3x3 mm transfer area. 1 μ l PMMA/Anisol 8 wt percent is pipetted on the opening and dried for about 20 minutes. To remove the oxide layer beneath the graphene, it is partially etched off with an aqueous NaOH solution (4 g in 100 mL H₂O, 90°C, ca. 2-5 minutes). The PMMA is rinsed together with the wafer in deionized water to remove residues of the NaOH solution and is subsequently transferred to the target substrate. Again, the sample is rinsed with water twice and dried on a hot plate (50°C, ca. 2 min) in order to let the water evaporate. To remove the last residues of the NaOH-base, the sample is rinsed with water another time. The PMMA is dissolved in acetone for 60 s. Afterwards, PMMA residues can be removed by dipping the sample in acetone several times. With this process it is possible to transfer graphene flakes to any substrate. By carefully following every step of the described procedure the yield of the transfer process should be 100%. Whenever it was necessary to have graphene samples on a transparent substrate the flakes have been transferred with this method. Doping effects due to the transfer process are excluded by comparing the Raman G-peak before and after the transfer on an identical substrate [60].

3.1.3. CVD graphene

This method has been established over the last few years as the only one that can fabricate graphene on a large scale, which means $>1\text{ mm}^2$. CVD stands for chemical vapor deposition and describes a technique that grows mono- and few-layer graphene on, for example, nickel or copper [61, 62]. Copper foil is heated to a temperature of 1000°C in an atmosphere of methane and hydrogen. Depending on the copper microstructure single areas of monolayer graphene are produced with a charge carrier mobility of 4050 cm^2Vs [62]. Graphene fabricated according to the exfoliation method described in chapter 3.1.1 has a charge carrier mobility of up to 40000 cm^2Vs on silicon substrates [63]. If not stated differently, all graphene samples for the research performed in this work are produced by mechanical exfoliation.

3.1.4. Samples for optical spectroscopy

Graphene flakes fabricated by mechanical exfoliation have an average lateral size of several tens of micrometer. For the time-resolved measurements described in chapter 3.2, it is, necessary to find a possibility to control the position of the samples in order to focus the invisible infrared laser pulses on the samples. Two methods were applied for this purpose. The first uses deposition of a pinhole structure around the graphene flake to be prepared on the substrate by means of photolithography in the clean room. The geometry is shown schematically in Fig.3.4.

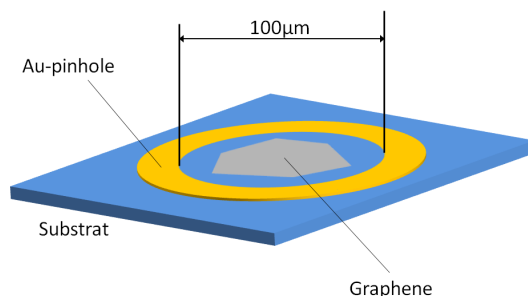


Figure 3.4.: Illustration of the sample structure used in optical transmission experiments. A graphene flake is transferred to a transparent substrate and a thin (50nm) Au-pinhole with an inner diameter of $100\ \mu\text{m}$ is evaporated by means of photolithography around the graphene flake. In an alternative method described in the text a commercial steel-pinhole with an identical inner diameter is positioned on top of the graphene flake. The pinhole is used to align the IR-laser beams with the graphene flake investigated and to assure equal conditions between different experiments.

A Gold pinhole with an inner diameter of $100\ \mu\text{m}$ and a height of 50nm is deposited on the substrate by means of thermal evaporation. Due to the various steps of the photolithography process and the very low contrast between graphene plus photoresist and the substrate in the mask-aligner (Suess Micro Tec MA6) the efficiency of this method was unfortunately very low. In a different method a steel pinhole (Edmund Optics) with an outer diameter of 10 mm and an inner opening of $100\ \mu\text{m}$ is fixed with a tape on the substrate. Here, less process steps

are necessary and without the treatment of the sample with various solvents and the photoresist possible damaging of the graphene samples can be avoided.

3.1.5. Characterization of single flakes

Raman scattering spectrum For determining the exact number of layers of graphene with one to two layers, Raman scattering works best [64]. Raman-spectroscopy is a common non-destructive technique, described in greater detail in chapter 2.4. Fig.3.5 shows the high frequency part of the Raman spectra of 1- and 2-layer graphene.

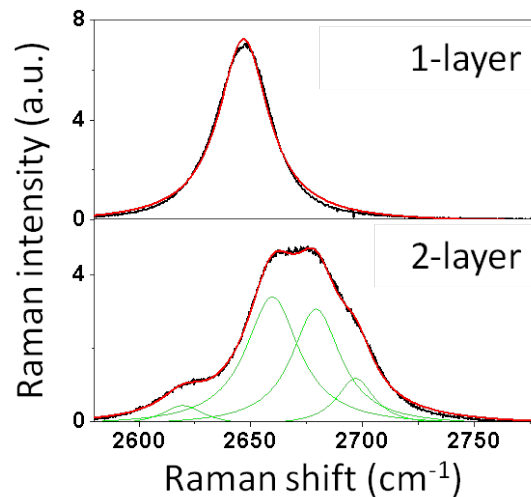


Figure 3.5.: High frequency Raman scattering spectra of a 1-layer graphene (top graph, black line) and 2-layer graphene (lower graph, black line) showing the 2D-peak. The red and green solid lines represent fits with a Lorentzian resonance model. While the 1-layer 2D-peak is almost a single Lorentzian resonance the 2-layer peak is a superposition of four Lorentzian lines ($\omega_{FWHM} \approx 30 \text{ cm}^{-1}$) with a distinctive shoulder on the low frequency side. Additionally, the central frequency of the 2D-peak is increasing with increasing number of layers for samples on Si/SiO₂ substrates. Thus, the 2D-peak can be used to distinguish between one and two layers of graphene.

The origin of the single resonances are explained in detail in chapter A. A closer look at the 2D peak in figure 3.5 reveals a distinct evolution in the shape of the peak. In case of 1-layer graphene, the peak consists of a single Lorentzian resonance while in the case of two layer graphene of the superposition of four. The 2D-peak of bilayer graphene exhibits a characteristic shoulder on the low energy

side and can be reproduced very well with four single Lorentzian peaks with a full width at half maximum of about 30 cm^{-1} each. However, the shape of the 2D-peaks of three and of four layers graphene are distinctly different (see chapter A). The number of transitions in the 2D band is proportional to the number of layers [64]. Due to the small energy difference between these transitions, changes in the 2D Raman peak of a system of three and more layers of graphene are marginal and result only in a change of the 2D-peak shape (see chapter A). The 2D-peak of the Raman spectrum of graphene can, thus, be used to determine the number of layers qualitatively. For an exact identification of the number of layers the actual height of the graphene flake has to be measured, for example by means of an atomic force microscope.

Atomic force microscopy (AFM) The actual height of graphene and few-layer graphene flakes on glass substrates was measured with atomic force microscope. Fig.3.6(a) displays, for example, an optical microscope image of a flake, on a Si/SiO₂ substrate appearing as the purple background, which consists of several areas of a different number of layers. The same flake was transferred to a transparent substrate and measured by means of AFM and is shown in Fig.3.6(b) in a color-coded image. Different colors give different height, as given by the color scale on the right side of the image. The brighter white spots visible on the image are probably due to dust particles on the substrate. Several steps on the graphite flake, representing areas with different number of graphene layers, were scanned with AFM and the measured height is displayed in Fig.3.6(c). 1-layer graphene has a height of $0.8\pm 0.1\text{ nm}$ on a glass substrate, 2-layers on the other hand $1.3\pm 0.1\text{ nm}$. Extrapolation of the linear fit shown by the red line in graph Fig.3.6(d) to the y-axis gives an offset of 0.35 nm . The last value is in accordance to literature values of AFM measurements of 1-layer graphene on glass substrates [11], and is probably due to water adsorbates between glass and the graphene layer. The thickness of a single layer of graphene was determined from these measurements to $0.39\pm 0.1\text{ nm}$.

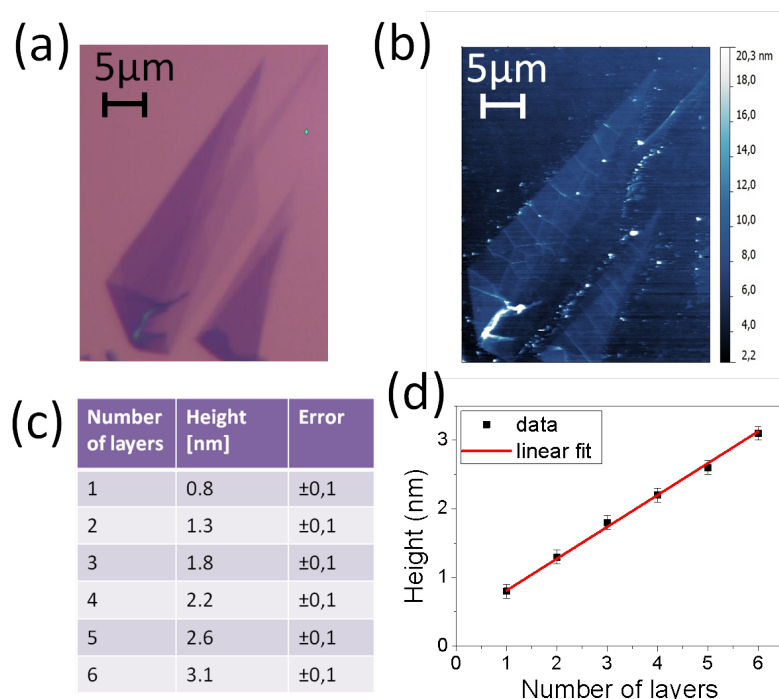


Figure 3.6.: (a) Optical microscope image of a flake, on a Si/SiO₂ substrate appearing as the purple background. The same flake was measured by means of AFM and is shown in (b) in a color-coded image. The brighter white spots visible on the image are probably due to dust particles on the substrate. (c) and (d) Measured height values of graphene and few-layer graphene together with a plot displaying the linear increase with increasing number of layers.

3.2. Time-resolved spectroscopy

Linear optical spectroscopy can give valuable information about the various characteristics of carbon nanostructures, for example electronic band structure, phonons, plasmons, defects etc. Using other, non-linear effects of optical spectroscopy, however, additional and fundamental properties of the analyzed materials can be studied like non-linear characteristics, non-equilibrium phenomena or transport properties [22]. Exciting non-equilibrium charge carrier populations with laser pulses is the method of choice to analyze the dynamics of excited states. With ultrafast laser pulses in the femtosecond regime, it is possible to study a variety of phenomena concerning relaxation processes and transport dynamics in carbon nanostructures [65]. A widely used method for ultrafast optical spec-

troscopy is the one known as pump-probe spectroscopy. The following paragraph explains this technique in greater detail.

3.2.1. Differential transmission pump-probe spectroscopy: method

In the most simple version, known as degenerate pump-probe, the laser beam of an ultrafast laser system is split into two parts. The sample is excited with one part and the second part probes the changes induced by the first laser pulse. Temporal dynamics are obtained by mechanical, typically linear modifications in the optical path of one pulse relative to the other. For sufficient thin samples the temporal resolution is solely limited by the temporal pulse width of pump and probe pulses and their cross-correlation. Non-degenerate pump-probe experiments are realized with two synchronized laser beams of different wavelength or optical-parametric oscillators in order to expand the available spectrum of ultra-short pulse. The laser systems of this work are described in greater detail in the next section. The method of choice for the experiments described in this work is a time-resolved differential transmission spectroscopy (DTS). A pump pulse generates a charge carrier distribution from the equilibrium population which is probed by a second, temporally shifted pulse of different energy and comparatively reduced intensity. The spot size of the probe at the sample is ideally considerable smaller than that of the pump so that it probes a region of uniform photoexcitation. The DT signal normalized with respect to the transmission is given by:

$$\frac{\Delta T}{T} = \frac{T_{exc} - T_0}{T_0} \quad (3.1)$$

with T_{exc} the sample transmission with the pump pulse and T_0 the transmission without the pump pulse. The differential transmission spectrum can be obtained either by varying the wavelength of the probe laser or by spectrally analyzing the transmitted probe energy with a spectrometer if a broadband ultrafast source is used as the probe. The strength of the pump-probe technique is its ability to obtain time-resolution limited only by the laser pulse width and the ease to detect the transmitted signal. Measuring very small differential transmission on

the order of 10^{-4} , care has to be taken to minimize all noise components in the experiments.

3.2.2. Laser system for pump-probe spectroscopy

The essential part of a time-resolved pump-probe experiment is the laser system that generates ultrashort laser pulses. Figure 3.7 shows the core parts of the setup for generating ultrashort pulses for pump-probe spectroscopy.

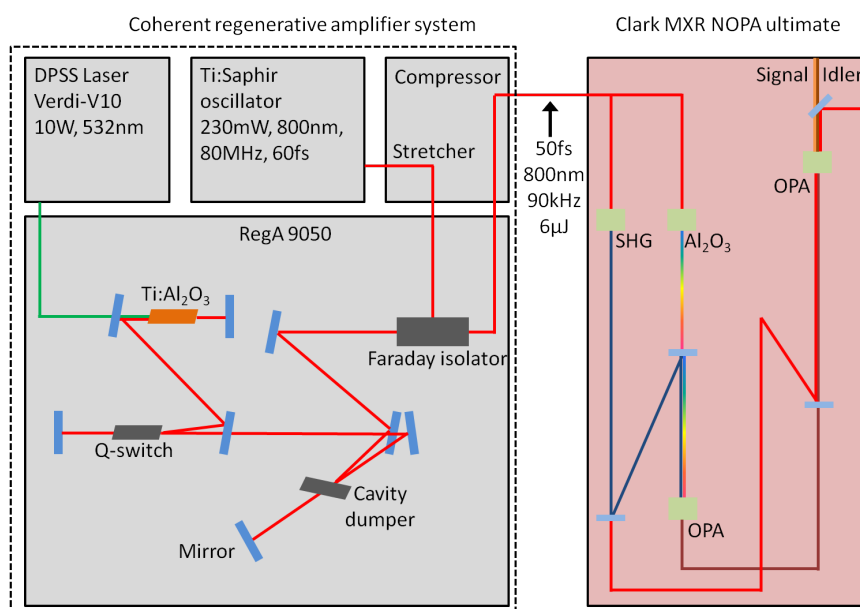


Figure 3.7.: The laser setup used to create ultrashort IR and MIR-laser pulses. The commercial regenerative amplifier system Coherent RegA 9050 produces 60 fs pulses with a repetition rate of 90 kHz and a fundamental of 800 nm. Part of the 800 nm pulses are used to pump an optical parametric amplifier (Clark MXR, NOPA ultimate) which extends the available wavelength range from 950 nm-1550 nm and from 1620 nm-4800 nm. A detailed description of both systems is given in the text.

Amplifier system Starting point of the laser system is a Ti:Sapphire oscillator (Coherent, Vitesse 800) with an independent Nd:YVO4 continuous wave pump laser of double frequency (Coherent, Verdi 2W). The specifications of the oscillator are 60 fs, 5 nJ with a repeat rate of 80 MHz and a central wave length

of 800 nm. The nJ-pulses of the oscillator are coupled into a regenerative amplifier system (Coherent, RegA 9050) with the resonator shortly beneath the laser threshold by means of a Q-switch. The ultrashort pulses of the oscillator are stretched in time by means of a multi-pass holographic grating before the amplification process. This step ensures that the peak intensities in the amplification process are low enough to avoid possible damage to the laser medium in the amplification stage. The efficient population inversion causes a pulse amplification of about 4-5 orders of magnitude within 20 round trips. An acousto-optical modulator regulates how single pulses are coupled into and released from the system. In the next step, the amplified nanosecond pulses are compressed in time to about 60 fs by means of another holographic grating pair with reverse dispersion. The output of the regenerative amplifier system is $6\mu\text{J}$ per pulse in average for a central wave length of 800 nm and a pulse length of about 60 fs with a repetition rate of 90 kHz.

Optical parametric amplifier 90 percent of the fundamental of the regenerative amplifier system is used to pump a optical parametric amplifier and to extend the available wave length range into the middle infrared regime (Clark MXR, NOPA ultimate). Two optical parametric amplification steps enable a continuous spectral range from 950 nm to 1580 nm (signal) and 1620 nm to 4800 nm (idler) respectively. Signal, idler and the residual 800 nm exit the NOPA in a collinear way, therefore it is necessary to effectively separate all beams according to their wavelength for further applications. In order to cut out the fundamental 800 nm a custom made Calcium-Fluoride (CaF_2) based window with a multilayer dielectric coating effectively reflecting the 800 nm and with a high transmittance for the signal and idler wavelengths is used. CaF_2 has the advantage of a high transmittance in the spectral range from 250 nm up to $7\mu\text{m}$ [66]. To separate signal and idler a germanium-window is used. Germanium is a semiconductor with a room temperature bulk band gap of 0.67 eV. So optical windows made of germanium are ideal for IR applications with its broad transmission range and opacity in the visible portion of the spectrum. Figure 3.8 shows several examples for spectra recorded with a monochromator (Horiba Jobin Yvon, MicroHR

140 with Gold-Grating) and a IR-photodetector (Infrared Associates, HgCdTe MCT-5-N) tuning the signal and idler at different photon energies.

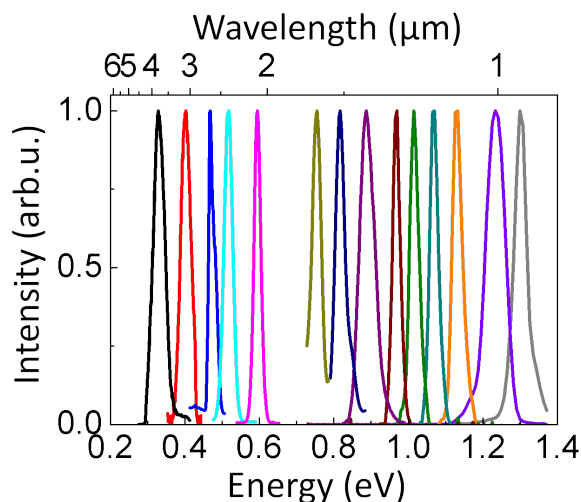


Figure 3.8.: Measured normalized output pulses of the NOPA system as a function of energy where the system has been tuned at different photon energies. This energy range can be used for the probe pulses in the pump-probe experiments.

Pump-Probe setup The remaining 10 percent of the fundamental of the amplifier system is used as pump pulse to optically excite the samples investigated. By means of a mechanical delay stage the optical pathway of the pump pulse can be delayed. This spatial displacement causes a difference in the arrival time between pump and probe pulse at the sample so that time resolved experiment can be performed with a maximum delay time of 1 ns. Before every measurement the spectrum of the signal and idler pulses was carefully checked with a spectrometer. To avoid dispersion of the probe pulses only spherical mirrors are used in the optical setup. The pump pulse is focussed down to a diameter of about $150 \mu\text{m}$ on the sample, the probe pulse to about $80 \mu\text{m}$. The change in the probe pulse is detected after passing through the sample by a photodetector diode (Infrared Associates, HgCdTe MCT-5-N) and lock-in technique (Stanford Research Systems, SR810). The temporal resolution of the setup lies between 150fs-250fs depending on the wavelength of the probe pulse.

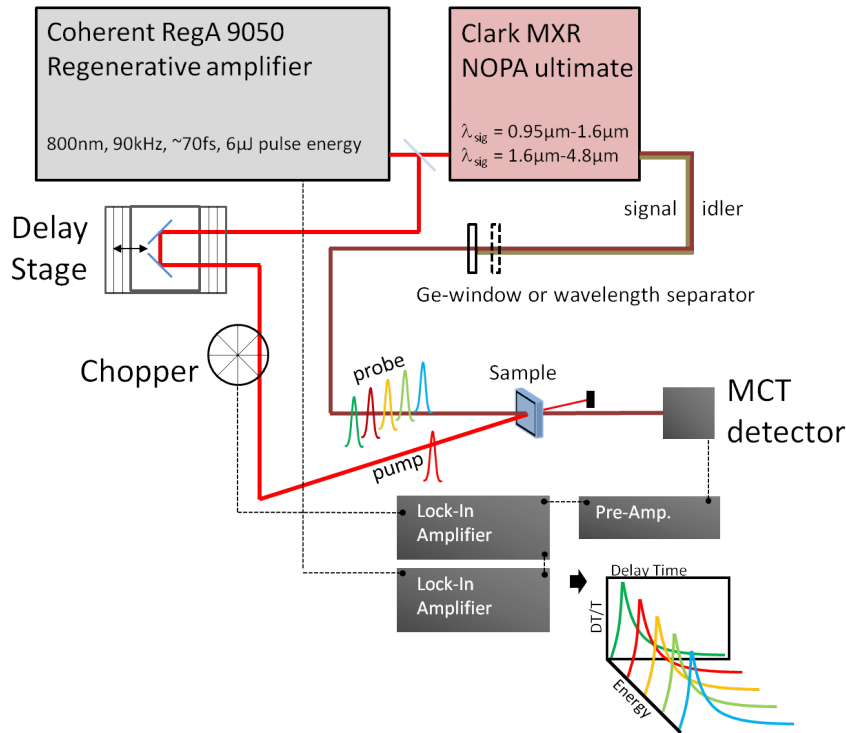


Figure 3.9.: Overview of the experimental setup and the measurement technique for the differential transmission experiments. Part of the fundamental of the amplifier system is chopped and serves as the pump pulse, the remaining is used to feed the NOPA ultimate. Signal and idler serve as the probe beam. The pump and probe beams are focused onto the sample and the change of the probe beam is detected with a liquid nitrogen cooled HgCdTe-photodiode while the pump is delayed in time with a mechanical delay stage. The signals are detected and filtered with two lock-in amplifiers and the normalized transmission change is analyzed with a computer.

3.3. Raman setup

Section 3.1.5 showed that Raman scattering offers a fast and nondestructive method to distinguish between a 1- and 2-layer graphene samples. The following will give a brief overview of how Raman scattering measurements of graphene and graphite samples are performed. Raman scattering on graphene and graphite was measured by a commercial system (Horiba Jobin Yvon, T64000). The system consists of a triple spectrometer with a confocal microscope and a liquid nitrogen cooled CCD-camera. This instrument offers three different modes of operation for performing Raman scattering experiments. In the direct, single

mode, only one spectrometer is used with a choice of two different gratings, 300g/mm and 1800g/mm. This is used for studying the high wavenumber region from $> 120\text{cm}^{-1}$ with good signal to noise ratio. In another configuration, two spectrometers are employed for the double, subtractive mode. This mode enables the measurement of Raman spectra up to 4cm^{-1} from the laser line wavelength. In the triple, additive mode, three spectrometers with an overall focal length of $3 \times 0.64\text{m}$ can be used to gain a resolution of up to 0.1cm^{-1} . The double and triple mode are used to probe the wavenumber region from $> 4\text{cm}^{-1}$ with a high spectral resolution. A commercial Argon/Krypton gas laser system operates as an excitation laser (Coherent, Innova 70C) with discrete wavelengths 458 nm, 514 nm, 568 nm, 647 nm and 752 nm. The laser beam is focused on the sample by a 100x objective to a spot size of about $1.5\mu\text{m}$ and the laser intensity is kept below the damage threshold for graphite and graphene (Zit et al. paper). The Raman signal is collected in a back scattering configuration from the same objective used to focus the laser spot. All measurements are performed in ambient conditions and at room temperature.

4. Influence of carrier density on the electronic cooling channels of 2-layer graphene

In the following section, we determine the energy loss rate of photoexcited hot carriers in 2-layer graphene and discuss the relevant mechanisms of carrier cooling and their connection to the initial carrier temperature. The electronic cooling dynamics in a single flake of 2-layer graphene are investigated by means of femtosecond transient absorption spectroscopy in the energy range 0.25 eV - 1.3 eV. From the transients we extract the carrier cooling curves for different initial temperatures and densities of the photoexcited electrons and holes. We identify two regimes of carrier cooling dominated first by optical and then acoustic phonon scattering. Interestingly, for increasing carrier densities the crossover between the two regimes occurs at higher carrier temperatures since cooling via optical phonons experiences a bottleneck. In contrast cooling via acoustic phonons, which are less sensitive to saturation, shows an increasing contribution at high carrier density.

4.1. Physical background of carrier cooling in graphene

The dynamics of carrier cooling is of particular interest in carbon based low dimensional structures, such as carbon nanotubes and graphene, because of their extraordinary mobilities and current densities in devices [18] in the presence of strong carrier-phonon interactions [19]. Hot carriers are expected to scatter with optical phonons as long as their energy with respect to the bottom of the band is above the optical phonon energy $\hbar\Omega_{op}$ (≈ 195 meV G-mode in graphene, see Fig.4.1(b)). In proximity to this energy, acoustic phonons become the dominant cooling channel for equilibrating the electronic system with the lattice. Acoustic phonons are also responsible for the decay of the emitted optical phonons via anharmonic interactions [67]. We consider the carrier cooling in 2-layer graphene, as this material is gaining an increasing interest in photonics and optoelectronics, where it can be used in photodiodes [20] and lasers [68]. We look at the dynamics of carriers as a function of energy and the photoexcited carrier density and discuss the main mechanism which returns the excited system back to the room temperature equilibrium. It is crucial to understand how hot carriers lose energy in different regimes of photocarrier densities, as this process is one of the limiting factors regarding the performance of high-speed devices, like photodetectors [20]. We note that, although the mechanism by which carriers gain energy is different for applied electric fields and photoexcitation, the process by which they lose energy to the lattice (i.e. by the emission of phonons) is the same in both cases [22]. Therefore, information gained by optical studies is useful in understanding high-field transport and vice versa. One advantage of optical spectroscopy is that it provides the best means of determining the dynamics of the hot carrier distribution functions. In addition, the physics of hot-carrier relaxation has triggered a considerable interest from the perspective of theoretical modeling [69, 70], but has seen limited experimental investigations, mainly focused on epitaxial graphene, which is known to be heavily doped and thus gives a non-intrinsic response [71].

4.2. Ultrafast carrier dynamics in graphene

Experimental methods The 2-layer graphene flake investigated in this section was prepared by mechanical exfoliation of natural graphite. This method is described in detail in section 3.1. Fig.4.1(a) shows an image of the sample taken with a standard optical microscope in transmission with a halogen lamp as light source. Inside the circle, there are two brighter areas which define the background glass substrate, the darker grey areas represent instead the 2-layer flake. Due to the small absorption (see section 4.3) of two layers of graphene in the visible spectrum, there is only a weak contrast between graphene and the background. The corresponding Raman scattering spectrum is shown in figure 4.1(b) from 1000 cm^{-1} up to 3500 cm^{-1} in the lower panel and a zoom of the 2D peak in the upper panel. The number of layers, two in this case, was checked from the shape and position of this high energy Raman mode and the flake height measured by means of atomic force microscopy. Fig.4.1(c) shows a Raman intensity map of

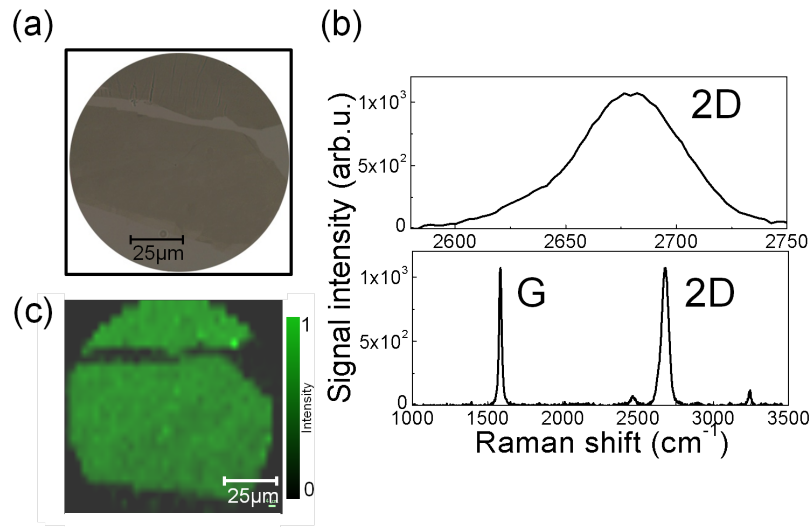


Figure 4.1.: (a) Image of the 2-layer graphene flake taken with a standard optical microscope in transmission. Inside the circle, there are two brighter areas which define the background glass substrate, the darker grey areas show the 2-layer flake. (b) Raman scattering spectrum of the 2-layer graphene with a zoom of the 2D peak in the upper graph. No defect-induced D-peak [49] can be observed in the lower spectrum. (c) Raman intensity map of the integrated 2D Raman peak intensity. Each pixel gives the integrated intensity in a normalized color-scale. The horizontal and vertical step size is $1\ \mu\text{m}$.

the integrated 2D-peak area measured with a 568 nm laser. Here the full area of the field of view shown in Fig.4.1(a) has been scanned and a Raman spectrum was taken at each pixel with a scanning step size of $1\mu\text{m}$. The image shows the value of the integrated 2D peak from each spectrum in a normalized color-coded scale. This Raman intensity map coincides with the optical microscope image and demonstrates the homogeneity of the sample investigated. Defect induced D-Peaks at a position around $\approx 1350\text{cm}^{-1}$ [49] could only be measured at the edges of the flake which indicates the high quality of the sample.

In order to measure the differential transmission spectrum of the 2-layer graphene the setup described in section 3.2 was used. For all measurements, the 800 nm fundamental of the amplified laser system is used as the excitation pump pulse, while the probe photon energy is tuned in the energy range from 0.25 eV - 1.3 eV (4800 nm - 950 nm). The change in the transmission of the probe pulse is detected as a function of (i) the time delay between pump and probe and (ii) the probe photon energy. All measurement are performed in ambient conditions and at room temperature.

Carrier dynamics at different probe photon energies Before discussing the full energy spectrum, we will first present the dependence of the carrier dynamics on the probe photon energy. Figure 4.2(a) shows a scheme illustrating the measurements performed together with a sketch of the electronic band dispersion calculated for 2-layer graphene at one of the K -points. For a full description of the electronic band structure see sections 2.1.2-3. The 2-layer graphene flake is probed at two different photon energies, one close to the pump (blue) and one closer to the Dirac point (green). The respective differential transmission dynamics are shown in Fig.4.2(b) for a probe energy of 1.28 eV (blue curve) and 0.3 eV (green curve) in the first 6 ps after photoexcitation. The photocarrier density is $5.0 \times 10^{11}\text{cm}^{-2}$. At negative times ($\Delta t < -200$ fs) before the onset of the pump pulse the transmission change $\Delta T/T$ is zero. At about $\Delta t = -200$ fs $\Delta T/T$ starts to increase within 200 fs to a maximum value. This rise is attributed to the time it takes for the photoexcited carriers to scatter and bleach the optically coupled states [72]. The rise time observed here is limited by the temporal resolution of our setup and the position of the maximum transmission change is defined as

$\Delta t = 0$. We focus now on the dynamics at $\Delta t > 0$ fs. While we observe an almost monoexponential decay of ≈ 4 ps at 0.3 eV, at high energy, 1.28 eV, the dynamics exhibit a faster decay of 500 fs. This shows how carrier relaxation is strongly dependent on the choice of the optically coupled states investigated by the probe. To further investigate the dynamics in between these two probe energies it will be necessary to measure a differential transmission spectrum, which will be the topic of the next section. Figure 4.2(c) shows the dependence of the absolute value of

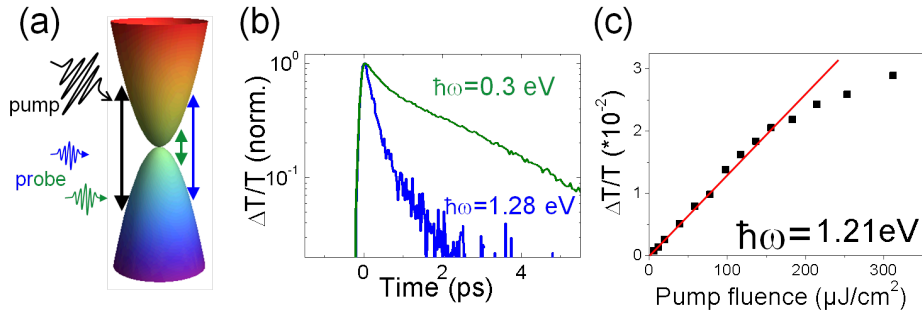


Figure 4.2.: (a) Scheme of the experiment with a sketch of the electronic band dispersion calculated for 2-layer graphene at the K -point in the first Brillouin Zone. A pump pulse (black vertical arrow) creates an excited carrier distribution. The change in the transmission of the probe pulse (vertical blue and green arrow) is monitored as a function of time delay between pump and probe. (b) Normalized differential transmission transients at probe energies of 1.28 eV (blue curve) and 0.3 eV (green curve) at a photocarrier density of $5.0 \times 10^{11} \text{ cm}^{-2}$. (c) Dependence of the absolute value of the differential transmission change on the pump pulse intensity for a fixed probe energy of 1.21 eV at $\delta t = 0$. A linear relation can be observed up to a fluence of $170 \mu \text{ J cm}^{-2}$.

$\Delta T/T$ on the pump pulse intensity for a fixed probe energy of 1.21 eV. A linear relation can be observed up to a fluence of $170 \mu \text{ J cm}^{-2}$. In this linear regime it is a good approximation to assume that many-body effects depend only on the photoexcitation density and are independent of time. Furthermore, for certain spectral regions, the change in the matrix elements for interband transitions may be small enough to be neglected[22]. The latter is an assumption for the model used to simulate the experimental data described in section 3.4 and allows us to discuss the experimental results in terms of carrier population dynamics. Unless otherwise specified all measurements are performed in the linear regime.

4.3. Spectrally resolved carrier dynamics

Ground-state absorption Before investigating excited state spectra we discuss the ground state absorption spectrum of 2-layer graphene. Figure 4.3 shows the ground-state absorption spectrum for the 2-layer graphene flake taken with a fourier-transform infrared-spectrometer (Bruker HYPERION 3000 FT-IR) in the spectral range from 0.2 eV up to 1 eV. As a guide for the eye the theoretical expected value for the absorption of two layers graphene $2\pi\alpha = 2 \cdot 2.293\%$ [17] with $\alpha = e^2/\hbar c$ is shown, indicated by the green horizontal line. Nair et al. measured

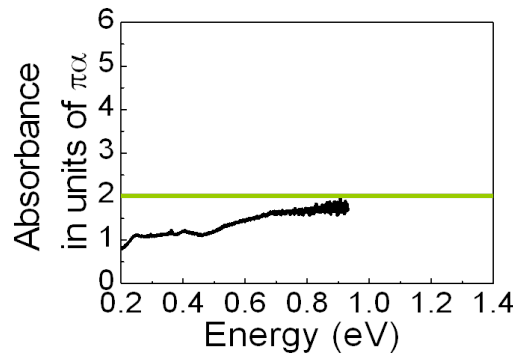


Figure 4.3.: Ground-state absorption spectrum for the 2-layer graphene flake in the spectral range from 0.2 eV up to 1 eV. As a guide for the eye the theoretical expected value for the absorption of two layers graphene $2\pi\alpha = 2 \cdot 2.293\%$ [17] with $\alpha = e^2/\hbar c$ is shown, indicated by the green horizontal line.

the absorption of a 2-layer graphene flake in the visible range of the spectrum from 400 nm to 700 nm, i.e. from 3 eV to 1.8 eV [17]. Li and co-worker measured the infrared conductivity up to 1 eV [73]. Both groups could find a qualitative agreement with the theoretically predicted value of $2\pi\alpha$. From our absorption spectrum it can be seen, that (i) no strong resonances appear in the investigated energy range and (ii) for smaller energies the deviation from the theoretical value is increasing. Mak et al. measured the same deviation for a 1-layer graphene in the same energy range. They described this behaviour to effects due to optical intraband-transitions and phenomena induced by the underlying substrate [32]. The substrate used in the measurement for the ground-state absorption spectrum is a 0.5 mm thick CaF₂ window, thus a small doping effect from the substrate cannot be excluded and may explain the absorbance drop to $\pi\alpha$ at photon ener-

gies below 0.5 eV.

Differential transmission transients of 2-layer graphene

In order to have a more complete picture of the carrier dynamics in 2-layer graphene, we recorded differential transmission spectra from pump-probe experiments. Figure 4.4 (a) and (b) show $\Delta T(\hbar\omega)/T(\hbar\omega)$ spectra for three different

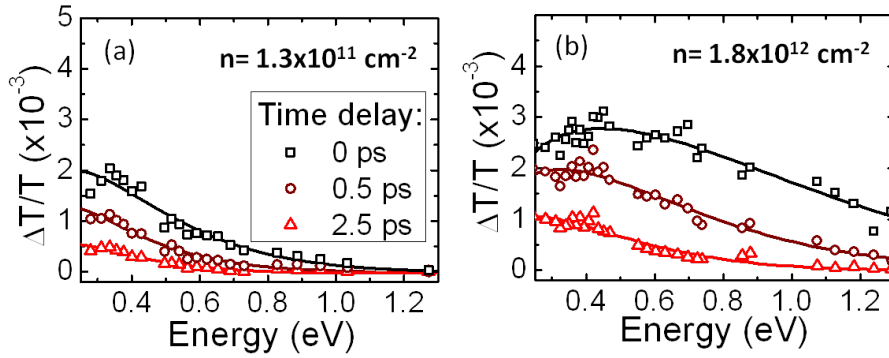


Figure 4.4.: Differential transmission spectrum of 2-layer graphene for three time delays (0 ps: black squares, 0.5 ps: brown circles and 2.5 ps: red triangles) between pump and probe for photocarrier densities of (a) $1.3 \times 10^{11} \text{ cm}^{-2}$ and (b) $1.8 \times 10^{12} \text{ cm}^{-2}$. The solid line are fits according to the model described in section 4.4.

time delays between pump and probe pulse (0 ps, 0.5 ps and 2.5 ps) and at two different initial carrier densities; (a) $1.3 \times 10^{11} \text{ cm}^{-2}$ and (b) $1.8 \times 10^{12} \text{ cm}^{-2}$. At a time delay $t=0$ a positive $\Delta T/T$ is detected across the whole energy range investigated. For both carriers densities, the signal amplitude is monotonically decreasing towards energies closer to the pump. This is clearly different from results reported in the previous optical experiments on epitaxial graphene [68, 71, 74]. In such epitaxial samples, the substrate induced doping gives rise to negative $\Delta T/T$ signals (photoinduced absorption) at the Fermi edge, which is shifted by up to 300 meV from the Dirac-point [68]. A positive $\Delta T/T$ over the whole spectral range investigated, as reported in our experiments is due to state filling of the optically coupled states and gives direct access to the relaxation of carriers. At low carrier density (Fig. 4.4(a)), the spectra recorded at 0.5 ps and 2.5 ps exhibit an almost vanishing signal on the high photon energy part, whereas between 0.25 eV and 0.5 eV the $\Delta T/T$ remains with a non-negligible amplitude, indicating

that carriers in this energy range are blocking the interband transitions with a slower decay. In agreement with the results of Fig.4.2(b) these results demonstrate that upon photoexcitation a fast cooling of the carriers at photon energies closer to the pump occurs. In Fig.4.4(b), we show the transient spectra at a higher excitation density, corresponding to $1.8 \times 10^{12} \text{cm}^{-2}$. Here, the spectra at 0.5 ps and 2.5 ps are characterized by slowly decaying dynamics extending to 1.0 eV, suggesting that also carries populating states closer to the pump have a longer lifetime. The spectra shown here will be used in the next section to determine the carrier temperature as a function of time and carrier density.

4.4. Analysis of the carrier dynamics

Carrier temperatures To extract the carrier temperatures T_c , we have fitted the $\Delta T(t, \hbar\omega)/T(\hbar\omega)$ data discussed in the last section with a model considering two Fermi-Dirac distributions for electrons and holes, characterized by a carrier temperature and two separated chemical potentials. Details of the model are described in section 2.2.1-2. Such a description with two carrier potentials has been demonstrated to be the most appropriate for the ultrafast dynamics of carriers in graphite [72] and can be extended to graphene. The transient absorption ΔA is modeled considering the difference in the excited and ground state dynamical conductivities, σ_{ex}^{tot} and σ_{gr}^{tot} and the absorption of the unexcited system A_0 .

$$\Delta A \propto -\ln(1 + \Delta T) \cong -\Delta T, \text{ for } |\Delta T| \ll 1 \quad (4.1)$$

$$\text{with } \frac{\Delta T}{T} \cong -\frac{4\pi}{c} (\sigma_{ex}^{tot} - \sigma_{gr}^{tot}) A_0 \quad (4.2)$$

where σ^{tot} is the sum of the inter- and intraband contributions:

$$\sigma^{tot}(T_c, \hbar\omega) = \sigma^{inter}(T_c, \hbar\omega) + \sigma^{intra}(T_c, \hbar\omega) \quad (4.3)$$

The intraband contribution is a Drude-like term from Ref. [32] used to account for the slight decrease in $\Delta T/T$ on the low energy side of the spectra at high carrier densities (see section 2.2.1). A_0 is the ground state absorption, which we consider constant in the probed energy range, while T_c and the chemical potential are

used as fitting parameters. The model assumes that the ultrafast carrier-carrier scattering, occurring in less than 10 fs [72], results in two Fermi-Dirac populations one for electrons and one for holes, with a common characteristic temperature T_c . This is established within the time resolution of our measurements (≈ 150 fs). The subsequent decrease in carrier population starting from the high energy tails of the spectra is due to carrier-phonon scattering and eventually recombination.

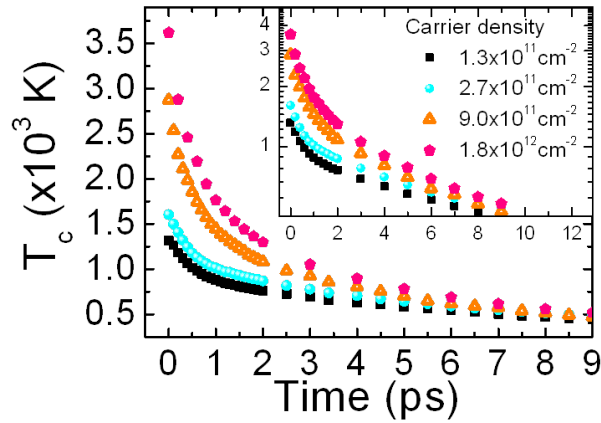


Figure 4.5.: T_c as a function of time for four different carrier densities as specified in the legend. The inset shows the same cooling curves on a logarithmic temperature scale.

The fits shown as solid lines in Fig.4.4(a) and (b) reproduce well the recorded experimental curves through the whole photon energy range investigated. Spectra such as those in Fig.4.4 were measured with four different initial carrier densities and each spectrum was fitted with the described model in order to get the carrier temperature as a function of time (*cooling curves*). The resulting cooling curves are plotted in Fig.4.5 for these four different carrier densities. All curves show an initial fast decrease consistent with the emission of optical phonons, followed by a longer tail due to coupling with acoustic phonons. The inset to Fig.4.5 shows the same graph in a log-linear plot. First, we note that the initial carrier temperature at time $\delta t=0$ increases with carrier density. Considering optical phonon emission as the main energy loss channel in the first few hundreds of femtoseconds, most of the excess energy is transferred in the phonon system. In the next section, a simple two-temperature model will be discussed to illustrate the temporal evo-

lution of the temperature for electrons and holes and used below to discuss the behaviour reported in Fig.4.5.

Two-temperature model The relaxation dynamics of carriers and optical phonons are strongly coupled, and experimental data can only be interpreted correctly if this coupling is taken into account. In the following we will present a simple model that considers this coupling to calculate the temperatures of the carrier system and the optical phonon system [74]. Intraband electron phonon scattering can be intravalley (due to Γ -point E_{2g} optical phonons, at the K-point in the Brillouin Zone) or intervalley (due to A'_1 phonons between K- and K'-points, see section 2.3.2). Using the results given by Rana et al., the net optical phonon emission rate $W_{\Gamma O}$ in units of $cm^{-2}s^{-1}$ due to intraband intervalley and intravalley electron-phonon generation and recombination given by [75]:

$$W_{\Gamma}(T_e, T_l) \approx \frac{9(dt/db)^2}{\pi\rho\omega_{\Gamma}\hbar^4v_F^4} \int_0^{\hbar\omega_{\Gamma}} dE \times E(\hbar\omega_{\Gamma} - E) \quad (4.4)$$

$$\times [f_c(E)(1 - f_c(E - \hbar\omega_{\Gamma}))(1 + n_{\Gamma}(\hbar\omega_{\Gamma})) \quad (4.5)$$

$$- f_c(\hbar\omega_{\Gamma} - E)(1 - f_c(E))n_{\Gamma}(\hbar\omega_{\Gamma})] \quad (4.6)$$

where $dt/db \approx 45$ eV/nm is the electron-phonon coupling matrix element [76], $\rho = 7.6 \times 10^{-7}$ kg/m² is the sheet density of graphene, $\hbar\omega_{\Gamma}$ and $n_{\Gamma} = (\exp(\hbar\omega_{\Gamma}/k_B T_l) - 1)^{-1}$ the phonon energy and occupation number of the E_{2g} and A'_1 phonon, the Fermi velocity $v_F = 1.1 \times 10^6$ m/s and $f_c(E)$ is the Fermi-Dirac distribution for conduction band electrons. The product $E(\hbar\omega_{\Gamma} - E)$ in the integrand originates from the initial and final density of states. W_K is calculated in a similar way, replacing $\hbar\omega_{\Gamma}$ with $\hbar\omega_K$. The frequencies of the phonons are, $\omega_{\Gamma} \cong 1580$ cm⁻¹ and $\omega_K \cong 1300$ cm⁻¹. Simulating the temperatures of the electronic system T_e and the lattice system T_l , the following set of rate equations is used [77]

$$\frac{dT_e(t)}{dt} = \frac{I(t) - W_{\Gamma,K}(T_e, T_l)}{C_e(T_e)} \quad (4.7)$$

$$\frac{dT_l(t)}{dt} = \frac{W_{\Gamma,K}(T_e, T_l)}{C_l(T_l)} - \frac{T_l(t) - T_0}{\tau_l} \quad (4.8)$$

with the specific heat of the electrons $C_e = \frac{18\zeta(3)}{\pi\hbar^2 v_F^2} k_B^3 T_e^2$ and of the phonon system $C_l = -4.79 \times 10^9 + 9.09 \times 10^6 T_l + 4456 T_l^2 + 1.29 T_l^3$, the absorbed laser intensity $I(t) = (F/2\tau_{exc}) \text{Sech}^2(t/\tau_{exc})$ with the absorbed fluence F and the duration of the exciting laser pulse $\tau_{exc} = 80$ fs. The second term in Eq.4.8 with the average phonon lifetime τ_l represents an energy loss channel for the optical phonon system due to anharmonic coupling. Figure 4.6 shows the calculated temperatures of the

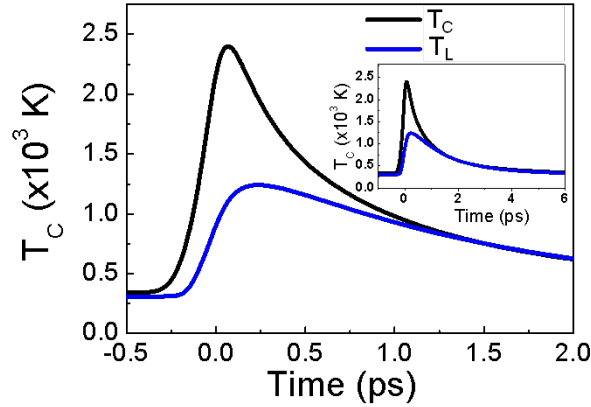


Figure 4.6.: Simulated temperatures of the electronic system (black line) and the lattice (blue line) in the first 2 ps derived from a two-temperature model described in the text. The inset shows the same temperature characteristics up to 6 ps after photoexcitation.

electronic system (black line) and the phonon system (blue line) as a function of time after photoexcitation. τ_l was assumed to be 2 ps [74], indicating the lifetime of acoustic phonons and the lattice temperature in equilibrium is $T_0 = 300$ K. What the calculations demonstrate is that within the first 500 fs the temperature of the electronic system rapidly decreases and the phonon temperature rapidly increases. This is how the excess energy from the electronic system is transferred into the lattice. With increasing carrier density, or absorbed pump fluence F , the initial temperatures of both systems increase too (not shown). As the temperature of the carriers and the phonons approach each other (at ≈ 250 fs), the net energy exchange between both systems also decreases and the temperature is slowly going back to the initial value of the lattice. At this moment in time the excited optical phonon system becomes the main bottleneck for further cooling

of the carrier system. This simple model gives a qualitative illustration of the temperature characteristics for carriers and phonons and helps in understanding the biexponential decay observed in Fig.4.5 of the last section. In particular, the first fast decay is due to transfer and thus excitation of optical phonons, the second slower component due to anharmonic coupling of optical phonons to acoustic phonons.

4.5. Influence of carrier density on energy loss

By quantifying the rate at which the electronic system is decreasing temperature we will calculate the *energy loss rate*. In the previous section the carrier temperature as a function of time has been calculated by modelling the transient spectra at different times and different initial photoexcited carrier densities. From here, it is possible to extract the energy loss rate P (or power loss) defined by:

$$P = \partial(k_B T_c) / \partial t \quad (4.9)$$

at different temperatures T_c and carrier densities. Figure 4.7 shows the logarithm of the energy loss rate versus the inverse carrier temperature $1/k_B T_c$ for four different initial carrier densities. In all graphs, P is decreasing exhibiting two clearly distinct regimes indicated by different slopes. As mentioned in section 4.4, in the initial regime, the power loss is expected to be dominated by the emission of optical phonons, while at lower T_c carriers can relax via low energy acoustic phonons [69]. The slopes of the curves in Fig.4.7 are proportional to the energy of the phonons $\hbar\Omega$ involved in P , since $P \cong \frac{\hbar\Omega}{\tau} e^{-\hbar\Omega/k_B T}$ [22]. A sum of the optical and acoustic cooling rates contributes to the overall P curve [78]. We report slopes of 350, 435, 424 and 506 meV as a function of increasing carrier density for the initial regime and ≈ 100 meV for the second. While 100 meV is in good agreement with the recent calculations on acoustic modes in graphene [67], the slopes of the initial regime are above the sum of the phonon energies and points to an additional carrier-dependent channel. Interestingly, the turning point towards the regime where cooling dynamics via acoustic phonons is dominant clearly depends on the carrier density (arrows in each graph). For higher

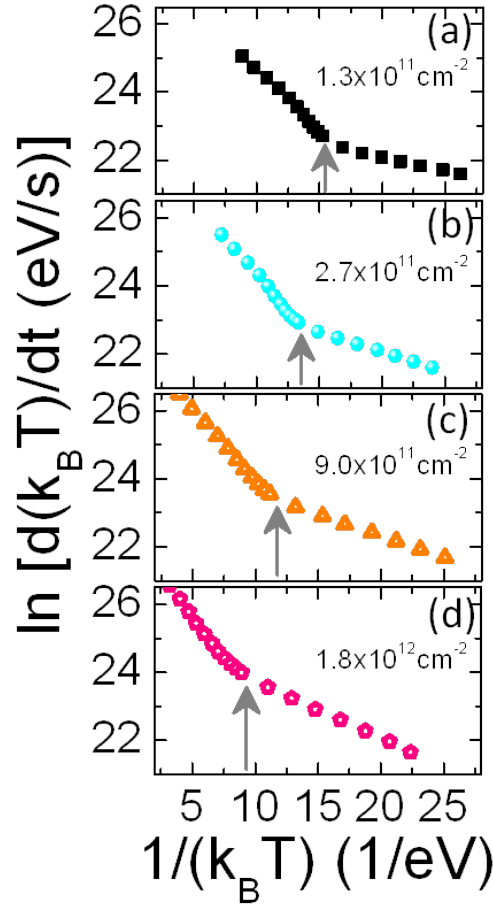


Figure 4.7.: Logarithm of the energy loss rate $\partial(k_B T_c)/\partial t$ as a function of $1/T_c$ for the carrier densities (a) $1.3 \times 10^{11} \text{ cm}^{-2}$, (b) $2.7 \times 10^{11} \text{ cm}^{-2}$, (c) $9.0 \times 10^{11} \text{ cm}^{-2}$ and (d) $1.8 \times 10^{12} \text{ cm}^{-2}$. The arrows indicate the turning point between a cooling mechanism dominated by optical phonons and acoustic phonons.

carrier densities the turning point is shifted to higher temperatures. This behavior can be explained considering that the power loss is proportional to the carrier temperature and density for both optical and acoustic cooling [69, 70]. However, optical phonons once excited transfer their energy to acoustic modes and from there to the surrounding heat bath. The transfer from optical to acoustic may not be as efficient as carrier optical-phonon transfer, leading to a large population of optical phonons and decreased cooling rate, also known in literature as *hot phonon effect* [79]. Thus, in the presence of a hot non-equilibrium phonon

population it is possible that energy is back-transferred to the electronic system, slowing down the cooling. The hot phonon effect is less apparent in the cooling via acoustic modes, since those have a lower thermal-impedance mismatch with the heat bath. Our data suggest that in the presence of the hot phonon effect, cooling via acoustic phonons takes place already at higher T_c .

4.6. Summary

In conclusion, we analyzed the energy loss channels of photoexcited carriers in 2-layer graphene and the influence of different initial photoinduced carrier densities. By modelling the recorded transients we were able to extract the carrier temperature as a function of time. From the cooling curves the power loss of the photoexcited system could be calculated, showing two different temporal regimes of carrier cooling dominated by optical and acoustic phonon emission. Due to the high optical phonon energy in graphene (about 195 meV) cooling via optical phonon emission is very efficient and within hundreds of femtoseconds a hot phonon population is established. The optical phonons decay by anharmonic coupling into acoustic phonons on a slower picosecond timescale. Here, the experimental data showed that for increasing carrier density the crossover between the two regimes occurs at higher carrier temperatures because cooling via optical phonons experiences a bottleneck. Since cooling via acoustic phonons is less sensitive to saturation effects, we could show that acoustic phonons show an increasing contribution to the energy loss at high carrier densities.

5. Carrier recombination lifetime in few-layer graphene

In this chapter, we show the possibility to determine the carrier recombination lifetime in few-layer graphene flakes by monitoring the dynamics of photoinduced intersubband transitions. The experiments are performed by femtosecond transient spectroscopy in the near to middle infrared, 0.8 eV - 0.35 eV photon energy, on isolated high quality graphene flakes and few-layer graphene flakes. At these photon energies, we are sensitive to the intersubband structure of few-layer graphene, which becomes more complex as the number of layers is increased. The differential absorption spectra show an evolving structure of photoinduced absorption bands superimposed on the bleaching due to Pauli blocking of the interband optically coupled states. Supported by tight binding model calculations of the electronic structure, we assign the photoinduced absorption features to intersubband transitions as the number of layers is increased. Interestingly, the intersubband photoinduced transitions show slower dynamics than the interband bleaching. Due to their independence from the absolute energy value of the carriers with respect to the Dirac point, the lifetime of these intersubband transitions depends exclusively on the lifetime of the photoinduced carriers. The experiments provide an elegant method to measure the carrier recombination lifetime in a class of zero gap semiconductors such as few-layer graphene.

5.1. Few-layer graphene and the problem of carrier recombination

In section 2.1 the electronic band dispersion of a single layer graphene was calculated within a tight binding model. One important aspect of this chapter is the evolution of the electronic structure as the number of layers is increased. Therefore, the tight binding model is used to calculate the energy dispersion of few-layer graphene. Fig.5.1 displays the evolution of the electronic band disper-

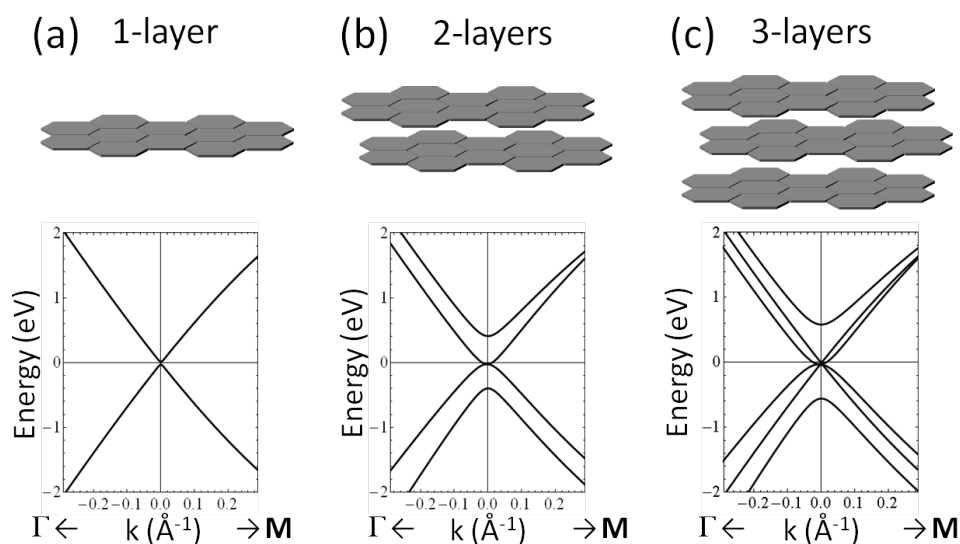


Figure 5.1.: Evolution of the electronic band dispersion with increasing number of stacked graphene layers. (a) The band dispersion of a 1-layer graphene at the high symmetry K -point in the first Brillouin Zone along the Γ - M intersection line calculated with the in section 2.1 described tight binding model. For a single-layer of graphene there are two bands which intersect at the Dirac-point. (b) The energy dispersion for an AB-stacked 2-layer graphene. The energy dispersion shows a subband structure with two bands in the conduction and two bands in the valence band. (c) The situation for three AB-stacked graphene layers with a more complex subband structure in the conduction and valence band. As a general rule, the number of subbands is equal to the number of layers.

sion with increasing number of AB-stacked graphene layers. Fig.5.1(a) shows the band dispersion of a 1-layer graphene at the high symmetry K -point in the first Brillouin Zone along the Γ - M intersection line calculated with the tight binding model described in section 2.1. For a single-layer of graphene there are two

bands which touch at the Dirac-point and about ± 1 eV to this point the energy dispersion is approximately linear. A variety of very interesting phenomena result from this special band dispersion as compared to the parabolic one of most semiconductors. For example, quasi-ballistic transport, room-temperature quantum Hall effect and the quantum of conductance [17, 80, 81]. For a three dimensional calculation of the energy dispersion in 1-layer graphene, see Fig.2.4 in chapter 2. Fig.5.1(b) shows the energy dispersion for an AB-stacked system of 2-layer graphene. The energy dispersion shows a subband structure with two subbands in the conduction and two subbands in the valence band. Therefore, 2-layer graphene exhibits a subband-structure in both the conduction and valence band. Fig. 5.1(c) displays the situation for three AB-stacked graphene layers with an even more complex subband structure in the conduction and valence band. As a general rule, the number of subbands is equal to the number of layers. Stacking additional layers on top is thus an easy parameter to change the electronic band structure investigated. For three layers, the minimum of the highest conduction band and the maximum of the lowest valence band have an energetic distance of ≈ 0.8 eV to the Dirac point. So infrared pump-probe can access this energy range. Carrier recombination in graphene and few-layer graphene is of relevance for many different applications in optoelectronics. For example, the total intrinsic response time τ_r of photodiodes is given by $\tau_r^{-1} = \tau_{rec}^{-1} + \tau_t^{-1}$ [82], with the carrier recombination time τ_{rec} and the transit time τ_t . Generally, in photodetectors either τ_{rec} or τ_t must be short for high-speed operation. For instance, in metal-semiconductor-metal photodetectors based on GaAs materials, high-speed operation can be achieved either by reduction of τ_{rec} with low-temperature-grown GaAs containing many defects [83], or by reduction of τ_t by keeping the distance between the electrodes short [84].

So far, measurements on carrier lifetime in graphene and graphite have been performed by looking at interband transitions [71], terahertz absorption [85] and time resolved photocurrent [82, 86]. Measurements on the interband conductivity probed the time evolution of carriers at specific energies in the band and were, therefore, not able to directly measure the time scales associated with carrier recombination. Urich et al. used a time resolved photocurrent technique to conclude on the carrier recombination time by determining the photodetector

response time. The RC-limited bandwidth of graphene-based photodetectors is approximately 640 GHz [87]. Therefore, common electronic techniques cannot resolve the ultrafast charge carrier dynamics due to challenges in producing electronic trigger signals and detecting transients in the picosecond regime. In the following chapter, we will investigate the dynamics of carriers resulting from the layer-dependent band structure in few-layer graphene.

5.2. Samples and experimental settings

Single and few-layer graphene flakes, with the typical AB-stacking sequence, were prepared by mechanical exfoliation of natural graphite and deposited on SiO₂ substrates according to section 3.1.1. Single and few-layer homogeneous graphene flakes were then transferred to quartz to perform optical experiments on a transparent substrate by means of the method described in detail in section 3.1.3. Images taken with an optical microscope in transmission and reflection of all few-layer graphene samples investigated in this section with the corresponding Raman scattering spectrum are shown in Fig.5.2(a)-(g). The figure shows samples with $N_L=1,2,3,4,5,10$ and 15 layers and a zoom of the characteristic 2D resonance in the Raman spectrum. The latter one being sensitive to the number of layers as explained in chapter A. Due to the low absorption of graphene in the visible spectrum, the images of the different graphene layers on transparent substrates have a very low contrast with respect to the background. Just for demonstration the 5-layer sample is shown on the initial Si/SiO₂ substrate before the transfer to quartz. Here, the contrast is improved due to interference effects with the underlying SiO₂ [58]. Even after transfer the graphene layers did not show evidence of a D-band [49] in the Raman spectrum, testifying that the high quality of the flakes. 1-layer graphene (Fig.5.2(a)) shows a characteristic single-lorentzian shape of the 2D peak, for 2-layer graphene on the other hand the peak position is blue shifted and the shape is broader with a distinctive shoulder on the low wavenumber side. This allows a distinction between 1- and 2-layer graphene [64]. In chapter A we describe a method to determine the number of graphene layers between $N_L=4-10$ by analyzing the Raman spectrum, in particular the 2D

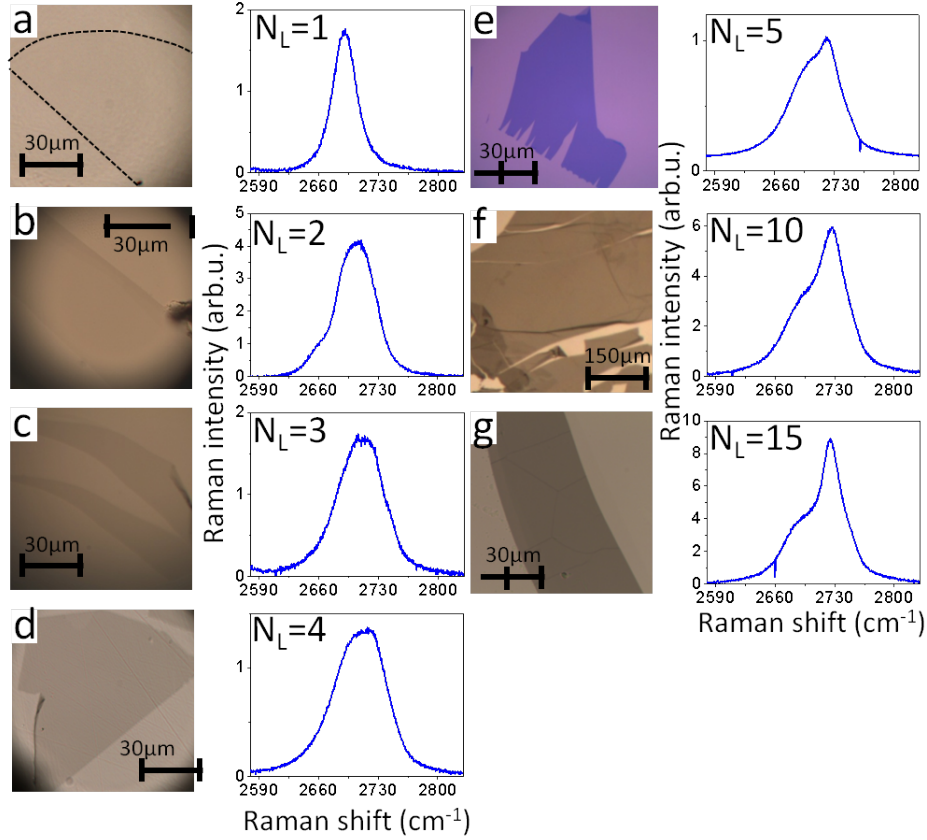


Figure 5.2.: Optical microscopy images and Raman scattering spectra of all few-layer graphene samples investigated in this chapter. (a)-(d),(f) and (g) show optical microscope images in transmission with the corresponding Raman scattering spectrum of the 2D resonance, N_L gives the number of layers. Due to the small contrast with respect to the background the few-layer graphene samples appear only as a slightly darker region in the image, additionally for the 1-layer a dashed line has been added to help in identifying the flake. (e) shows an optical image in reflection of the 5-layer sample on a Si/SiO₂ wafer prior to transfer to a transparent substrate. The 2D-peak is used to determine the number of layers together with atomic force microscopy. A detailed description of the evolution of the 2D-peak in the Raman spectra is given in section A.

peak. Carriers were photoexcited with 70 fs pulses at 1.55 eV from an amplified Ti:sapphire laser. Probe pulses with similar time durations were obtained from an optical parametric amplifier (see section 3.2 for details). The signal and idler from the OPA were used as probe beams. Experiments were performed by focusing the pump and probe beams on a single flake in ambient conditions

and detecting the normalized change in absorption $\Delta a(t, \hbar\omega)/a(\hbar\omega)$ at different probe photon energies, $\hbar\omega$, and time delays between the pump and the probe, t . Experiments were conducted in a linear regime between pump fluence and $\Delta a/a$ signal with a pump fluence of $5 \mu\text{Jcm}^{-2}$ and photoinduced carrier densities of $\approx 4 \times 10^{10} \text{ cm}^{-2}$.

5.3. Differential absorption transients of few-layer graphene flakes

Differential absorption spectra Figure 5.3(a-e) shows the differential absorption $\Delta a/a$ spectra in the probe photon energy range from 0.35eV-0.8 eV at three different pump-probe delay times, 0 ps (black squares), 0.5 ps (blue circles) and 4 ps (red triangles) for $N_L = 1$ -, 2-, 3-, 4- and 5-layer graphene, respectively. Here a positive value, $\Delta a/a > 0$, indicates photoinduced absorption and a negative value, $\Delta a/a < 0$ photoinduced bleaching. Whereas 1-layer graphene exhibits a featureless photoinduced bleaching over the whole probe photon energy range investigated, the few-layer graphene samples starting from 2-layers are characterized by photoinduced absorption bands with $\Delta a/a > 0$. Even when the absorption bands are superimposed to the bleaching, they can be clearly distinguished. For example, 2-layer graphene shows a resonance centered at 0.44 eV, 3-layer a clear band at 0.66 eV and a second one at 0.48 eV. For 5-layer two clear absorption bands at 0.45 eV and at around 0.7 eV. In general, we observe a richer spectrum with absorption bands appearing broader as the number of layers increases. Another important characteristic of these data lies in the time domain. By looking at the time evolution, it is possible to recognize a longer lifetime of the absorption features with respect to the bleaching signals. To further analyze the recorded spectra we have first calculated the absorption spectra of graphene with increasing number of AB-stacked layers.

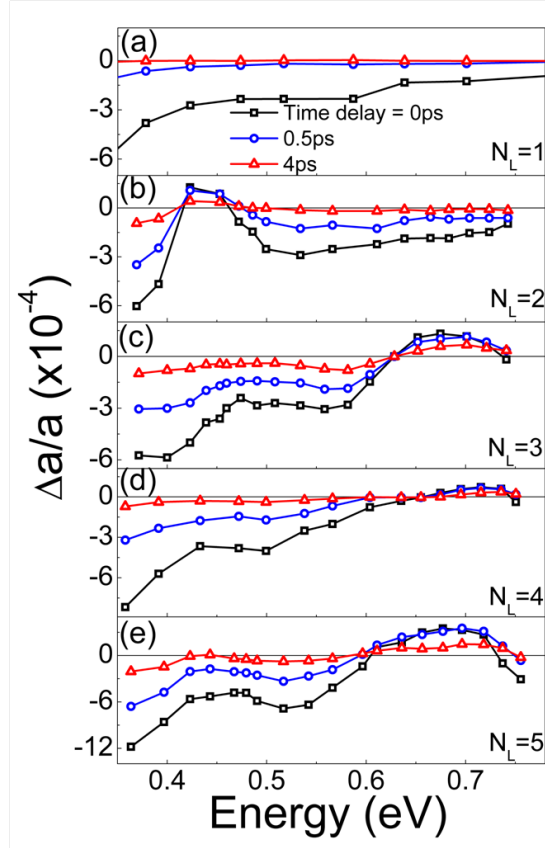


Figure 5.3.: Differential absorption transients in the probe energy range from 0.35 eV-0.8 eV with $N_L = 1, 2, 3, 4, 5$ number of graphene layers for three different time delays between pump and probe. Black squares 0 ps, blue circles 0.5 ps and red triangles 4 ps. The single-layer (a) sample exhibits a featureless bleaching over the whole energy range investigated. Two-layer graphene (b) shows one absorption band at 0.42 eV superimposed to the bleaching signal. Three- (c) and four- (d) layer show one absorption band at energies 0.65 eV and 0.7 eV respectively. For the case of five-layers two broad absorption bands are clearly visible at energies of 0.45 eV and 0.68 eV.

Calculation of the absorption spectrum We first attempt to describe the nature of the absorption features appearing in the few-layer graphene spectra. A tight binding model described in detail in section 2.1 is used to describe the electronic structure of graphene and few-layer graphene. This allows us to have an accurate estimation of how the band structure of graphene evolves as the number of layers is increased. Using the tight binding wavefunctions we calculate the matrix elements according to equation 2.37 for all possible transitions be-

tween (i) the subbands of the conduction and valence band and (ii) those across the conduction and valence band. In a first approximation, we try to compare the calculated spectra with the experimental data by subtracting the absorption spectrum at an elevated carrier temperature T_C with the absorption spectrum at room temperature T_0 . Possible doping effects for exfoliated few-layer graphene samples on quartz substrates can be neglected [88]. In such conditions, the Fermi level before the photoexcitation by the pump pulse is assumed to be close to the Dirac point. The temperature value for the excited spectrum was taken from Ref. [89]. The simulated Δa spectra in figure 5.4(a-e) are obtained by calculating the absorption spectra of graphene flakes given by equation 2.34 at elevated T_C , a_{Exc} , and subtracting the absorption at room temperature T_0 , a_{RT} .

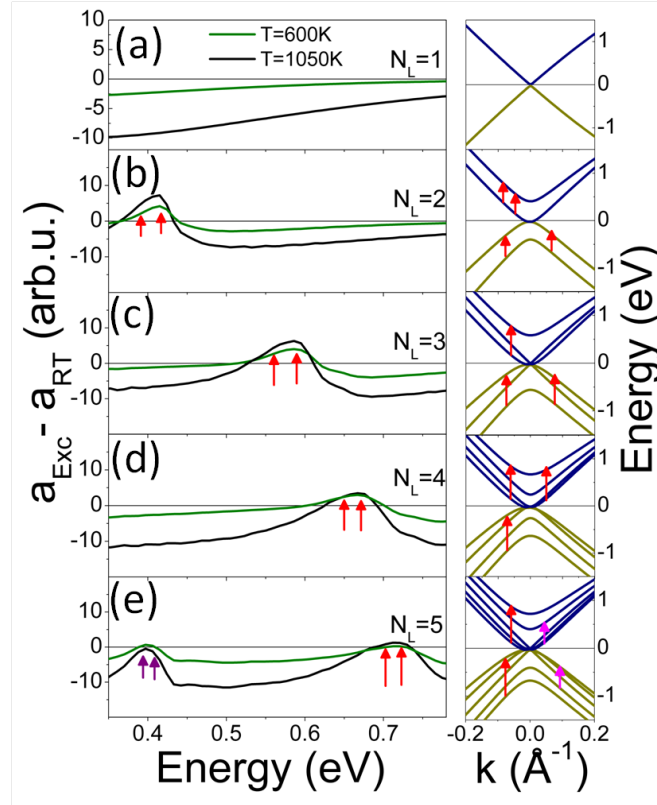


Figure 5.4.: Calculated absorption spectrum for $N_L = 1, 2, 3, 4, 5$ number of graphene layers with the corresponding band dispersion to the right of each spectrum. The spectra are calculated by taking the absorption spectrum at an elevated temperature ($T_C = 1050$ K, black and $T_C = 600$ K, green) and subtracting the one at room temperature T_0 .

Fig.5.4 shows the calculated spectrum for $N_L = 1, 2, 3, 4, 5$ number of graphene layers together with the corresponding band dispersion on the right hand column. The black curves represent spectra at $T_C = 1050$ K, the green curves at $T_C = 600$ K, which describe the dynamics of the absorption transients. In performing these calculations we assume an initial ultrafast scattering of electrons and holes into the bottom conduction subband and top valence subband, respectively. The spectra show a remarkable agreement with the measured $\Delta a/a$ in terms of correspondence with the absorption resonances. We note appreciable deviations from the experiments on the low energy side of the spectra, below 0.4 eV. This might be due to dynamics of the system after photoexcitation not considered in the model. For example, due to the strong electron optical-phonon coupling described in section 3 and the short timescale relevant for this process, optically coupled states energetically closer to the pump energy will be depopulated much faster than those states closer to the Dirac point. An increase in the absolute value of the photobleaching with decreasing probe energy is one consequence as seen in the recorded data.

A first indication that photoinduced absorption resonances originate from intersubband transitions comes from their absence in single-layer graphene. The nature of the intersubband absorption transitions is indicated with red vertical arrows in the respective energy dispersion graphs. The 2-layer sample shows absorption from the bottom subband to the top one, both in the conduction and valence band. If the number of layers increases, new subbands are present and additional transitions contribute to the absorption resonances. Clearly, absorption features are broadened by the differences in the energy separation of the subbands in the conduction and valence band and because of the increasing energy difference of the transitions for carriers which have relaxed closer to the Dirac point. It is also important to notice that our simulated spectra reproduce the bleaching spectral regions in which hot carriers occupying the bottom conduction (electrons) and top valence band (holes) induce Pauli blocking. This gives us confidence that our initial assumption of a fast intersubband scattering to the bottom (top) subband for electrons (holes), is valid and reflects the effective experimental dynamics. The calculated spectrum of the 5-layer graphene sample gives two possible transitions in the conduction and valence band at around

0.41 eV and 0.7 eV with the latter exhibiting a more broad peak. Both features can be clearly resolved in the experimental data, Fig.5.3(e). Therefore, by calculating a room temperature corrected, excited absorption spectrum for few-layer graphene we were able to explain the absorption bands in the recorded experimental data. Supported by theoretical calculations, we assigned the absorption bands to intersubband transitions in few-layer graphene which are absent in the 1-layer case. In the following we will investigate the temporal dynamics of the absorption bands in detail.

5.4. Carrier recombination lifetime

We turn now to the dynamics of the different spectral features. Figure 5.5(a) shows the $\Delta a/a$ transients as a function of time delay for the 2-layer sample for a probe energy of 0.42 eV (green squares) corresponding to the photoinduced absorption resonance and 0.66 eV (blue circles) which tracks the bleaching at this arbitrary chosen energy. Both dynamics show a resolution limited rise in photoinduced bleaching and absorption, respectively. After $t = 0$ ps both signals recover to $\Delta a/a = 0$, but with different dynamics. While the bleaching has a bi-exponential decay with a first ultrafast resolution-limited decay of 200 fs and a second component of 2.8 ps, the absorption shows a monoexponential decay of 5 ps. In general, all the distinguishable absorption features of Fig.5.3 show a monoexponential decay, which is a factor of two longer than the second component of the bleaching regardless of the probe photon energy. In Fig.5.5(b) we show the calculated absorption from the last section for 2-layer graphene at different carrier temperatures T_c for the same energies as in panel (a). Despite slight deviations due to the rather simple way to consider the dynamics by changing the carrier temperatures a slower decay of the $\Delta a/a > 0$ signal amplitude can be observed, in agreement with the experimental data.

In the following we will discuss the different time constants and the relevant physical mechanism responsible, starting from 2-layer graphene. We can interpret the observed behavior according to the schemes in Fig.5.5(c,d). Fig.5.5(c) shows the band structure of 2-layer graphene with photogenerated electrons and

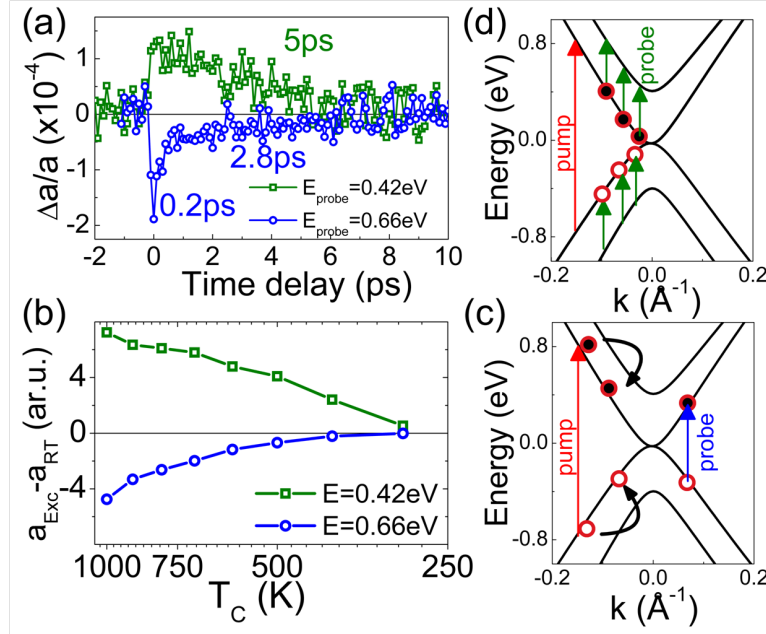


Figure 5.5.: (a) $\Delta a/a$ transients for the 2-layer sample for a probe energy of 0.42 eV (green squares) corresponding to the photoinduced absorption resonance and 0.66 eV (blue circles). (b) Calculated absorption at an energy of 0.42 eV (green squares) and 0.66 eV (blue circles) as a function of carrier temperature T_c . Energy band dispersion of 2-layer graphene with photogenerated electrons and holes with a scheme explaining the photoinduced absorption (d) and the bleached interband transitions (c). A detailed description of the processes is given in the text.

holes. At negative time delays there are no carriers at the energy of the probe photons, the transient absorption is zero. Immediately after photoexcitation, the carriers thermalize, occupying states and a decrease in the differential absorption can be observed as a consequence of Pauli blocking. The hot carriers relax in the respective bands by emission of initial optical phonons (ultrafast 200 fs component) and acoustic phonons (second slower component), until they reach a thermal equilibrium with the lattice (black curved arrows). These dynamics have been discussed in detail in chapter 3 of this thesis. The lifetime monitoring the blocked interband transitions corresponds to the rate at which the tail of the two Fermi-Dirac distributions, one for electrons and the other for holes, are depopulating those optically selected states. This means that bleaching signals monitor carrier distributions subject to several physical processes such as relaxation by phonon or plasmon emission, Coulomb scattering and eventually direct interband

recombination [75, 90, 91]. It is, thus, difficult to extract reliable information on the carrier lifetime, since a number of processes not necessarily connected to the annihilation of carriers is contributing to the recorded decay. On the other hand, Fig.5.5(d) sketches the intersubband transitions for electrons and holes superimposed on the electronic structure of 2-layer graphene. It is interesting to note how the presence of intersubband absorption transition is independent from the energy position of the carriers with respect to the Dirac point, which for undoped flakes represents the equilibrium point. This is a direct consequence of the peculiar band structure of few-layer graphene. The subbands in the conduction and valence band show an almost parallel dispersion in close vicinity to the Dirac point. If the probe energy matches the energetic difference of two subbands, carriers can be excited almost independently from the k -vector within these two subbands. Of course, provided that the optical matrix elements allow these transitions. In other words, the decay of the intersubband photoinduced absorptions is only sensitive to recombination processes which bring the carrier distribution to the room temperature equilibrium distribution. In contrast to previous studies [71], we assign the carrier lifetime in few-layer graphene to the decay of the intersubband transitions and propose this as a method to investigate the different recombination processes which have thus far been proposed on the basis of theoretical models [75, 90, 91] and not yet investigated experimentally.

All measurements discussed so far have been performed for different number of stacked graphene layer samples, namely $N_L = 1, 2, 3, 4, 5$ number of layers. As already mentioned, the dynamics of the absorption bands in the transients show a factor of two slower decay than the photobleached interband transitions. In order to compare the different layers, we fitted the monoexponential decays, $\Delta a(t)/a \propto e^{-t/\tau}$ for $t > 0$ ps with τ being the time constant of the decay.

Figure 5.6 shows the carrier lifetimes extracted from the monoexponential decays of the intersubband transitions for single flakes differing in the number of stacked layers. The large error for samples with a small number of layers is due to the small differential absorption change in the pump-probe experiments for these samples which is on the same order than the inherent noise. Within our uncertainties we observe a values ranging from 3 ps to 6 ps for the recombination lifetime as a function of the layer number. This is also valid for thicker sam-

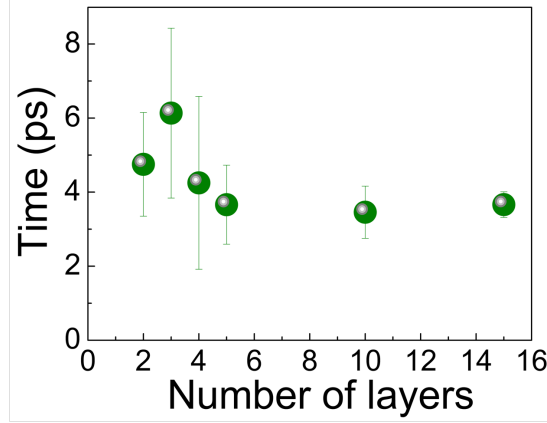


Figure 5.6.: Carrier recombination lifetimes extracted from the monoexponential decays of the photoinduced absorption transients connected to intersubband transitions for single flakes differing in the number of stacked layers.

ples made of 10 and 15 layers which should be representative for graphite [14]. For these samples due to the large number of subbands a large number of possible intersubband transitions contribute to the observed photoinduced absorption. Therefore, only a broad absorption peak with $\Delta a/a > 0$ ranging from 0.55 eV to 0.8 eV for the 10-layer and from 0.48 eV to 0.8 eV for the 15-layer at a time delay of $t=0$ ps is observed at a pump pulse fluence of $5 \mu\text{Jcm}^{-2}$ in the transients. By increasing the pump pulse fluence the contribution due to photobleaching overcomes the photoinduced absorption. For fluences $> 100 \mu\text{Jcm}^{-2}$ the differential transients show photoinduced bleaching of optically coupled states in the probe photon energy of 0.25 eV up to 1.3 eV. The response of graphite at higher fluences will be discussed in the next chapter.

Due to the absence of subbands in single layer graphene, the method proposed here to obtain the carrier recombination lifetime cannot be applied to this material system and compared to the values observed in few-layer graphenes. Therefore, other experiments, for example based on transient photoconductivity have to be optimized in order to extract values for graphene.

5.5. Summary

To summarize, in this chapter we report a method to determine the carrier recombination lifetime in few-layer graphene flakes by monitoring the dynamics of photoinduced intersubband transitions. At photon energies in the midinfrared region, we are sensitive to the intersubband structure of few-layer graphene, which becomes more complex as the number of layers is increased. With the support of tight-binding model calculations of the electronic structure we could assign the photoinduced absorption features in the differential absorption spectra to intersubband transitions. The lifetime of these intersubband transitions depends on the lifetime of the photoinduced carriers and provide an elegant method to measure the carrier recombination lifetime in a class of semimetals such as few-layer graphene.

6. Ultrafast optically induced compression of graphite lattice

In this chapter, we report direct temporal observation of ultrafast compression and expansion of the c-axis graphite lattice induced by intense femtosecond laser pulses. The experiments are performed by femtosecond transient spectroscopy in the near to middle infrared, 0.3 eV to 0.6 eV photon energy, on isolated high quality graphite flakes. In this spectral region the transients of graphite show a photoinduced bleaching of optically coupled states at all time delays between pump and probe, provided that the fluence is below 0.5 mJcm^{-2} . By increasing the pump fluence, an intense photoinduced absorption appears in the first hundreds of femtoseconds followed by an increase in transmission indicating photo-bleaching with a superimposed oscillation of the signal amplitude. The ultrashort increase in absorption is attributed to an initial compression in the c-axis of the graphite lattice induced by photo-excited coherent phonons leading to a structural modification of the interlayer spacing along the c-axis. After compression, the c-axis is expanding and the transients are accompanied by coherent oscillations with the frequency of the interlayer (E_{2g}) shearing mode showing the dynamics typical of a damped oscillator.

6.1. Graphite subjected to high fluence laser pulses

The unique semimetal graphite shows a variety of interesting structural and electronic properties. A great deal of information has been obtained by a set of experiments based on ultrafast electron scattering techniques [92–95], revealing the tendency of the c-axis of graphite to be destabilized by the photoinduced coherent motion of ions. Recently, the transition of graphite to diamond was observed by very intense femtosecond laser pulses [96]. Femtosecond transient absorption spectroscopy is a powerful tool to gain information about the coupling between carriers and the lattice [19, 97]. The excitation of coherent phonons in graphite was demonstrated with the selective coupling of excited carriers to certain atomic motions [98–100]. More than ten years ago, several optical studies have focused on the carrier dynamics at both high, above 100 mJcm^{-1} [101, 102] and low fluence, below 0.5 mJcm^{-1} [98] of the optical pump excitation. With the help of time-dependent ab-initio calculations, three different regimes for the response of graphite to high fluence pulses have been identified. The pre-ablation regime, the ablation regime and for sufficiently large fluences, breaking of the in-plane bonds is predicted [103, 104]. At fluences above the damage threshold, melting of the graphite was observed [102]. Here, we report on femtosecond transient absorption spectroscopy of graphite in the preablation regime, so below the damage threshold, and at photon energies close to the Dirac point. In this regime a coherent motion of the graphite layers is expected leading to a compression of the lattice along the c-axis direction. Interestingly, several studies predict changes in the absorption properties of graphite when the lattice is modified for example by applying pressure [105] or by irradiation with fs-pulses of moderate intensity [103, 106]. We will show here that the optical properties of graphite in the middle-infrared region are strongly dependent on the interlayer distance.

6.2. Fluence dependent photoinduced absorption in graphite

Single and multi-layer isolated graphite flakes were prepared by mechanical exfoliation as described in chapter 2. For optical spectroscopy, the samples were transferred to transparent quartz-windows. In chapter 4 and 5 of this work, different graphene flakes were investigated at pump pulse fluences below $100 \mu J cm^{-2}$. Here, we focus on the dynamics close to the Dirac point and at pump pulse fluences $>100 \mu J cm^{-2}$. Fig.6.1 shows the differential transmission dynamics for

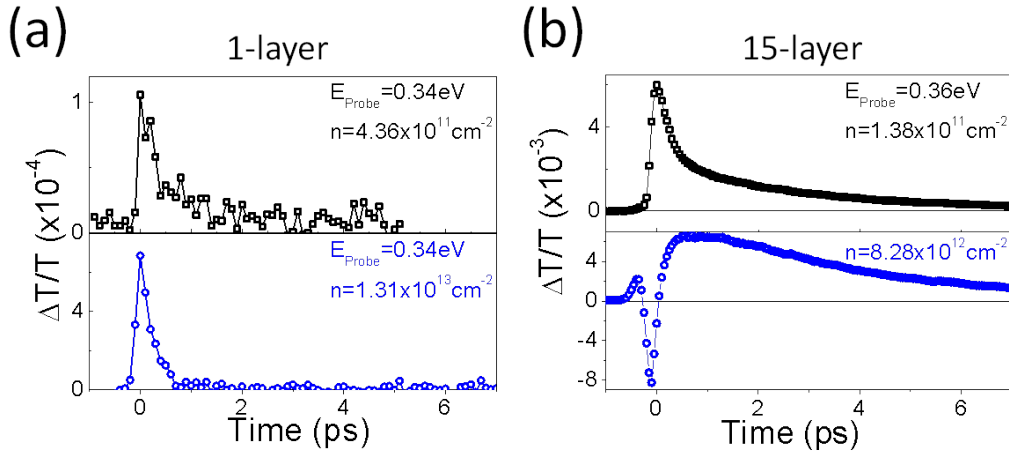


Figure 6.1.: Differential transmission dynamics for 1-layer graphene (a) and 15-layer graphene (b) at a fixed probe photon energy and for two different pump fluence values. The carrier density given in the plots is the calculated carrier density per layer for a given fluence.

1-layer graphene (a) and 15-layer graphene (b), the latter representative for graphite, at a fixed probe photon energy and for two different pump fluence values. The carrier densities displayed in the figures are calculated per layer for a given pump laser fluence. For the 1-layer graphene sample, we observe both at low fluence (top graph, black squares) and high fluence (lower graph, blue circles) a rise of the signal within our experimental limited resolution of 100-200 fs and a subsequently fast decay of the photobleaching within about 200 fs. The position of the maximum transmission change is set as $t=0$ ps. For the graphite sample, we

see at a low pump fluence ((b) black squares) similar characteristics: a resolution limited rise up to maximum transmission change followed by a decay where two temporal regimes can be observed. The physical interpretation of these two time constants was discussed in detail in chapter 2 and 3 of this work. If the pump fluence is increased to 0.7 mJcm^{-2} ((b) blue circles) we can observe a completely different behaviour in the recorded dynamics. After a short initial positive rise with $\Delta T/T > 0$, the signal has a 400 fs temporal windows with $\Delta T/T < 0$, followed by an again positive photobleached signal. Additionally, the decay of the photobleached signal is slowed down in the high fluence case. All displayed transients in Fig.6.1 were measured at a probe photon energy of about 0.35 eV. It is well known, that by means of degenerate pump-probe experiments at 1.55 eV only photobleaching is observed for pump fluences up to $0.47 \mu\text{Jcm}^{-2}$ in graphite [98]. Liu et al. report on pump fluence dependent photoinduced absorption in mixed sp^2 - and sp^3 -hybridized domains in graphene oxide [107]. There, the observed photoinduced absorption was assigned to a two-photon absorption process from the sp^3 -hybridized domains. Jeschke et al. [104] reported on time-dependent absorption changes during ultrafast lattice deformation in graphite by means of molecular dynamics simulation. At fluences close to the damage threshold, they could show that a time dependent increase of the density of states (DOS) close to the Fermi level is caused by structural changes induced by the laser pulse. Hence, the absorption spectrum of graphite irradiated with high intensity femtosecond pulses is changing dynamically by the action of the pulse. Additionally, a close correlation of the absorption characteristics to the temporal profile of the laser pulse was shown. So far, no optical experiment has been performed investigating the spectral region close to the Dirac point and at carrier densities high enough to induce some structural modifications of the graphite carbon lattice. In order to gain more information on this interesting effect, we report in the next section the dependence of the observed photoinduced absorption on the probe photon energy, the induced carrier density and the temporal duration of the pump pulse.

6.3. Influence of probe photon energy, carrier density and pulse duration on the transient absorption

Spectrally resolved carrier dynamics In order to further investigate the nature of the induced absorption in the transient dynamics we recorded the differential transmission spectrum in the probe photon energy range 0.65 eV - 0.3 eV (1900 nm - 4100 nm). Fig.6.2(a) shows the spectrum at a photoinduced carrier density of $n = 2.8 \times 10^{11} \text{ cm}^{-2}$ (black squares) and $n = 6.7 \times 10^{12} \text{ cm}^{-2}$ (blue circles) at a time delay of $t=0$ ps between pump and probe pulses. The low flu-

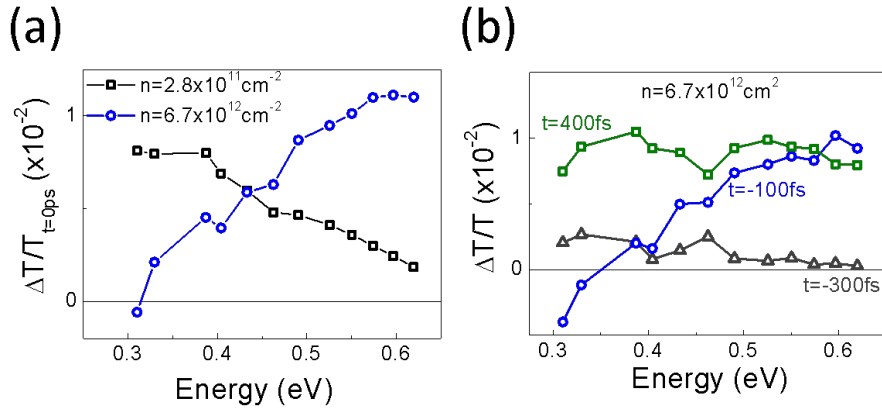


Figure 6.2.: (a) Differential transmission spectra at a fixed time delay of $t=0$ ps between pump and probe pulse and at a photoinduced carrier density of $n = 2.8 \times 10^{11} \text{ cm}^{-2}$ (black squares) and $n = 6.7 \times 10^{12} \text{ cm}^{-2}$ (blue circles). (b) Differential spectrum at three different time delays between pump and probe, $t=-100$ fs (blue circles), which is the position of the maximum absorption, at $t=-300$ fs (black triangles) and at $t=400$ fs (green squares). The temporal window of the absorption is roughly given by ± 250 fs around $t=-100$ fs in the dynamics, almost independent from the probe energy.

ence spectrum shows the characteristic behaviour of few-layer graphene already discussed in chapter 4 of this thesis. The absolute value of the photobleached signal at this time delay is increasing with decreasing energy. Optically coupled states closer to the pump photon energy will initially be faster depopulated than states closer to the Dirac point. At energies below 0.3 eV (not displayed), the

absolute transmission change decreases, probably due to Drude like absorption, which is the dominant contribution to the optical absorption at small frequencies as indicated by Eq. 1.18 and 1.19 (see section 2.2.1). On the other hand, the higher fluence spectrum (blue circles) clearly behaves differently. The absolute value of the transmission change is decreasing with decreasing probe photon energy. The fraction of photoinduced absorption overcomes the contribution due to bleaching by state blocking and, at probe energies below 0.28 eV, the differential transmission spectrum even turns negative.

Due to the small temporal window of the photoinduced absorption, it is interesting to examine whether there is a dependence of the temporal characteristics on the probe energy. Fig. 6.2 (b) shows the differential spectrum at three different time delays between pump and probe, at $t=-100$ fs (blue circles), which is the position of the maximum absorption, at $t=-300$ fs (black triangles) and at $t=400$ fs (green squares). The spectra before and after the time at which we observe the maximum photoinduced absorption are similar and show little energy dependence. At $t=-100$ fs we see the energy dependence as in Fig.6.2 (a) with an increasing contribution of the photoinduced absorption to the overall recorded signal with decreasing probe energy. The temporal window of the photoinduced absorption is roughly given by ± 250 fs around $t=-100$ fs in the dynamics and is observed below 0.35 eV probe photon energy.

Effects of carrier density on the spectrum In the last section, we discussed the differential transmission spectrum at a high and low photoinduced carrier density. The intensity of the pump pulse correlating with the photoexcited carrier density is a major factor of ultrafast carrier dynamics in graphene and related systems [89]. In the following, we will look in detail on the effects of the pump pulse fluence on the differential transients. Fig.6.3 shows the dependence of the absolute value of the recorded differential transmission signal on the photoexcited carrier density at a fixed time delay of $t=-100$ fs and for three different probe photon energies, 0.30 eV (red circles), 0.33 eV (blue circles) and 0.39 eV (black circles). At carrier densities up to $n = 5.0 \times 10^{11} \text{ cm}^{-2}$ a linear increase of the photobleached signal with the carrier density can be observed followed by a saturation for higher carrier densities. Above a value of $n = 1.0 \times 10^{12} \text{ cm}^{-2}$ the

6.3. Influence of probe photon energy, carrier density and pulse duration on the transient absorption

signal value starts to decrease, demonstrating an increasing contribution of the photoinduced absorption. Additionally, the critical carrier density at which the differential signal turns negative is shifted to lower values for decreasing probe photon energy. Combining the findings of the last two sections, we see that the

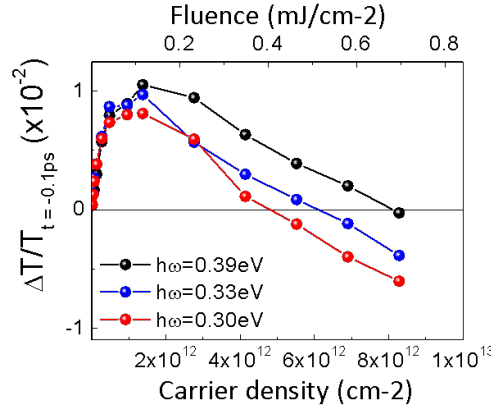


Figure 6.3.: Dependence of the absolute value of the differential transmission signal on the photoexcited carrier density at a fixed time delay of $t=-100$ fs and for three different probe photon energies, 0.30 eV (red circles), 0.33 eV (blue circles) and 0.39 eV (black circles).

energy at which the spectrum turns negative is shifted to lower energies for increasing fluence. The temporal position of the photoinduced absorption, on the other hand, is always at $t=-100$ fs. These findings suggest that the temporal position after photoexcitation does not depend on the probed electronic levels but may be correlated with the temporal intensity maximum of the excitation pump pulse.

Effect of the pump pulse temporal profile Molecular dynamics calculation based on a tight-binding model of the Hamiltonian predict ablation of graphite layers at a fluence above 160 mJcm^{-2} and a non-equilibrium melting followed by fast evaporation at fluences above 280 mJcm^{-2} [103]. All values are calculated for a pulse length of 20 fs and a photon energy of 3.0 eV (413 nm). Optical femtosecond transient spectroscopy show that melting of the graphite lattice in this experimental configuration occurs at a fluence of 130 mJcm^{-2} [102] for 620 nm, 90 fs pulses and of 250 mJcm^{-2} [108] for 825 nm, 120 fs pulses. Therefore, these

experiments suggest that broadening the pulse time width reduces the threshold for the ablation process. In Fig.6.4, the influence of the pump pulse duration on the maximum transmission change is shown. By chirping the fundamental of the amplifier system 800 nm, 50 fs pump pulse with SF10 and SF57 windows of different thickness, the pulse length is changed to 60 fs, 93 fs and 120 fs depending on the optical path length of the fundamental in the windows. A decreasing value of $\Delta T/T$ can be observed for shorter pulses, as was predicted by the calculations in [104]. Therefore the temporal profile of the excitation pulse correlates with the observed increase in photoinduced absorption. In the beginning of this chapter,

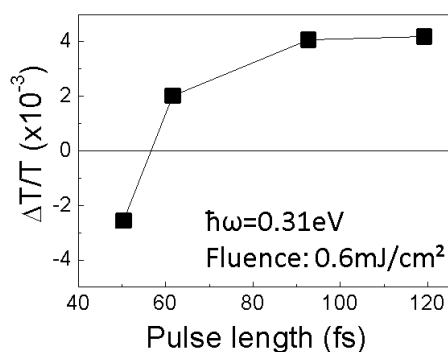


Figure 6.4.: Dependence of the absolute value of the differential transmission signal on the temporal length of the pump pulse. By chirping the 800 nm pump pulse with SF10 and SF57 windows the pulse length was changed.

we mentioned the different regimes of the response of graphite to intense laser pulses. At very high fluences, structural modifications of the graphite lattice are expected, leading to ablation of single layers and even melting of the material. In the following, we will discuss possible changes of the lattice induced by laser pulses with the help of Raman scattering spectra.

Preablation effects on the lattice We now turn the discussion to the effects on the graphite lattice due to the mechanical stress caused by fs-pulses. Fig.6.5(a) shows an optical microscope image in reflection of the graphite sample investigated deposited on a Si/SiO₂ substrate prior to the transfer to a transparent substrate and the femtosecond pump-probe measurements. While the flake is shown in blue color, the background appears in purple. Micro-Raman measure-

ments of the sample indicate the high quality since no disorder induced D-peak could be observed in the Raman spectrum. In panel (b) an optical microscope image in transmission of the same graphite flake after transfer and irradiation with intense fs-pulses is shown. Here, several concentric rings can be observed which appear as brighter areas in the image, highlighted by the red circle. The distance between each of the rings is decreasing from a value of $4\ \mu\text{m}$ to $1.5\ \mu\text{m}$ in radial direction going towards the center. The optical images give a first indication of structural modifications driven by the femtosecond laser pulses. In order to further investigate possible changes in the lattice structure and exclude optical interference effects, we measured Raman scattering spectra of the graphite flake. Raman scattering was chosen because this method detects defects in the lattice [49] and possible local changes in the number of layers (chapter A1 of this thesis). Fig.6.5(c) and (d) show a color-coded Raman map of the sample area shown in (b), indicated with a red circle, after fs-pulse irradiation. The graphite flake was scanned with a continuous wave 514 nm excitation laser at low intensity to avoid possible damage. At every pixel shown in the image a Raman scattering spectrum was taken and the integrated area of the 2D/D-mode is given in a color code. Fig.6.5(c) displays the integrated area of the D-peak and (d) the integrated area of the 2D-peak. The Raman map of the D-mode reflects defects within the sample investigated, as explained in section 2.4.2. As already mentioned above, no D-peak could be measured prior to the pump-probe measurements. After irradiation with intense fs-pulses the D-peak intensity was dramatically increased over the whole exposed area of the graphite flake. In some areas of the image, a large increase in the D-peak can be observed: (i) The concentric rings appearing in the optical image correspond to an increased D-peak intensity and (ii) the larger brighter area in the upper part, corresponding to the center of Fig.6.5(b) shows an increased D-peak intensity as well. The center of the flake corresponds to the center of the focused pump pulse. Assuming a gaussian intensity distribution of the laser pulse, one would expect a large defect density at this point, as is indeed observed in our Raman maps. Fig.6.5(d) displays the 2D-peak Raman map of the same area shown in (c). Again the concentric rings can be seen, but here indicating a reduced 2D-peak intensity. Prior to the measurements, the graphite flake was a multi-layer structure with about 18 layers. A reduced number of layers

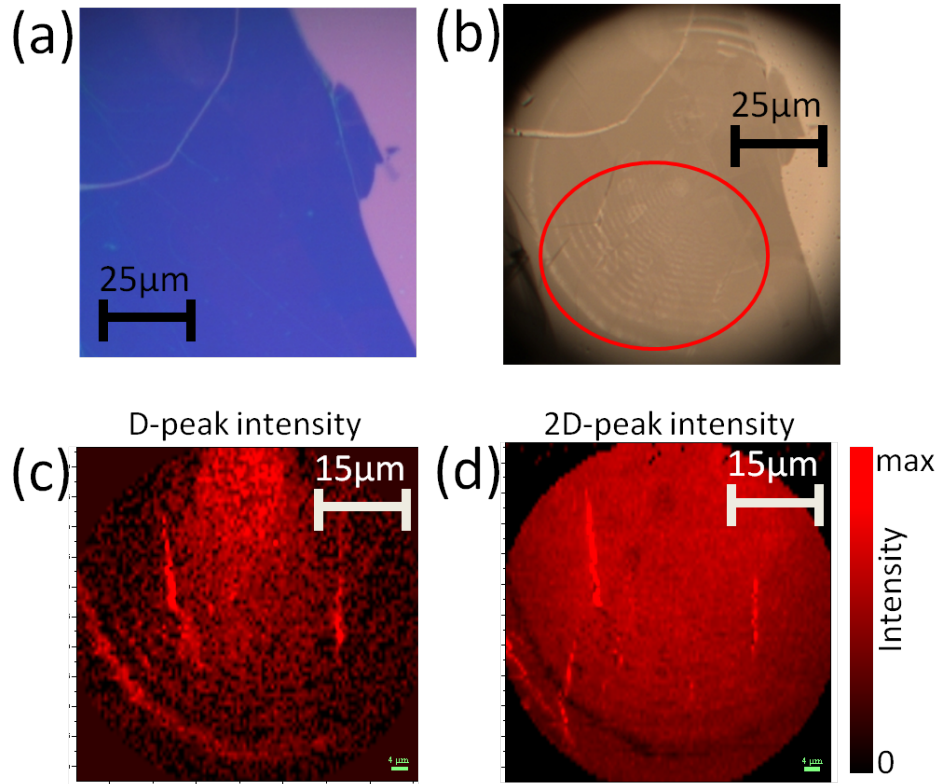


Figure 6.5.: (a) Optical microscope image in reflection of the graphite sample investigated on a Si/SiO₂ substrate prior to the transfer to a transparent substrate. The flake is shown in blue color. (b) Optical microscope image in transmission of the same graphite flake after transfer and irradiation with intense fs-pulses. Concentric rings can be observed which appear as brighter areas in the image. (c),(d) Color-coded Raman map of the red marked circle shown in (b) after fs-pulse irradiation. The graphite flake was scanned with a continuous wave 514 nm excitation laser at low intensity to avoid possible damage. At every pixel shown in the image a Raman scattering spectrum was taken and the integrated value of the D-mode (c) and 2D-mode (d) is given in a color code. Within both images, the concentric rings can be observed. Additionally, a brighter area in the upper part of (c) can be observed, which correspond to the center of (b), giving the center of the focused pump pulse.

would give a reduced Raman scattering signal for this multi-layer sample. Here, the Raman scattering spectrum suggests a decrease in the number of layers at the position of the rings. Therefore, the Raman spectra of the sample before and after irradiation with intense fs-pulses reveal clear structural modifications of the layers. The origin of the concentric rings is, nevertheless, not identified, but can

be correlated with an effect due to high intensity laser pulse irradiation. We have shown here that fs-laser pulses can induce structural changes in the graphite lattice. In the following section, we will relate these modifications with the observed increase in photoinduced absorption from the pump-probe experiments.

6.4. Lattice oscillations in graphite

Coherent lattice vibrations of the interlayer shearing mode On the basis of theoretical predictions [103, 104, 106], the measured photoinduced absorption in the dynamics at high carrier densities and low probe photon energies will be assigned to an initial ultrafast compression of the lattice. A subsequent expansion and oscillation of the graphite lattice after the initial compression is expected [92] and should be observable in the transients [98]. We analyzed the transient dynamics at a probe photon energy of 0.34 eV and a carrier density $n = 8.28 \times 10^{12} \text{ cm}^{-2}$. In order to isolate the oscillatory component from the measured transients of Fig.6.1(b), a stretched exponential fitting model was used to model the dynamics and subsequently subtract from the recorded data [109]. The upper panel in Fig.6.6(a) displays the subtracted result of the $\Delta T/T$ signal from 0 ps up to 16 ps time delay. A clear modulation of the signal with a decreasing amplitude of the oscillation with time can be observed. Obtaining information about the frequency of the oscillatory part we perform a Fourier-transform of the raw experimental data according to the equation:

$$F(\omega) = \frac{1}{\sqrt{2\pi}} \int_{-\infty}^{\infty} f(t)e^{-i\omega t} dt$$

with $F(\omega)$ being the Fourier transformed function of $f(t)$. Here, $f(t)$ corresponds to the recorded $\Delta T/T$ signal after subtraction of the stretched exponential. The result of a fast Fourier-Transformation is shown in the lower panel of Fig.6.6(a), which depicts the absolute value of the $F(\omega)$ as a function of $\omega = 1/s = \text{Hz}$. A clear peak at a frequency of 1.282 THz can be observed, corresponding to an energy of 42.8 cm^{-1} in wavenumber. The oscillation is attributed to the coherent phonon signal of interplanar shearing motion in multilayer graphene whose

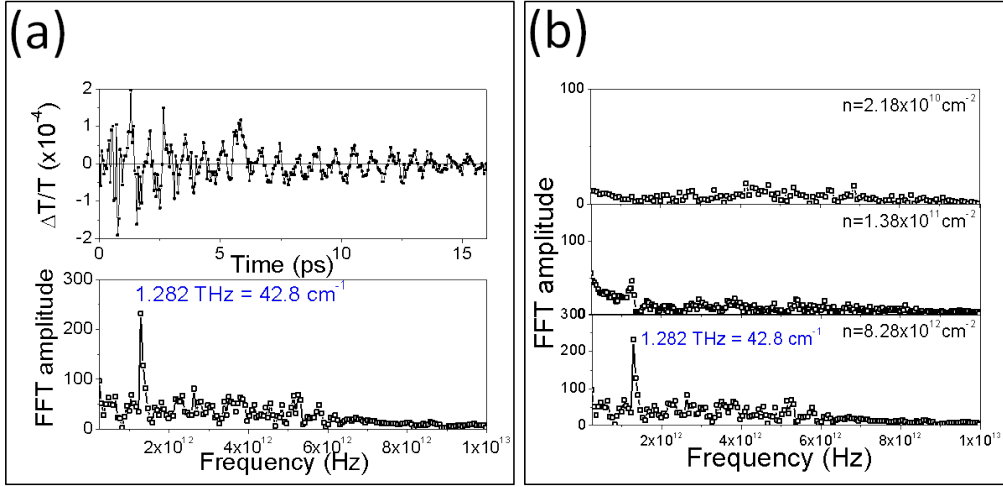


Figure 6.6.: (a) Upper panel: Subtracted result of the $\Delta T/T$ signal from 0 ps up to 16 ps time delay as explained in the text. A clear oscillation of the transmission signal with a decreasing amplitude with time can be observed. Lower panel: Fourier-Transformation of the experimental data shown in the upper graph. A peak at a frequency of 1.282 THz can be observed, which corresponds to an energy of 42.8 cm^{-1} . (b) Dependence of the oscillation on photoexcited carrier density over three orders of magnitude, $n = 2.18 \times 10^{10} \text{ cm}^{-2}$ (upper panel), $n = 1.38 \times 10^{11} \text{ cm}^{-2}$ (middle panel) and $n = 8.28 \times 10^{12} \text{ cm}^{-2}$ (lower panel).

vibrational energy is about 43 cm^{-1} [110]. The oscillation can be fitted by an expression for a damped oscillator, $\Delta T/T \propto -Ae^{-t/T_1} \cos(\Omega_0(t - t_0))$, where Ω_0 is the phonon frequency and T_1 the relaxation time of the coherent phonon [109]. From the fitting we extract a value of $T_1 = 8.3 \text{ ps}$. Raman et al. reported from ultrafast electron crystallography on graphite a diffraction intensity decrease indicative for interference between graphitic layers of $8 \pm 1 \text{ ps}$ [111], which is in remarkable agreement with our experiments.

Fig.6.6(b) illustrates the dependence of the oscillation peak amplitude in the frequency domain on photoexcited carrier density over three orders of magnitude, $n = 2.18 \times 10^{10} \text{ cm}^{-2}$ (upper panel), $n = 1.38 \times 10^{11} \text{ cm}^{-2}$ (middle panel) and $n = 8.28 \times 10^{12} \text{ cm}^{-2}$ (lower panel). At the lowest carrier density there are no oscillation and the peak can not be observed. At $n = 1.38 \times 10^{11} \text{ cm}^{-2}$ a peak with small amplitude can be observed and at the highest fluence a clear signal can be identified. The frequency as a function of the carrier density is rather

constant and is in the range $43 \pm 0.3 \text{ cm}^{-1}$. This value is in excellent agreement with values for the interlayer shear mode in multi-layer graphene recently measured by means of Raman scattering [110].

Discussion We now turn to the physical interpretation of the observed strong absorption and the subsequent oscillations in the measured transient signal. Fig.6.7(a) shows again the $\Delta T/T$ for a probe photon energy of 0.34 eV and a photoinduced carrier density of $n = 8.28 \times 10^{12} \text{ cm}^{-2}$. Three different temporal regimes are indicated, which will be discussed in the following. In (1), before

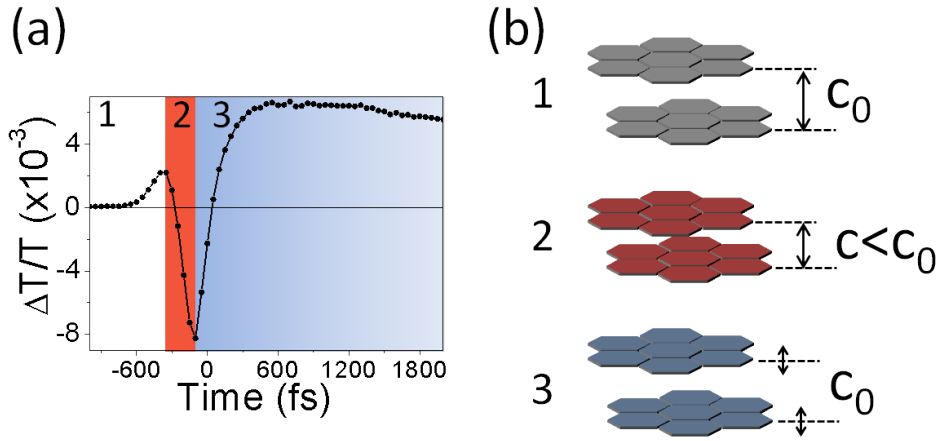


Figure 6.7.: (a) $\Delta T/T$ for a probe photon energy of 0.34 eV and a photoinduced carrier density of $n = 8.28 \times 10^{12} \text{ cm}^{-2}$. Three different temporal regimes are indicated, which will be discussed in the text. (b) Sketches illustrating the interplanar distance c_0 between two layers in the graphite for the three different temporal regimes.

the arrival of the pump pulse, at $t < -600$ fs the transmission change is zero. Due to the high intensity of the pump pulse, starting at $t = -600$ fs the transmission change is increasing, indicating photobleaching due to blocking of optically coupled states. The interplanar distance in this regime is supposed to be the equilibrium value of $c_0 = 3.35 \text{ \AA}$, Fig.6.7(b). The following strong decrease in the measured transmission (2) takes about 200 fs up to a maximum photoinduced absorption at $t = -100$ fs. During the electronic thermalization, emission of strongly coupled optical phonons takes place because of the anisotropic band structure of graphite [99, 112]. These phonon modes are mainly in-plane vibrations of the

carbon atoms followed by a slower c-axis shearing motion of the planes. The in-plane vibrations allow a different stacking of the layers along the c-axis, similar to an uniaxial pressure applied to the crystal [106]. A significant movement of the atoms perpendicular to the graphite planes in the preablation regime was predicted in molecular dynamics simulation in Ref. [103].

Calculations based on ab initio density functional theory (DFT) in Ref. [111] studied the effect of laser pulses on the electronic structure and bonding in graphite. They show that changes in the charge density modify the force field in the system. The authors suggest an increased population of the $2p_z$ -Orbitals, which are perpendicular to the plane, and may hybridize to $pp\sigma$ bonding states connecting neighboring layers and therefore increasing their attraction. Indeed, Carbone et al. correlated electronic structural changes from time-resolved electron energy loss spectroscopy measurements on graphite to a change from sp^2 to diamond-like sp^3 electronic hybridization during compression of the lattice [94]. In Ref.[111] the authors calculate the charge density for zero temperature $\rho(\mathbf{r})=\rho(\mathbf{r},T=0)$ and the change in the charge density $\Delta\rho(\mathbf{r})=\rho(\mathbf{r},k_B T_e)-\rho(\mathbf{r},T=0)$ for an increased temperature of about $k_B T=1.0$ eV due to population of initially empty conduction states by valence electrons. For details of the calculation see Ref. [111]. Optical excitation by a laser pulse leads to an increased temperature of the electronic system after the initial thermalization of a nonequilibrium population. The resulting increase in the charge density in the plane perpendicular to the graphite lattice is responsible for the increased attraction between two neighboring layers.

Further calculations showed that an electronic temperature of about $k_B T=1.0$ eV leads to a maximum interlayer contraction $\Delta c/c_0=-1\%$ [111]. Marinopoulos et al. [113] predict by means of DFT calculations a very strong dependence of the optical absorption on the interlayer distance in graphite. For light polarized in the plane of the lattice an increase in the optical absorption at energies below 1 eV with decreasing interlayer spacing was shown. In addition to this, Jeschke et al. [104] reported on the time dependence of the energy absorption of graphite upon excitation with femtosecond laser pulses. Depending on the pulse duration they calculated the electronic density of states (DOS) at different times with respect to photoexcitation. The results predict a strong increase of optical absorption

during the action of the laser pulse which is attributed to a very high DOS that has established around the Fermi level.

The depopulation of excited states due to carrier-carrier and carrier-phonon scattering, on the other hand, should cause the following in-layer expansion. The expansion is expected to start in the temporal regime (3), as indicated in Fig.6.7(a). The expansion of the lattice is then accompanied by an eigenmode of the crystal Hamiltonian, namely the E_{2g} interplane shearing eigenmode of the graphite lattice as observed in our data. The time constant observed in the decay of the oscillatory component, $T_1 = 8.3$ ps, may reflect the interplay between the repulsive Coulomb force and the restoring van der Waals force. It remains an open question which of the layers contribute to the compression and expansion. In Ref. [114] the authors suggest that due to surface charging of the topmost layers of graphite upon strong laser excitation only these layers contribute to the interlayer motion.

Together with the increase in absorption predicted in Ref.[106, 113] for the probe photon energy in our measurements we assign the observed strong photoinduced absorption as a direct consequence of an initial compressed lattice. The compression of the lattice along the c-axis is induced by the intense femtosecond laser pulses. The reduced interlayer distance is responsible for an increased optical absorption. Interestingly, we have observed the photoinduced absorption in different few-layer samples, 2-layer, 3-layer and 5-layer, but not in the case of only 1-layer graphene as depicted in Fig.6.1(a). This is a very important point since the absence of the strong absorption for a single layer of graphene further supports the picture that a c-axis distance change for $N_l > 1$ layer graphene is responsible for the increased absorption in the samples investigated here.

6.5. Summary

Summarizing, we report direct observation of ultrafast compression and expansion of the c-axis graphite lattice induced by intense fs laser pulses. At high carrier densities, a strong temporal limited photoinduced absorption appears in the first hundreds of femtoseconds followed by photoinduced bleaching with a

superimposed oscillation of the signal. The ultrashort increase in absorption is attributed to an initial compression along the c-axis of the graphite lattice induced by photo-excited coherent phonons leading to a structural modification of the atomic lattice. In the following c-axis expansion, the transients are accompanied by coherent oscillations with the frequency of the interlayer (E_{2g}) shearing mode showing temporal characteristics of a damped oscillation.

7. Conclusions and outlook

The aim of this work is to understand the energy loss mechanism in graphene and few-layer graphene after ultrashort photoexcitation. In particular, by modifying the initial photoinduced carrier density, the electronic structure and the conditions of the ultrashort excitation, important information could be found by means of femtosecond differential transmission spectroscopy. We were able to address questions relevant for possible applications and for the advancement of graphene in optoelectronic devices.

In the first chapter, we analyzed the energy loss channels of photoexcited carriers in 2-layer graphene and the influence of different initial photoinduced carrier densities. For this purpose, 2-layer graphene samples were produced by mechanical exfoliation of natural graphite flakes. Femtosecond differential absorption spectroscopy in the photon energy range from 0.25 eV to 1.3 eV was used to investigate the temporal changes in the absorption. By modelling the recorded transients, we were able to extract the carrier temperature as a function of time and initial carrier density. From the cooling curves, the power loss of the photoexcited system could be calculated, showing two different temporal regimes of carrier cooling dominated by optical and acoustic phonon emission.

Due to the high optical phonon energy in graphene cooling via optical phonon emission is very efficient and within hundreds of femtoseconds a hot phonon population is established. The optical phonons decay by anharmonic coupling into acoustic phonons on a slower picosecond timescale. Here, the experimental data show that for increasing carrier density the crossover between the two regimes occurs at larger carrier temperatures since cooling via optical phonons experiences a bottleneck. As cooling via acoustic phonons is less sensitive to saturation effects, we could show that acoustic phonons exhibit an increasing contribution to the energy loss at high carrier densities. These results about the dynamics of car-

riers at elevated temperatures addresses important questions regarding ultrafast optoelectronic devices where transport is dominated by hot carriers.

In order to further reveal the importance of the electronic structure on the carrier dynamics in graphene, we modified the latter by changing the number of stacked graphene layers. Calculations based on a tight binding model predict a modification of the electronic and optical properties of few-layer graphene samples with increasing number of layers. In the photon energy range of 0.3 eV up to 0.7 eV we are sensitive to the subband-structure of few-layer graphene. While for a high photoinduced carrier density the differential absorption spectrum is dominated by photoinduced bleaching due to Pauli blocking of the interband optically coupled states at low carrier densities the spectra show an evolving structure of photoinduced absorption bands superimposed on the bleaching. Supported by tight binding model calculations of the electronic structure, we assigned the photoinduced absorption features to intersubband transitions as the number of layers is increased. Interestingly, the intersubband photoinduced transitions show slower dynamics than the interband bleaching. Due to their independence from the absolute energy value of the carriers with respect to the Dirac point, the lifetime of these intersubband transitions depends exclusively on the lifetime of the photoinduced carriers. Thus, experiments provide an elegant method to measure the carrier recombination lifetime in a class of zero gap semiconductor such as few-layer graphene. Carrier recombination in graphene and few-layer graphene is of relevance for many different applications in optoelectronics. For example the total intrinsic response time τ_r of photodiodes is given by $\tau_r^{-1} = \tau_{rec}^{-1} + \tau_t^{-1}$ [82], with the carrier recombination time τ_{rec} and the transit time τ_t .

Further experiments performed by increasing the fluence of the photoexcitation in multi-layer graphene revealed new transient optical phenomena. At mid-infrared photon energies, the differential transmission dynamics of multi-layer graphene at a high level of photoexcitation displayed a strong temporal limited increase in absorption within the first hundreds of femtoseconds after photoexcitation. The amplitude of the absorption change strongly depends on the probe photon energy, the pump pulse intensity and the temporal duration of the pump pulse. After about one picosecond the differential transients display photoinduced bleaching, with a superimposed oscillatory behaviour of the signal amplitude. A

Fourier-transformation of this oscillation yields a frequency of about 43 cm^{-1} . The observed characteristics can be assigned to an initial compression along the c-axis of the graphite lattice followed by an expansion and subsequent damped oscillation. The increase in absorption is correlated to the compression of the lattice and an electronic sp^2/sp^3 like hybridization along the c-axis induced by a structural modification of the carbon atoms. The latter is a direct consequence of the high level femtosecond irradiation and responsible for the change in the optical properties. Micro-Raman measurements after irradiation verified structural modifications of the sample. The frequency of the observed oscillation matches the interlayer shearing mode of graphite showing characteristics of a damped oscillation on the picosecond timescale. The relevance of these findings are important in terms of fundamental physics because they demonstrate how femtosecond pulses can transform the solid into either the strongest three-dimensional material, diamond, or the only two-dimensional crystal known.

Some questions connected with the dynamics of carriers in graphene and few-layer graphene at elevated temperatures remain unanswered and might be interesting for future projects. A quantitative comparison of the power loss for a 2-layer graphene, displaying a more quadratic energy dispersion, with the power loss of 1-layer graphene, which, on the other hand, shows a linear dispersion for carrier energies $< 1\text{ eV}$ would be of great interest because most of the applications and devices presented up to date are based on 1-layer graphene and make use of the unique properties of this material. Additionally, due to the lack of an inter-subband structure in 1-layer graphene, the method presented within this work to obtain the carrier recombination lifetime is not applicable for this special case. Graphene is an ideal material for e.g. photodetectors because of a short carrier recombination and transit time. Additionally, when compared to the established GaAs and InGaAs device technology graphene exhibits no bandgap for photon absorption. Another very interesting future work would be to investigate the pre-ablation regime of multi-layer graphite at high levels of femtosecond irradiation. With the differential transmission technique, it should be possible to determine the energy necessary to ablate single graphene layers from a multi-layer structure and gain information about this dynamic process connecting sp^2 and sp^3 materials. Conclusively,

A. From graphene to graphite: Evolution of the 2D Raman peak

In the following chapter, we describe Raman scattering in few-layer graphene samples from 4-layer graphene up to a multi-layer structure of 35-layers. By carefully analyzing the 2D-peak in the spectrum, we could directly connect changes in the mode to the evolution of the band structure as the number of layers is increased.

A.1. Physical background Raman scattering in graphene

Raman scattering spectroscopy on graphene and graphite has so far mainly focused on the characterization of 1-layer, 2-layer graphene and graphite [64]. The two most prominent peaks appearing in the Raman spectrum of graphene/graphite are the G- and 2D-mode. While the shape of the G-mode exhibits only little change when going from graphene to graphite, the 2D-peak dramatically changes shape, thus being sensitive to the number of layers. Here, we fill the gap and monitor the changes of the 2D-peak with increasing number of layers from 4-layer graphene up to a multi-layer structure of 35-layers, which can be considered as the bulk graphite limit. The changes in position and intensity of the peaks are clearly connected to the electronic structure and give important information about relevant electron-phonon scattering events responsible for the 2D-peak in the Raman spectrum of graphite.

A.2. Raman spectrum of graphite and graphene

Raman scattering is a powerful tool to investigate characteristic properties of carbon based nanostructures, like carbon nanotubes or graphene. Ferrari et al. reported on a way to distinguish between 1-layer and 2-layer graphene by analyzing the shape and position of the 2D-mode in the Raman scattering spectrum [64]. Maultzsch et al. could relate the D-band in the spectrum of graphene and graphite to defects in the material [49] as was discussed in section 2.4.2.

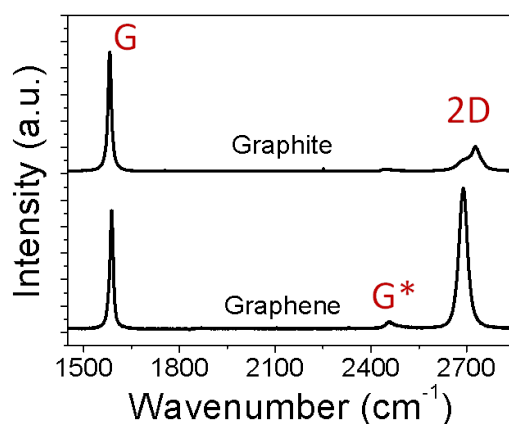


Figure A.1.: High frequency Raman scattering spectrum of graphite (top graph) and 1-layer graphene (lower graph), showing the two most prominent peaks, the G-mode at $\approx 1580 \text{ cm}^{-1}$ and the 2D-mode at $\approx 2700 \text{ cm}^{-1}$. Additionally the G*-mode is shown.

Fig.A.1 depicts the Raman spectra of 1-layer graphite and graphene. While the shape of the G-peak shows almost no change when going from graphite to graphene, the 2D-peak changes in shape and position. The 1-layer 2D-peak can be fitted by a single-lorentzian mode, as already mentioned in section 3.1.5. There, we showed that the number of subpeaks of the 2D-band is related to the electronic structure, for example the number of bands. For a 1-layer with only one band in the conduction (CB) and valence band (VB), the 2D-peak can be well reproduced with a single lorentzian line. Already for 2-layer with two bands in the CB and VB, four possible transitions give the four subpeaks of the 2D-mode [64]. In 3-layer graphene, 9 different transitions would be expected for an inter-valley scattering from K to K' in the Brillouin zone considering the electronic

band dispersions or 15 with group symmetry arguments as shown in Ref. [115]. Due to the small energy difference between some of these possible transitions, not all of them can be seen in the 2D peak [51]. For graphite, a very large number of transitions and peaks is expected. But, the 2D-peak of graphite can be well fitted with only two Lorentzian lines, this is the common model in the literature. But up to date, there is no detailed work on the evolution of this layer-number sensitive peak considering the gap between few-layer graphene and graphite. In this chapter, we want to investigate the change of the 2D-peak as a function of the number of layers of the sample and look at the evolution of this peak from 4-layer graphene to bulk graphite.

A.3. 2D Raman peak vs. number of layers

As we have shown above, the 2D-peak in the Raman spectrum of multi-layer graphene samples is sensitive to the number of stacked graphene layers in the sample investigated. In this section, we will focus on the 2D-peak and investigate the evolution of this mode with increasing number of layers. Fig.A.2 shows a zoom of the 2D-peak of $N_l=1,2,3,4$ and 5-layer graphene, at a laser energy of 2.41 eV. All samples are prepared with the mechanical exfoliation method from natural graphite flakes, described in chapter 2 of this work. When necessary, the graphene flakes are transferred to transparent substrates to perform further experiments. In the graphs the Raman spectrum is given by the black line, the red line is the sum of the single Lorentzian subpeaks, shown in green color. The Raman spectrum of 1-layer and 2-layer is already discussed in section 3.1.5. Fig.A.2(a)-(e) shows that for every additional layer the 2D-peak displays a different shape. And additionally, up to 5 layers the peak shifts to higher wavenumber, in which the biggest frequency shift is between 1-layer and 4-layers. By comparing the 2D-peak of 4-layer and 5-layer, two characteristics are apparent: (i) the shape can be well reproduced by a superposition of only two single Lorentzian-peaks and (ii) the frequency of the peak is almost fixed at $\approx 2700 \text{ cm}^{-1}$. In the following we will focus on these two aspects when analyzing the evolution of the 2D-mode in few-layer graphene. The lower wavenumber peak will in the following be labeled ω_{2D1} , the

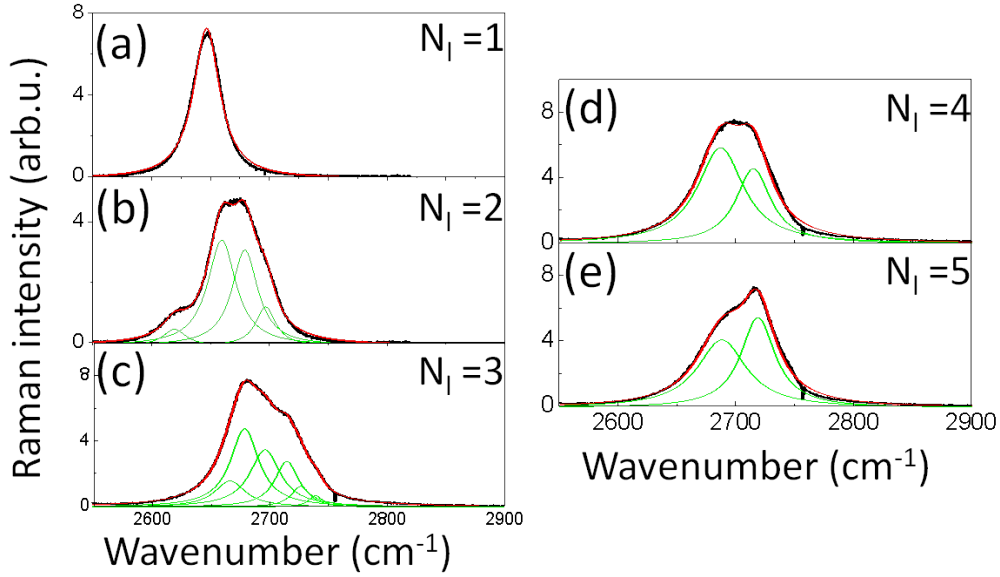


Figure A.2.: Zoom of the 2D-peak of $N_l=1,2,3,4$ and 5-layer graphene samples (black curves). While the 2D-peak of 1-layer graphene displays a single Lorentzian line shape (red curve), the 2-layer graphene 2D-mode can be well reproduced with a superposition of four subpeaks (green curves). The characteristic shoulder on the low wavenumber side is clearly visible. The 2D-mode of 3-layer graphene can be reproduced with six subpeaks and is blue shifted to $\approx 2700 \text{ cm}^{-1}$. 4-layer and 5-layer can be fitted with two single subpeaks and from 5-layers the shape is already similar to the graphite 2D-peak.

higher wavenumber peak with ω_{2D2} . Considering the electronic structure, already 10-layer graphene shows some characteristics of bulk graphite [14]. One question we want to answer here with Raman scattering is, at which number of layers the 2D-peak is identical to the 2D-peak of bulk graphite. We define bulk graphite from atomic force microscopy measurements to have more than 50 layers.

In Fig.A.3, plots of the 2D-mode of 5-layer and 15-layer are compared to the one for bulk graphite. Theoretically, the two-peak structure of the 2D-mode in HOPG (highly oriented pyrolytic graphite, $N_l \rightarrow \infty$) is the result of a convolution of an infinite number of allowed double resonance processes [51]. In

Fig.A.3(a) we can see that, while the position of the higher frequency subpeak ω_{2D2} is almost constant, the lower frequency subpeak ω_{2D1} is redshifted to lower wavenumbers. Fig.A.3(b) compares the relative intensity of the two subpeaks for 5-layer, 15-layer and bulk graphite. Here, a relative intensity change between the two subpeaks can be observed, indicated by the orange vertical arrows, with a decreasing contribution of the ω_{2D1} subpeak to the overall 2D-mode intensity with increasing number of layers. In order to analyze the observed characteristics,

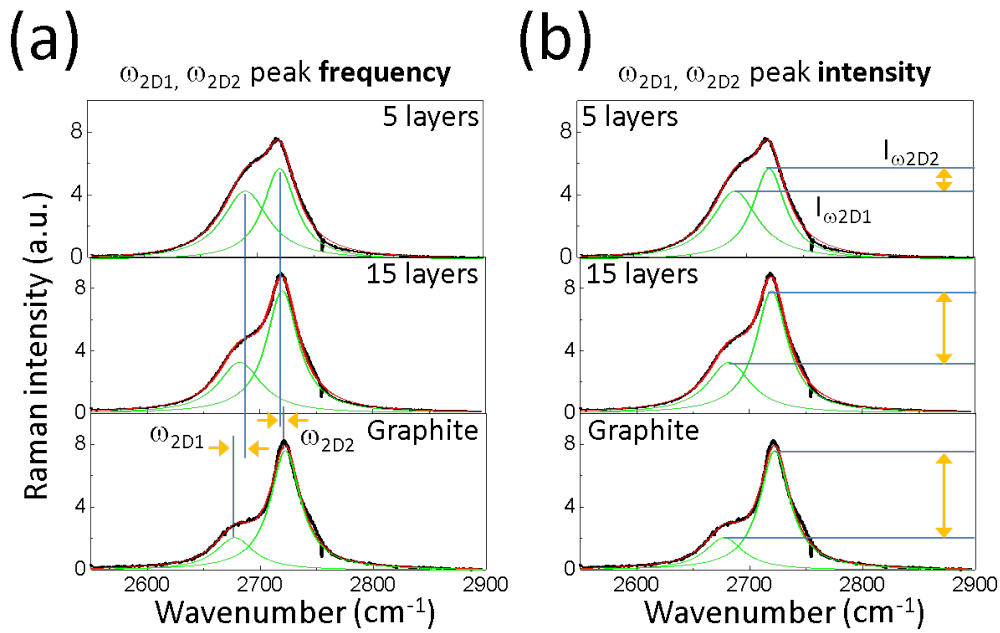


Figure A.3.: Comparison of the 2D-mode of 5-layer and 15-layer to the one for bulk graphite. The black lines indicate the measured data, the red curve is the sum of the single subpeaks, shown in green color. (a) displays the change in the position of the two subpeaks (green curves). While the position of the higher frequency subpeak ω_{2D2} is almost constant, the lower frequency subpeak ω_{2D1} is redshifted. In (b) the change in the intensity $I_{\omega_{2D1}}$ and $I_{\omega_{2D2}}$ of the two subpeaks is shown. Here an intensity change can be seen with a decreased intensity of the ω_{2D1} subpeak relative to ω_{2D2} .

we performed a detailed study and measured different multi-layer samples from 4-layer up to 35-layer. Details of the sample preparation are given in chapter 3. For every flake, the height was carefully measured with atomic force microscopy determining the exact number of layers. Raman measurements were performed

with laser energies 1.92 eV, 2.41 eV and 2.70 eV at room temperature and ambient conditions and for all measurements the laser intensity was kept below the damage threshold. Analyzing the 2D-peak as a function of layer number, the peaks were modelled with a superposition of two lorentzian lines and the frequencies of the two subpeaks ω_{2D1} and ω_{2D2} as well as their relative intensities $I_{\omega_{2D1}}/I_{\omega_{2D2}}$ were determined. Fig.A.4 displays the result of this analysis. In (a) the frequency

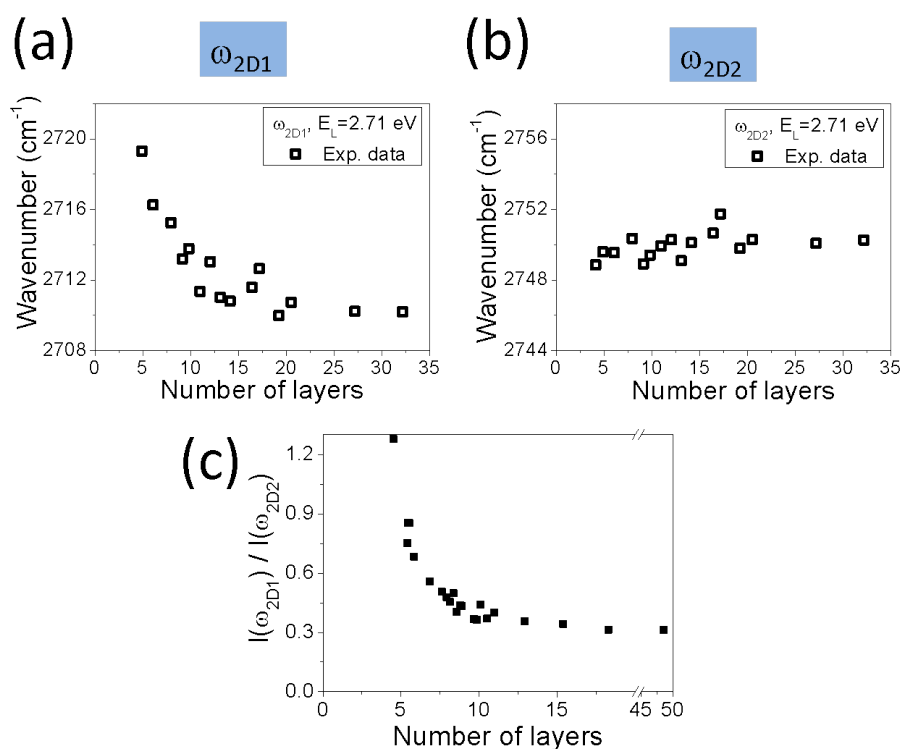


Figure A.4.: Detailed experimental data for the (a) ω_{2D1} frequency, the (b) ω_{2D2} frequency and their relative intensities $I_{\omega_{2D1}}/I_{\omega_{2D2}}$ as a function of the number of layers. A discussion is given in the text.

of the ω_{2D1} and in (b) the frequency of the ω_{2D2} subpeak is plotted against the number of layers. For ω_{2D1} , a clear correlation to the layer number is visible with an initial red shift of the frequency which is reaching the bulk-value limit at roughly 12-15 layers. ω_{2D2} on the other hand displays only a light blueshift of the frequency. The intensity ratio of the two subpeaks shown in Fig.A.4(c) depicts a similar trend as observed for the ω_{2D1} frequency. Gupta et al. reported on a

similar red shift of the G-peak wavenumber vs. number of layers [116]. They attributed the observed behaviour to a change of the electron and phonon states with increasing number of layers. In the following, we will explain the experimental findings with a detailed study of the electron-photon and electron-phonon scattering processes, considering the evolution of the electronic band structure as the layer number is changed.

A.4. Calculation of the phonon density of states

In this section, we will connect the observed changes in the frequencies ω_{2D1} and ω_{2D2} with changes in the electronic band structure and with the electron-phonon scattering process responsible for the 2D-peak in the graphite Raman spectrum. The theoretical background for this chapter is discussed in section 2.3 and 2.4. Due to the enormous computational effort in the calculation of the whole Raman scattering spectrum [29, 45] we introduce a simplified model to qualify the observed findings. Fig.A.5(a) gives an illustration of the double resonance Raman scattering process responsible for the 2D-peak together with a sketched band structure for 1-layer graphene at the K- and K'-point in the Brillouin zone. A photoexcited electron (1) with wavevector \mathbf{k}_i and energy $E_i = \frac{E_{Laser}}{2}$ scatters by emitting/absorbing a phonon (2) with wavevector \mathbf{q} and energy $\hbar\Omega(\mathbf{q})$ from the K- to the K'-point with wavevector \mathbf{k}_f and energy $E_f = \frac{E_{Laser}}{2} \pm \hbar\Omega(\mathbf{q})$ and back (3) and subsequently recombines (4). The phonon wavevector is given by momentum conservation, $\mathbf{q} = \mathbf{k}_i \pm \mathbf{k}_f$, with \mathbf{q} measured from the Γ -point. The energy of the incoming photon together with the band structure of the graphite sample defines an energy contour for the possible \mathbf{k}_i states. For one possible scattering event this situation is sketched in Fig.A.5(b). The electron can scatter from the K-point at \mathbf{k}_i , given by the blue thick triangle, to a subset of states \mathbf{k}_f at the K'-point, given by the purple triangle. All calculated possible phonon wavevectors for one initial \mathbf{k}_i are shown by the green area in Fig.A.5(b). A manifold of possible phonon wavevectors result from one initial electron state \mathbf{k}_i . If we compute all possible phonon modes with wavevector \mathbf{q} connecting \mathbf{k}_i and \mathbf{k}_f , we can calculate a phonon density of states (DOS). Fig.A.5(c) displays

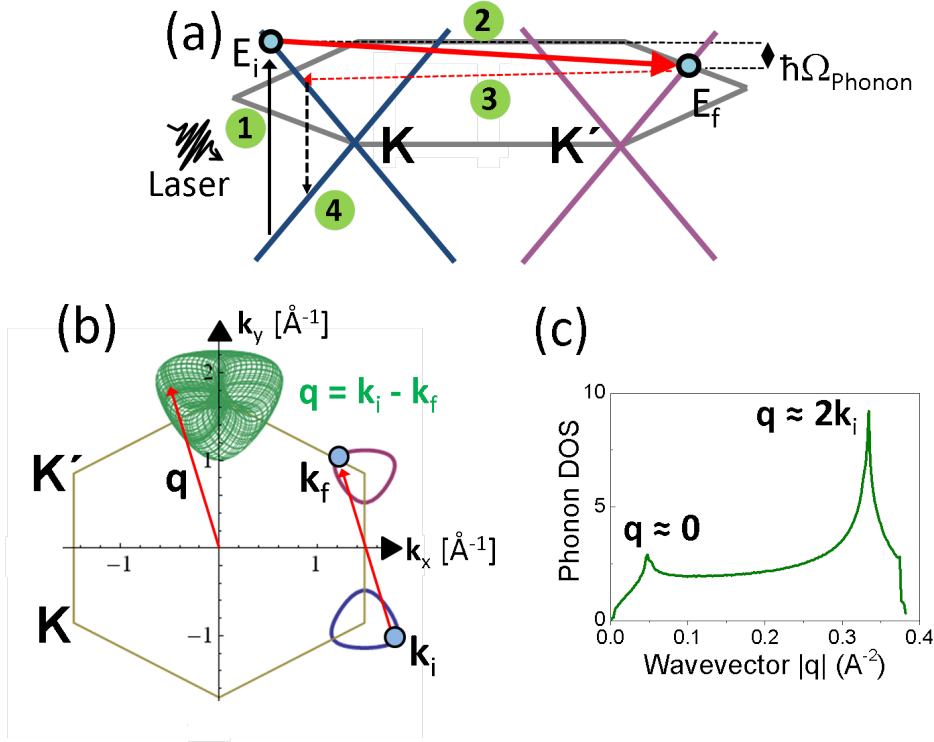


Figure A.5.: The second order Stokes resonance Raman scattering in the graphene sheet. (a) hexagonal Brillouin zone together with a schematic of the electronic band structure around the K- and K'-point. The vertical and horizontal arrows indicate (1) light absorption, (2) and (3) phonon emission and (4) light emission. (b) One of the possible second order Stokes resonance Raman scattering processes involves the emission of a phonon with wavevector \mathbf{q} . The set of all phonon wavevectors which are related to transitions from points on the two triangles around K and K' gives rise to the collection of small triangles shown in green, obeying momentum conservation $\mathbf{q} = \mathbf{k}_i \pm \mathbf{k}_f$. (c) The calculated density of states from the set of phonon wavevectors shown in (b) as a function of the absolute phonon wavevector \mathbf{q} measured from the K-point.

the calculated phonon DOS as a function of the absolute value of the phonon wavevector \mathbf{q} . While the larger peak at $\mathbf{q} \approx 2\mathbf{k}_i$ give rise to the second order Raman features in the graphite Raman spectrum [117], the smaller peak at $\mathbf{q} \approx 0$ are suppressed by negative interference at Γ , K and K' points, as shown in Ref. [45] and hence do not contribute to the Raman spectrum.

The calculations so far considered 1-layer graphene with only one conduction and valence band. For this special case, there is only one possible inter-valley

scattering event connecting different bands between K and K' point. For 2-layer graphene with a subband structure of two bands, there are already four possibilities, giving rise to the observed four subpeaks in the 2D-peak. For 3-layer graphene, there are 9 possibilities, for 4-layer 16 and so on. Due to the phonon dispersion of the iTO branch around the K point in graphite, the energetic difference between these transitions will be very small. That is why, e.g. the 9 possible subpeaks for a 3-layer graphene can not be distinguished in the corresponding 2D-peak.

In a very simplified model, we will only look at two different inter-valley transitions in multi-layer graphene, as is illustrated in Fig.A.6(a). Here the energy contours for a laser energy of 1.2 eV at the K- and K'-point is shown for a 5-layer sample. Five concentric bands can be observed at the K- and K'-point in the BZ, which are the five subbands in the conduction band. From now on we will use the following notation for the subbands in the conduction band of a N_l -layer sample. The energetic lowest conduction band will be labeled CB_1 , the second lowest CB_2 and so on until the highest energetic conduction subband CB_{N_l} . In Fig.A.6(a) for example, the highest conduction band CB_{N_l} is displayed as the innermost band at the K-point. For the calculation we will consider only phonon modes connecting electronic states between the bands CB_{N_l} (in the figure $N_l=5$ for the 5-layer, green horizontal arrow) and CB_1 (red horizontal arrow). This assumption will be justified in the following. The electron-phonon interaction is expressed by the electron-phonon matrix elements, derived with the help of Eq.2.44 and the phonon dispersion of graphite calculated with Eq.2.43. The 2D-mode comes from an inter-valley double resonance Raman process involving an electron with wavevector \mathbf{k}_i in the vicinity of the K-point and two iTO-phonons with wavevectors $\mathbf{q} \approx 2\mathbf{k}_i$, where both \mathbf{k}_i and \mathbf{q} are measured from the K-point [51]. In Fig.A.6(b) we plot the absolute value of the electron-phonon matrix element for a phonon emission process, where an iTO-phonon connects two electronic states at \mathbf{k}_i in CB_m and \mathbf{k}_f in CB_n with $m, n = 1, \dots, 5$. For simplification, we do not consider the backscattering process from K' back to the K-point in the calculation, as for the 2D-peak the two states involved in this process are again connected by an iTO-phonon. For the subset of possible transitions between two bands, the mean value of the absolute matrix element is calculated

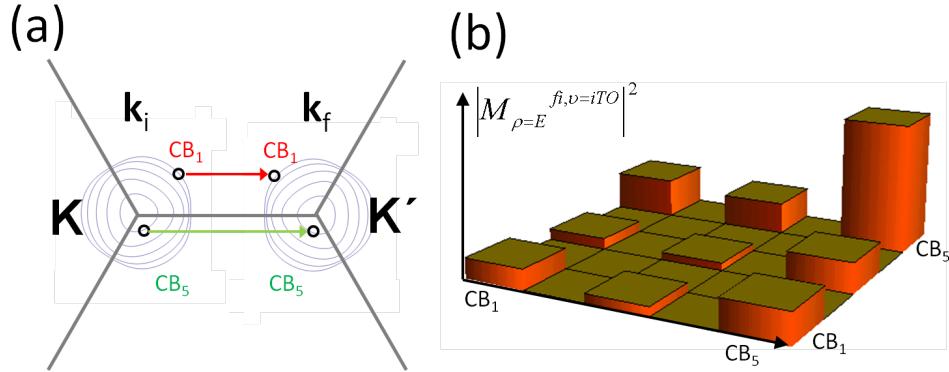


Figure A.6.: (a) Energy contours for a laser energy of 1.2 eV at the K- and K'-point for a 5-layer sample. Five bands can be observed at the K- and K'-point in the BZ, which are the five subbands in the conduction band. Only phonon modes connecting electronic states between the bands labeled CB_5 (green horizontal arrow) and CB_5 (red horizontal arrow) are considered in the model explained in the text. (b) Absolute value of the electron-phonon matrix element for a phonon emission process, where an iTO-phonon connects two electronic states at \mathbf{k}_i in CB_m and \mathbf{k}_f in CB_n with $m, n = 1, \dots, 5$, calculated with Eq.2.44.

and shown in Fig.A.6(b). From the graph, we see that, while the transitions connecting CB_5 - CB_5 show the biggest interaction strength, the transition CB_1 - CB_1 is about 1/4 of this value. Since the iTO-phonon increases its frequency with increasing wavevector \mathbf{q} , measured from the K-point, the highest frequency of a 2D-subpeak for a given laser energy E_{Laser} is associated with the transition showing the largest wavevector \mathbf{q} . So in the following, we will mainly focus on the transitions displaying the largest and the lowest wavevector \mathbf{q} , which are CB_{N_l} - CB_{N_l} and CB_1 - CB_1 , respectively. We will now try to model the experimental data. We calculate the phonon DOS and look at the evolution of the $\mathbf{q} \approx 2\mathbf{k}_i$ peak in the DOS (see Fig.A5(c)), as a function of the number of graphene layers for phonons connecting the electronic bands CB_{N_l} - CB_{N_l} and CB_1 - CB_1 , with N_l the number of layers. Fig.A7 shows again the experimental data for the (a1) ω_{2D1} and (a2) ω_{2D2} subpeak correlation with the number of layers, together with the calculated position of the $\mathbf{q} \approx 2\mathbf{k}_i$ peak for (b1) CB_{N_l} - CB_{N_l} and (b2) CB_1 - CB_1 transitions. From the graphs presented here, it is clearly visible that the model qualitatively reproduces the experimental data of the Raman measurements. As we did not calculate the Raman spectrum and hence can not directly compare the

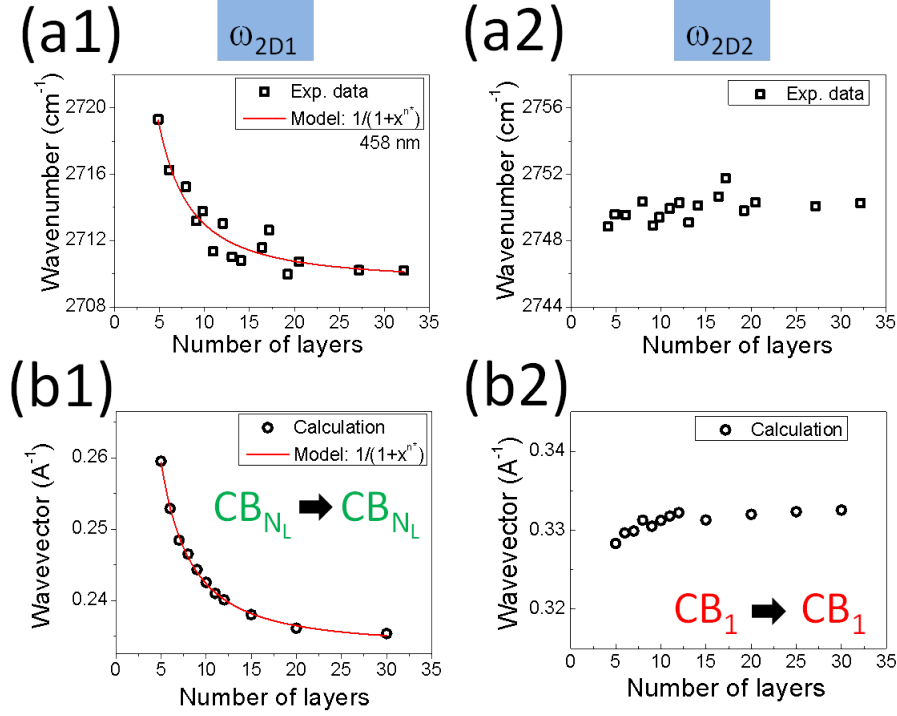


Figure A.7.: The experimental data for the (a1) ω_{2D1} and (a2) ω_{2D2} subpeak correlation with the number of layers, together with the calculated position of the $\mathbf{q} \approx 2\mathbf{k}_i$ peak for (b1) $CB_{N_L}-CB_{N_L}$ and (b2) CB_1-CB_1 transitions.

actual frequencies we used a model introduced by Wang et al. for the evolution of the G-peak in multi-layer graphene [118]. By calculating the phonon dispersion of graphene and graphene layers they found the relation $\omega_G = 1581.6 + 11/(1 + N_l^{1.6})$ for the frequency of the G-peak as a function of number of layers. We used a similar model to compare experiments and calculation, $\omega_{2D1} = \omega_0 + A/(1 + N_l^{n^*})$ with the bulk limit frequency ω_0 and the two fitting parameter A and n^* . The frequency of the subpeak ω_{2D1} from the Raman experiments with laser excitation energies 1.92 eV, 2.41 eV and 2.7 eV is fitted with this model and the parameter n^* was compared to n^* derived from the calculations. Fig.A.8 displays the result with the experimental data in black squares and an error bar from the fitting procedure and the calculated parameter values for different transitions in triangles indicated with different colors. The fitting parameter shows a dispersive behaviour with an increasing value with increasing laser energy which is directly

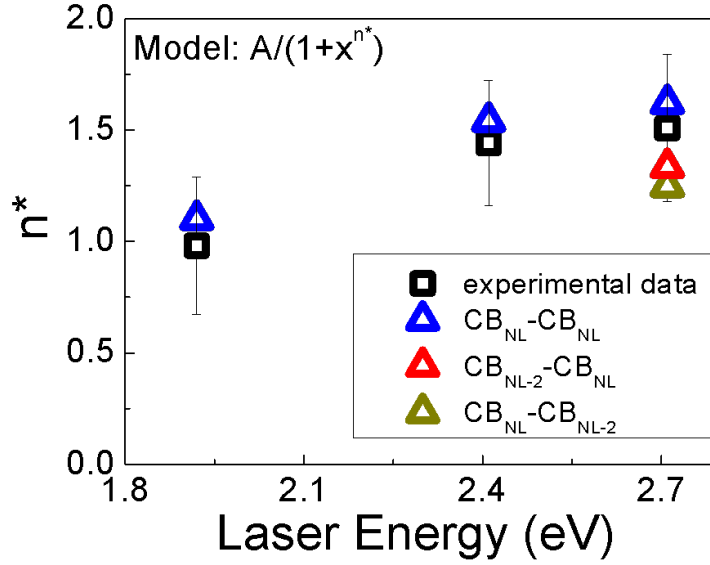


Figure A.8.: Fitting parameter n^* from the model indicated in the graph for the experimental data in black squares with an error bar from the fitting procedure and the calculated parameter values for different transitions in triangles indicated with different colors.

connected to changes in the electronic structure. A similar trend was e.g. shown in the dispersive behaviour of the four subpeaks that comprise the 2D-peak in 2-layer graphene as a function of laser energy in ref. [119]. The calculated fitting parameter n^* for the $CB_{N_i}-CB_{N_i}$ transition (blue triangles) can reproduce the observed behaviour of the experimental data at all laser energies. Additionally, n^* is shown for the transitions $CB_{N_i-2}-CB_{N_i}$ and $CB_{N_i}-CB_{N_i-2}$. For these transitions the calculated electron-phonon matrix element is displayed in Fig.A.6(b). Unfortunately, the calculated values are within the error bars of the experimental derived values. Therefore, the ω_{2D1} subpeak cannot clearly be assigned to the transition between the bands $CB_{N_i-2}-CB_{N_i}$. The transitions between bands $CB_{N_i}-CB_1$ and $CB_1-CB_{N_i}$, which show a larger electron-phonon coupling as well, as displayed in Fig.A.6(b), give a fitting parameter of $n^* > 2$ for a laser energy of 2.71 eV (not displayed in the figure). A more detailed investigation of the complete Raman scattering spectrum including the multi-layer graphene phonon

dispersion would probably be necessary to explain the findings, but this is beyond the scope of this work.

The observed characteristics of the relative intensity ratio of ω_{2D1} and ω_{2D2} as a function of number of layers is also not in agreement with the calculated electron-phonon matrix elements from Fig.A.6(b). The latter suggest a stronger interaction for transitions responsible for the lower frequency ω_{2D1} subpeak, which shows a decreasing contribution to the 2D-peak intensity in the experiments. The deviation from the model could be explained when considering the number of sub-bands in the conduction and valence band as the number of layers is increased. A tight binding calculation of the band structure at the K-point for a structure consisting of 25-layers graphene show that there is an accumulation of bands at the position of the lowest conduction and highest valence band, respectively. These bands are identical in position with the bands from a tight binding calculation of three dimensional graphite. Although the interaction strength of the CB_1-CB_1 transition is small when compared to $CB_{N_i}-CB_{N_i}$, the increased number of possible transition might explain the larger intensity of the ω_{2D2} subpeak. Nevertheless, we propose the measured intensity ratio $I_{\omega_{2D1}}/I_{\omega_{2D2}}$ from the Raman scattering analysis as a method to estimate the number of graphene layers between 4 and 10 layers.

Bibliography

- [1] P.R. Wallace. The band theory of graphite. *Phys. Rev.*, 71(7):476, 1947.
- [2] JC Slonczewski and PR Weiss. Band structure of graphite. *Phys. Rev.*, 109(2):272–279, 1958.
- [3] J.W. McClure. Band structure of graphite and dehaas-vanalphen effect. *Phys. Rev.*, 108(3):612–618, 1957.
- [4] H. W. Kroto, J. R. Heath, S. C. O'Brien, R. F. Curl, and R. E. Smalley. C-60 - buckminsterfullerene. *Nature*, 318(6042):162–163, 1985.
- [5] S. Iijima. Helical microtubules of graphitic carbon. *Nature*, 354(6348):56–58, November 1991.
- [6] L.D. Landau. Zur theorie der phasenumwandlungen ii. *Phys. Z. Sowjetunion*, 11:26–35, 1937.
- [7] R.E. Peierls. Quelques proprietes typiques des corpses solides. *Ann. I. H. Poincare*, 5:177–222, 1935.
- [8] N.D Mermin and H. Wagner. Absence of ferromagnetism or antiferromagnetism in one- or 2-dimensional isotropic heisenberg models. *Physical Review Letters*, 17(22):1133–&, 1966.
- [9] N. Mermin. Crystalline order in 2 dimensions. *Phys. Rev.*, 176(1):250, 1968.
- [10] Landau, L.D., Lifshitz, E.M. *Statistical Physics, Part I*. Pergamon, Oxford, 1980.
- [11] K. S. Novoselov, A. K. Geim, S. V. Morozov, D. Jiang, Y. Zhang, S. V. Dubonos, I. V. Grigorieva, and A. A. Firsov. Electric field effect in atomically thin carbon films. *Science*, 306(5696):666–669, October 2004.
- [12] A. Fasolino, J. H. Los, and M. I. Katsnelson. Intrinsic ripples in graphene. *Nature Mat.*, 6(11):858–861, NOV 2007.
- [13] Nelson, D. R., and Piran, T., and Weinberg, S. *Statistical Mechanics of Membranes and Surfaces*. World Scientific, Singapore, 2004.
- [14] B. Partoens and F. M. Peeters. From graphene to graphite: Electronic structure around the k point. *Phys. Rev. B*, 74(7), AUG 2006.

- [15] K.S. Geim, A. Novoselov. The rise of graphene. *Nature Materials*, 6:183–191, 2004.
- [16] A. B. Kuzmenko, E. van Heumen, F. Carbone, and D. van der Marel. Universal optical conductance of graphite. *Phys. Rev. Lett.*, 100(11), MAR 21 2008.
- [17] R. R. Nair, P. Blake, A. N. Grigorenko, K. S. Novoselov, T. J. Booth, T. Stauber, N. M. R. Peres, and A. K. Geim. Fine structure constant defines visual transparency of graphene. *Science*, 320:5881, 2008.
- [18] J. C. Tsang, M. Freitag, V. Perebeinos, J. Liu, and Ph. Avouris. Doping and phonon renormalization in carbon nanotubes. *Nature Nanotechnology*, 2(11):725–730, NOV 2007.
- [19] A. Gambetta, C. Manzoni, E. Menna, M. Meneghetti, G. Cerullo, G. Lanzani, S. Tretiak, A. Piryatinski, A. Saxena, R. L. Martin, and A. R. Bishop. Real-time observation of nonlinear coherent phonon dynamics in single-walled carbon nanotubes. *Nature Physics*, 2(8):515–520, AUG 2006.
- [20] T. Mueller, F. Xia, and P. Avouris. Graphene photodetectors for high-speed optical communications. *Nature Photonics*, 4(5):297–301, MAY 2010.
- [21] Y. M. Lin, C. Dimitrakopoulos, K. A. Jenkins, D. B. Farmer, H. Y. Chiu, A. Grill, and P. Avouris. 100-ghz transistors from wafer-scale epitaxial graphene. *Science*, 327(5966):662–662, February 2010.
- [22] Jagdeep Shah. *Ultrafast spectroscopy of semiconductors and semiconductor nanostructures*. Springer-Verlag, 1999.
- [23] Y. B. Zhang, T. T. Tang, C. Girit, Z. Hao, M. C. Martin, A. Zettl, M. F. Crommie, Y. R. Shen, and F. Wang. Direct observation of a widely tunable bandgap in bilayer graphene. *Nature*, 459(7248):820–823, June 2009.
- [24] W. Bao, L. Jing, J. Velasco, Y. Lee, G. Liu, D. Tran, B. Standley, M. Aykol, S. B. Cronin, D. Smirnov, M. Koshino, E. McCann, M. Bockrath, and C. N. Lau. Stacking-dependent band gap and quantum transport in trilayer graphene. *Nature Physics*, 7(12):948–952, December 2011.
- [25] C. H. Lui, Z. Q. Li, K. F. Mak, E. Cappelluti, and T. F. Heinz. Observation of an electrically tunable band gap in trilayer graphene. *Nature Physics*, 7(12):944–947, December 2011.
- [26] F. Bonaccorso, Z. Sun, T. Hasan, and A. C. Ferrari. Graphene photonics and optoelectronics. *Nature Photonics*, 4(9):611–622, September 2010.

-
- [27] M.S. Dresselhaus R. Saito, G. Dresselhaus. *Physics Properties of Carbon Nanotubes*. Imperial College Press, 2005.
- [28] S.B. Trickey, F. Mullerplathe, G.H.F. Diercksen, and J.C. Boettger. Interplanar binding and lattice-relaxation in a graphite dilayer. *Phys. Rev. B*, 45(8):4460–4468, FEB 15 1992.
- [29] Alexander Grüneis. *Resonance Raman spectroscopy of single wall carbon nanotubes*. PhD thesis, Tohoku University, Japan, 2004.
- [30] EG Mishchenko and BI Halperin. Transport equations for a two-dimensional electron gas with spin-orbit interaction. *Phys. Rev. B*, 68(4), JUL 15 2003.
- [31] E. G. Mishchenko. Effect of electron-electron interactions on the conductivity of clean graphene. *Phys. Rev. B*, 98(21), MAY 25 2007.
- [32] K. F. Mak, M. Y. Sfeir, Y. Wu, C. H. Lui, J. A. Misewich, and T. F. Heinz. Measurement of the optical conductivity of graphene. *Phys. Rev. Lett.*, 101:196405, 2008.
- [33] L. A. Falkovsky and S. S. Pershoguba. Optical far-infrared properties of a graphene monolayer and multilayer. *Phys. Rev. B*, 76(15), OCT 2007.
- [34] T. Stauber, N. M. R. Peres, and A. K. Geim. Optical conductivity of graphene in the visible region of the spectrum. *Phys. Rev. B*, 78(8), AUG 2008.
- [35] Tsuneya Ando. Anomaly of optical phonon in monolayer graphene. *Journal of the physical society of Japan*, 75(12), DEC 2006.
- [36] Kentaro Nomura and A. H. MacDonald. Quantum transport of massless dirac fermions. *Phys. Rev. Lett.*, 98(7), FEB 16 2007.
- [37] NMR Peres, F Guinea, and AHC Neto. Electronic properties of disordered two-dimensional carbon. *Phys. Rev. B*, 73(12):125411, MAR 2006.
- [38] Kin Fai Mak, Matthew Y. Sfeir, Yang Wu, Chun Hung Lui, James A. Misewich, and Tony F. Heinz. Measurement of the optical conductivity of graphene. *Phys. Rev. Lett.*, 101(19), NOV 7 2008.
- [39] V. P. Gusynin, S. G. Sharapov, and J. P. Carbotte. Unusual microwave response of dirac quasiparticles in graphene. *Phys. Rev. Lett.*, 96(25):256802, JUN 30 2006.
- [40] Haug H. Koch S.W. *Quantum theory of the optical and electric properties of Semiconductors, Third edition*. World Scientific, 1994.
- [41] Lu C.L., Chang C.P., Huang Y.C., Chen R.B., Lin M.L. Influence of an electric field on the optical properties of few-layer graphene with ab-stacking. *Phys. Rev. B*, 73:144427, 2006.

- [42] Dresselhaus G. Johnson J.G. Optical properties of graphite. *Phys. Rev. B*, 7:2275, 1973.
- [43] Shyu F.L., Chang C.P., Chen R.B., Chiu C.W., Lin M.F. Magnetoelectronic and optical properties of carbon nanotubes. *Phys. Rev. B*, 67:045405, 2003.
- [44] Shung K.W.K. Lin M.F. Plasmons and optical properties of carbon nanotubes. *Phys. Rev. B*, 50:17744, 1994.
- [45] Georgii G. Samsonidze. *Photophysics of Carbon Nanotubes*. PhD thesis, Massachusetts Institute of Technology, 2007.
- [46] R. Nicklow, H. G. Smith, and N. Wakabayashi. Lattice-dynamics of pyrolytic-graphite. *Physical Review B*, 5(12):4951–4954, 1972.
- [47] T. Aizawa, R. Souda, S. Otani, Y. Ishizawa, and C. Oshima. Bond softening in monolayer graphite formed on transition-metal carbide surfaces. *Physical Review B*, 42(18):11469–11478, December 1990.
- [48] C. Oshima, T. Aizawa, R. Souda, Y. Ishizawa, and Y. Sumiyoshi. Surface phonon-dispersion curves of graphite(0001) over the entire energy region. *Solid State Communications*, 65(12):1601–1604, March 1988.
- [49] J Maultzsch, S Reich, and C Thomsen. Double-resonant Raman scattering in graphite: Interference effects, selection rules, and phonon dispersion. *Phys. Rev. B*, 70(15):155403, OCT 2004.
- [50] R. A. Jishi, L. Venkataraman, M. S. Dresselhaus, and G. Dresselhaus. Phonon modes in carbon nanotubes. *Chemical Physics Letters*, 209(1-2):77–82, June 1993.
- [51] Saito R. Jorio A., Dresselhaus M. and Dresselhaus G.F. *Raman Spectroscopy in Graphene Related Systems*. WILEY-VCH, 2011.
- [52] Leandro Malard Moreira. *Raman spectroscopy of graphene: probing phonons, electrons and electron-phonon interactions*. PhD thesis, Universidade federal de Minas Gerais, 2009.
- [53] C. Thomsen and S. Reich. Double resonant raman scattering in graphite. *Physical Review Letters*, 85(24):5214–5217, December 2000.
- [54] KS Novoselov, D Jiang, F Schedin, TJ Booth, VV Khotkevich, SV Morozov, and AK Geim. Two-dimensional atomic crystals. *Proceedings of the national academy of sciences of the united states of america*, 102(30):10451–10453, JUL 26 2005.
- [55] Nelson, D. R., Piran, T. & Weinberg, S. *Statistical Mechanics of Membranes and Surfaces*. World Scientific, Singapore, 2004.

-
- [56] D.R Nelson and L. Peliti. Fluctuations in membranes with crystalline and hexatic order. *Journal de physique*, 48(7):1085–1092, JUL 1987.
- [57] P LeDoussal and L Radzihovsky. Self-consistent theory of polymerized membranes. *Phys. Rev. Lett.*, 69(8):1209–1212, AUG 24 1992.
- [58] P. Blake, E. W. Hill, A. H. Castro Neto, K. S. Novoselov, D. Jiang, R. Yang, T. J. Booth, and A. K. Geim. Making graphene visible. *Applied Physics Letters*, 91(6), AUG 6 2007.
- [59] Alfonso Reina, Hyungbin Son, Liying Jiao, Ben Fan, Mildred S. Dresselhaus, ZhongFan Liu, and Jing Kong. Transferring and Identification of Single- and Few-Layer Graphene on Arbitrary Substrates. *Nano Letters*, 112(46):17741–17744, NOV 20 2008.
- [60] A. Das, S. Pisana, B. Chakraborty, S. Piscanec, S. K. Saha, U. V. Waghmare, K. S. Novoselov, H. R. Krishnamurthy, A. K. Geim, A. C. Ferrari, and A. K. Sood. Monitoring dopants by Raman scattering in an electrochemically top-gated graphene transistor. *Nature Nanotechnology*, 3(4):210–215, APR 2008.
- [61] Keun Soo Kim, Yue Zhao, Houk Jang, Sang Yoon Lee, Jong Min Kim, Kwang S. Kim, Jong-Hyun Ahn, Philip Kim, Jae-Young Choi, and Byung Hee Hong. Large-scale pattern growth of graphene films for stretchable transparent electrodes. *Nature*, 457(7230):706–710, FEB 5 2009.
- [62] X. Li, W. Cai, J. An, S. Kim, J. Nah, D. Yang, R. Piner, A. Velamakanni, I. Jung, E. Tutuc, S. K. Banerjee, L. Colombo, and R. S. Ruoff. Large-Area Synthesis of High-Quality and Uniform Graphene Films on Copper Foils. *Science*, 324(5932):1312–1314, JUN 5 2009.
- [63] Jian-Hao Chen, Chaun Jang, Shudong Xiao, Masa Ishigami, and Michael S. Fuhrer. Intrinsic and extrinsic performance limits of graphene devices on sio₂. *Nature Nanotechnology*, 3(4):206–209, April 2008.
- [64] A. C. Ferrari, J. C. Meyer, V. Scardaci, C. Casiraghi, M. Lazzeri, F. Mauri, S. Piscanec, D. Jiang, K. S. Novoselov, S. Roth, and A. K. Geim. Raman spectrum of graphene and graphene layers. *Phys. Rev. Lett.*, 97(18), NOV 3 2006.
- [65] Ying-Zhong Ma, Tobias Hertel, Zeev Vally Vardeny, Graham R. Fleming, and Leonas Valkunas. Ultrafast Spectroscopy of carbon nanotubes. *Nature Nanotechnology*, 111:321–352, 2008.
- [66] Korth kristalle gmbh, www.korth.de.
- [67] Bonini N., Lazzeri M., Marzari N., Mauri F. Phonon anharmonicities in graphite and graphene. *Phys. Rev. Lett.*, 99:176802, 2007.

- [68] D. Sun, Z. K. Wu, C. Divin, X. B. Li, C. Berger, W. A. de Heer, P. N. First, and T. B. Norris. *Physical Review Letters*, 104:136802, 2010.
- [69] Das Sarma S. Tse W.K. *Phys. Rev. B*, 79:235406, 2009.
- [70] MacDonald A.H. Bistrizter R. *Phys. Rev. Lett.*, 102:206410, 2009.
- [71] D. Sun, Z. K. Wu, C. Divin, X. B. Li, C. Berger, W. A. de Heer, P. N. First, and T. B. Norris. Ultrafast relaxation of excited dirac fermions in epitaxial graphene using optical differential transmission spectroscopy. *Physical Review Letters*, 101(15):157402, October 2008.
- [72] M. Breusing, C. Ropers, and T. Elsaesser. Ultrafast carrier dynamics in graphite. *Physical Review Letters*, 102(8):086809, February 2009.
- [73] Z. Q. Li, E. A. Henriksen, Z. Jiang, Z. Hao, M. C. Martin, P. Kim, H. L. Stormer, and D. N. Basov. Band structure asymmetry of bilayer graphene revealed by infrared spectroscopy. *Phys. Rev. Lett.*, 102(3), JAN 23 2009.
- [74] Wang H.N. et al. and Park J. Ultrafast relaxation dynamics of hot optical phonons in graphene. *Applied Physics Letters*, 96:081917, 2010.
- [75] F. Rana, P. A. George, J. H. Strait, J. Dawlaty, S. Shivaraman, M. Chandrashekar, and M. G. Spencer. Carrier recombination and generation rates for intravalley and intervalley phonon scattering in graphene. *Physical Review B*, 79(11):115447, March 2009.
- [76] S. Piscanec, M. Lazzeri, J. Robertson, A. C. Ferrari, and F. Mauri. Optical phonons in carbon nanotubes: Kohn anomalies, peierls distortions, and dynamic effects. *Physical Review B*, 75(3):035427, January 2007.
- [77] Lui, C. H., Mak K.F., Shan J., Heinz T.F. Ultrafast photoluminescence from graphene. *Phys. Rev. Lett.*, 105:127404, 2010.
- [78] Jalabert R. Das Sarma S., Jain J.K. *Phys. Rev. B*, 37:6290, 1988.
- [79] S. Butscher, F. Milde, M. Hirtshulz, E. Malic, and A. Knorr. Hot electron relaxation and phonon dynamics in graphene. *Applied Physics Letters*, 91(20):203103, November 2007.
- [80] X. Du, I. Skachko, A. Barker, and E. Y. Andrei. Approaching ballistic transport in suspended graphene. *Nature Nanotechnology*, 3(8):491–495, August 2008.
- [81] K. S. Novoselov, Z. Jiang, Y. Zhang, S. V. Morozov, H. L. Stormer, U. Zeitler, J. C. Maan, G. S. Boebinger, P. Kim, and A. K. Geim. Room-temperature quantum hall effect in graphene. *Science*, 315(5817):1379–1379, March 2007.

-
- [82] A. Urich, K. Unterrainer, and T. Mueller. Intrinsic response time of graphene photodetectors. *Nano Letters*, 11(7):2804–2808, July 2011.
- [83] F. W. Smith, Q. Le, V. Diadiuk, M. A. Hollis, A. R. Calawa, S. Gupta, M. Frenkel, D. R. Dykaar, G. A. Mourou, and T. Y. Hsiang. Picosecond gas-based photoconductive optoelectronic detectors. *Applied Physics Letters*, 54(10):890–892, March 1989.
- [84] S. Y. Chou, Y. Liu, J., and P. B. Fischer. Fabrication of sub-50 nm finger spacing and width high-speed metal-semiconductor-metal photodetectors using high-resolution electron-beam lithography and molecular-beam epitaxy. *Journal of Vacuum Science & Technology B*, 9(6):2920–2924, November 1991.
- [85] P. A. George, J. Strait, J. Dawlaty, S. Shivaraman, M. Chandrashekar, F. Rana, and M. G. Spencer. Ultrafast optical-pump terahertz-probe spectroscopy of the carrier relaxation and recombination dynamics in epitaxial graphene. *Nano Letters*, 8(12):4248–4251, December 2008.
- [86] D. Sun, G. Aivazian, A. M. Jones, J. S. Ross, W. Yao, D. Cobden, and X. D. Xu. Ultrafast hot-carrier-dominated photocurrent in graphene. *Nature Nanotechnology*, 7(2):114–118, February 2012.
- [87] F. N. Xia, T. Mueller, Y. M. Lin, A. Valdes-Garcia, and P. Avouris. Ultrafast graphene photodetector. *Nature Nanotechnology*, 4(12):839–843, December 2009.
- [88] Y. Y. Wang, Z. H. Ni, T. Yu, Z. X. Shen, H. M. Wang, Y. H. Wu, W. Chen, and A. T. S. Wee. Raman studies of monolayer graphene: The substrate effect. *Journal of Physical Chemistry C*, 112(29):10637–10640, July 2008.
- [89] T. Limmer, A. J. Houtepen, A. Niggebaum, R. Tautz, and E. Da Como. Influence of carrier density on the electronic cooling channels of bilayer graphene. *Applied Physics Letters*, 99(10):103104, September 2011.
- [90] Farhan Rana. Electron-hole generation and recombination rates for coulomb scattering in graphene. *Physical Review B*, 76(15):155431, October 2007.
- [91] Farhan Rana, Jared H. Strait, Haining Wang, and Christina Manolatos. Ultrafast carrier recombination and generation rates for plasmon emission and absorption in graphene. *Physical Review B*, 84(4):045437, July 2011.
- [92] F. Carbone, P. Baum, P. Rudolf, and A. H. Zewail. Structural preablation dynamics of graphite observed by ultrafast electron crystallography. *Physical Review Letters*, 100(3):035501, January 2008.

- [93] B. Barwick, H. S. Park, O. H. Kwon, J. S. Baskin, and A. H. Zewail. 4d imaging of transient structures and morphologies in ultrafast electron microscopy. *Science*, 322(5905):1227–1231, November 2008.
- [94] F. Carbone, O. H. Kwon, and A. H. Zewail. Dynamics of chemical bonding mapped by energy-resolved 4d electron microscopy rid a-2969-2012. *Science*, 325(5937):181–184, July 2009.
- [95] O. H. Kwon, B. Barwick, H. S. Park, J. S. Baskin, and A. H. Zewail. Nanoscale mechanical drumming visualized by 4d electron microscopy. *Nano Letters*, 8(11):3557–3562, November 2008.
- [96] R. Nuske, A. Jurgilaitis, H. Enquist, M. Harb, Y. Fang, U. Hakanson, and J. Larsson. Transforming graphite to nanoscale diamonds by a femtosecond laser pulse. *Applied Physics Letters*, 100(4):043102, January 2012.
- [97] C. Manzoni, A. Gambetta, E. Menna, M. Meneghetti, G. Lanzani, and G. Cerullo. Intersubband exciton relaxation dynamics in single-walled carbon nanotubes rid f-6669-2011 rid a-5747-2008 rid f-6534-2011. *Physical Review Letters*, 94(20):207401, May 2005.
- [98] T. Mishina, K. Nitta, and Y. Masumoto. Coherent lattice vibration of interlayer shearing mode of graphite. *Physical Review B*, 62(4):2908–2911, July 2000.
- [99] K. Ishioka, M. Hase, M. Kitajima, L. Wirtz, A. Rubio, and H. Petek. Ultrafast electron-phonon decoupling in graphite. *Physical Review B*, 77(12):121402, March 2008.
- [100] T. Kampfrath, L. Perfetti, F. Schapper, C. Frischkorn, and M. Wolf. Strongly coupled optical phonons in the ultrafast dynamics of the electronic energy and current relaxation in graphite. *Phys. Rev. Lett.*, 95(18):187403, October 2005.
- [101] K. Seibert, G. C. Cho, W. Kutt, H. Kurz, D. H. Reitze, J. I. Dadap, H. Ahn, M. C. Downer, and A. M. Malvezzi. Femtosecond carrier dynamics in graphite. *Physical Review B*, 42(5):2842–2851, August 1990.
- [102] D. H. Reitze, X. Wang, H. Ahn, and M. C. Downer. Femtosecond laser melting of graphite. *Physical Review B*, 40(17):11986–11989, December 1989.
- [103] H. O. Jeschke, M. E. Garcia, and K. H. Bennemann. Theory for the ultrafast ablation of graphite films rid c-3507-2009 rid d-2697-2009. *Physical Review Letters*, 87(1):015003, July 2001.
- [104] H. O. Jeschke, M. E. Garcia, and K. H. Bennemann. Time-dependent energy absorption changes during ultrafast lattice deformation rid c-3507-2009 rid d-2697-2009. *Journal of Applied Physics*, 91(1):18–23, January 2002.

-
- [105] Yagi T. Utsumi W. Light-transparent phase formed by room-temperature compression of graphite. *Science*, 252:1542–1544, 1991.
- [106] F. Carbone. The interplay between structure and orbitals in the chemical bonding of graphite. *Chemical Physics Letters*, 496(4-6):291–295, August 2010.
- [107] Z. B. Liu, X. Zhao, X. L. Zhang, X. Q. Yan, Y. P. Wu, Y. S. Chen, and J. G. Tian. Ultrafast dynamics and nonlinear optical responses from sp(2)- and sp(3)-hybridized domains in graphene oxide. *Journal of Physical Chemistry Letters*, 2(16):1972–1977, August 2011.
- [108] M. D. Shirk and P. A. Molian. Ultra-short pulsed laser ablation of highly oriented pyrolytic graphite. *Carbon*, 39(8):1183–1193, 2001.
- [109] T. Pfeifer, W. Kutt, H. Kurz, and R. Scholz. Generation and detection of coherent optical phonons in germanium. *Physical Review Letters*, 69(22):3248–3251, November 1992.
- [110] P. H. Tan and A. C. Ferrari. The shear mode of multilayer graphene. *Nature Materials*, 2012.
- [111] R. K. Raman, Y. Murooka, C. Y. Ruan, T. Yang, S. Berber, and D. Tomanek. Direct observation of optically induced transient structures in graphite using ultrafast electron crystallography. *Physical Review Letters*, 101(7):077401, August 2008.
- [112] R. Saito, A. Jorio, A. G. Souza, G. Dresselhaus, M. S. Dresselhaus, and M. A. Pimenta. Probing phonon dispersion relations of graphite by double resonance raman scattering. *Physical Review Letters*, 88(2):027401, January 2002.
- [113] A. G. Marinopoulos, L. Reining, A. Rubio, and V. Olevano. Ab initio study of the optical absorption and wave-vector-dependent dielectric response of graphite. *Physical Review B*, 69(24):245419, June 2004.
- [114] M. Lenner, A. Kaplan, C. Huchon, and R. E. Palmer. Ultrafast laser ablation of graphite. *Physical Review B*, 79(18):184105, May 2009.
- [115] L. M. Malard, M. H. D. Guimaraes, D. L. Mafra, M. S. C. Mazzoni, and A. Jorio. Group-theory analysis of electrons and phonons in n-layer graphene systems. *Physical Review B*, 79(12):125426, March 2009.
- [116] A. Gupta, G. Chen, P. Joshi, S. Tadigadapa, and P. C. Eklund. Raman scattering from high-frequency phonons in supported n-graphene layer films. *Nano Letters*, 6(12):2667–2673, December 2006.

- [117] L. G. Cancado, M. A. Pimenta, R. Saito, A. Jorio, L. O. Ladeira, A. Grueneis, A. G. Souza, G. Dresselhaus, and M. S. Dresselhaus. Stokes and anti-stokes double resonance raman scattering in two-dimensional graphite. *Physical Review B*, 66(3):035415, July 2002.
- [118] H. Wang, Y. F. Wang, X. W. Cao, M. Feng, and G. X. Lan. Vibrational properties of graphene and graphene layers. *Journal of Raman Spectroscopy*, 40(12):1791–1796, December 2009.
- [119] L. M. Malard, J. Nilsson, D. C. Elias, J. C. Brant, F. Plentz, E. S. Alves, A. H. Castro, and M. A. Pimenta. Probing the electronic structure of bilayer graphene by raman scattering. *Physical Review B*, 76(20):201401, November 2007.

Acknowledgments